

Immobilization of Mercury by Stabilized FeS Nanoparticles and Effects of Oil Dispersant on Sorption/Desorption and Photodegradation of Polycyclic Aromatic Hydrocarbons

by

Yanyan Gong

A dissertation submitted to the Graduate Faculty of
Auburn University
in partial fulfillment of the
requirements for the Degree of
Doctor of Philosophy

Auburn, Alabama
May 4, 2014

Keywords: Mercury Immobilization, Iron Sulfide Nanoparticles, Oil dispersants, Sediment Sorption, Polycyclic Aromatic Hydrocarbon, Photodegradation

Copyright 2014 by Yanyan Gong

Approved by

Dongye Zhao, Chair, Elton Z. and Lois G. Endowed Professor of Environmental Engineering
Orlando Acevedo, Associate Professor of Chemistry & BioChemistry
Mark Barnett, Malcolm Pirnie Professor of Environmental Engineering
Prabhakar Clement, Harold Vince Groome Jr. Endowed Professor of Environmental Engineering
Christopher Roberts, Uthlaut Professor of Chemical Engineering

Abstract

Iron sulfide (FeS) nanoparticles were prepared with sodium carboxymethyl cellulose (CMC) as a stabilizer, and tested for enhanced removal of mercury (Hg^{2+}) from water, soil and sediment. The presence of CMC at ≥ 0.03 wt.% can fully stabilize 0.5 g/L of FeS (i.e. CMC-to-FeS molar ratio ≥ 0.0006) through concurrent electrostatic and steric stabilization mechanisms. Fourier transform infrared spectroscopy (FTIR) spectra suggested that CMC molecules were attached to the nanoparticles through bidentate bridging and hydrogen bonding. Increasing the CMC-to-FeS molar ratio from 0 to 0.0006 enhanced mercury sorption capacity by 20%; yet, increasing the ratio from 0.0010 to 0.0025 diminished the sorption by 14%. FTIR and X-ray diffractograms (XRD) analyses suggested that precipitation (formation of cinnabar and metacinnabar), ion exchange (formation of $\text{Hg}_{0.89}\text{Fe}_{0.11}\text{S}$) and surface complexation were important mechanisms for mercury removal. Batch kinetic data revealed that the stabilized nanoparticles facilitated rapid uptake of Hg^{2+} , and the kinetic data can be interpreted with a pseudo-second-order kinetic model. We proposed a dual-mode isotherm model, which considers both precipitation and adsorption mechanisms, to interpret the sorption isotherm data. High mercury uptake was observed over the pH range of 6.5-10.5, whereas at $\text{pH} < 6$ significant loss in Hg capacity was observed. High concentrations of Cl^- (> 106 mg/L) and dissolved organic matter (5 mg/L as TOC) may inhibit Hg uptake, while effect of ionic strength (0-0.2 M) was negligible. When aged for 2.5 years, 14% of sorbed Hg^{2+} was leached out of the nanoparticles due to pH drop. The leaching, however, can be prevented by maintaining pH above neutral.

In situ immobilization of Hg in field-contaminated soil and sediment using soil-deliverable CMC-FeS nanoparticles (CMC-to-FeS molar ratio = 0.0010) was investigated through a series of batch and column experiments. Transmission electron microscopy measurements revealed a particle size of 34.3 ± 8.3 nm (standard deviation), whereas dynamic light scattering gave a hydrodynamic diameter of 222.5 ± 3.2 nm. Batch tests showed that at an FeS-to-Hg molar ratio of 28:1 to 118:1, the nanoparticles reduced water-leachable Hg by 79%-96% and the TCLP (Toxicity Characteristic Leaching Procedure) based leachability by 26%-96%. Column breakthrough tests indicated that the nanoparticles were deliverable in the sediment/soil columns under moderate injection pressure. However, once the external pressure was removed, the delivered nanoparticles remained virtually immobile under typical groundwater flow conditions. When the Hg contaminated soil and sediment were treated with 52 to 95 pore volumes of a 500 mg/L FeS nanoparticle suspension, water-leachable Hg was reduced by 90%-93% and TCLP-leachable Hg was reduced by 65%-91%. The results warrant further field demonstration of this promising *in situ* remediation technology.

During the 2010 Deepwater Horizon oil spill, ~2.1 million gallons of dispersants were applied to the surface and well head to break up oil slicks. However, it remains unknown how the dispersants affect the environmental fate and transport of persistent oil components such as polycyclic aromatic hydrocarbons (PAHs) in the Gulf Coast ecosystems. Effects of a model oil dispersant (Corexit EC9500A) on sorption/desorption of phenanthrene were investigated with two marine sediments. Kinetic data revealed that the presence of the dispersant at 18 mg/L enhanced phenanthrene uptake by up to 7%, whereas the same dispersant during desorption reduced phenanthrene desorption by up to 5%. Sorption isotherms confirmed that at dispersant concentrations of 18 and 180 mg/L phenanthrene uptake progressively increased for both

sediments. Furthermore, the presence of the dispersant during desorption induced remarkable sorption hysteresis. The effects were attributed to added phenanthrene affinity and capacity due to sorption of the dispersant on the sediments. Dual-mode models adequately simulated sorption isotherms and kinetic data in the presence of the dispersant. Water accommodated oil (WAO) and dispersant-enhanced WAO increased phenanthrene sorption by up to 22%.

Effects of the oil dispersant Corexit EC9500A on UV-mediated photodegradation of pyrene in the Gulf Coast seawater were investigated. The presence of 18 and 180 mg/L of the dispersant increased the first-order photodegradation rate by 5.5% and 17%, respectively, within 360 min, and the dispersant also reduced or eliminated pyrene volatilization. By combining the individual first-order rate laws for volatilization and photodegradation, we proposed an integrated kinetic model that was able to adequately predict the overall degradation data. Mechanistic studies indicated that superoxide radicals play a predominant role, and 1-hydroxypyrene was the main intermediate in the degradation process with and without the dispersant, suggesting that electrons are transferred from excited pyrene to oxygen. The dispersant enhanced the formation of the superoxide radicals. In the presence of 18 mg/L of the dispersant, the first-order photodegradation rate increased with increasing ionic strength and temperature, decreased with increasing HA concentration, but remained independent of solution pH. The results are important for understanding the roles of oil dispersants on environmental fate of spilled oil and persistent oil components.

Acknowledgments

I would never have been able to finish my dissertation without the help and support of my committee members, friends, and family.

First and foremost, I would like to express my sincerest gratitude to my major advisor, Dr. Dongye Zhao, for his excellent guidance, inspiration, caring, patience, motivation, and encouragement through the research. He taught me not only to be an experimentalist, but also an independent and creative thinker. His truly scientist intuition has made him a constant oasis of ideas, which exceptionally inspires and enriches my growth as a student, as a researcher and as an engineer. I am indebted to him more than he knows. I thank him for everything he has done for me.

I gratefully acknowledge Drs. Christopher Roberts, Mark Barnett, Orlando Acevedo, Prabhakar Clement, and Ahjeong Son for their services on my Ph.D. committee, for their valuable advice, enlightening guidance, encouraging words, and thoughtful criticism. It has been my pleasure working with them. Sincere appreciation is also extended to Dr. Virginia Davis, who served in the committee as the outside reader. I would like to thank Dr. Yucheng Feng and Jinling Zhuang for their analytical and technical assistance. Special thanks are extended to my fellow students in the environmental engineering program here at AU for their friendship, helps, research advices and for creating a supportive environment.

Finally, I would like to thank my parents and friends for their support and encouragement throughout my study.

Table of Contents

Abstract.....	ii
Acknowledgments.....	v
List of Tables	ix
List of Figures.....	x
Chapter 1. General Introduction	1
1.1 Mercury contamination in environmental media	1
1.2 Chemical dispersion of oil spill and related knowledge gaps	3
1.3 Photochemical degradation of PAHs	5
1.4 Objectives.....	6
1.5 Organization	8
Chapter 2. Immobilization of Mercury by Carboxymethyl Cellulose Stabilized Iron Sulfide Nanoparticles: Reaction Mechanisms and Effects of Stabilizer and Water Chemistry	10
2.1 Introduction.....	10
2.2 Materials and Methods	14
2.2.1 Chemicals	14
2.2.2 Preparation of CMC-FeS nanoparticles.....	14
2.2.3 Characterization of CMC-FeS nanoparticles.....	15
2.2.4 Effects of CMC concentration on stability of FeS nanoparticles and mercury sorption	17
2.2.5 Mercury sorption kinetic tests	18
2.2.6 Mercury sorption isotherm tests	18
2.2.7 Effects of pH, Cl ⁻ , DOM/HA, and IS	19
2.2.8 Analytical methods.....	20
2.3 Results and discussion.....	21
2.3.1 Characterization of CMC-FeS Nanoparticles.....	21
2.3.2 Interactions between CMC and FeS and nature of Hg ²⁺ uptake by CMC-FeS	23
2.3.3 Effects of CMC concentration on nanoparticle stability and Hg sorption capacity	26
2.3.4 Mercury sorption kinetics, isotherm, and mechanisms	29
2.3.5 Effects of pH.....	35

2.3.6 Effect of chloride	37
2.3.7 Effect of DOM.....	38
2.3.8 Effects of ionic strength.....	40
2.4 Conclusions	42
Chapter 3. Immobilization of Mercury in Field Soil and Sediment Using Carboxymethyl Cellulose Stabilized Iron Sulfide Nanoparticles	45
3.1 Introduction	45
3.2 Materials and methods	48
3.2.1 Materials	48
3.2.2 Soil and sediment analysis.....	49
3.2.3 Preparation of CMC-FeS nanoparticles.....	52
3.2.4 Characterization of CMC-FeS nanoparticles.....	52
3.2.5 Immobilization of Hg: batch tests	53
3.2.6 TCLP tests	53
3.2.7 Deliverability of CMC-FeS nanoparticles.....	54
3.2.8 Immobilization of Hg: column tests.....	55
3.2.9 Chemical analysis.....	55
3.3 Results and discussion.....	56
3.3.1 Characterization of CMC-FeS Nanoparticles.....	56
3.3.2 Immobilization of mercury: batch tests.....	58
3.3.3 TCLP leachability of Hg	62
3.3.4 Deliverability and transport of CMC-stabilized FeS nanoparticles in sediment and soil	63
3.4 Conclusions	69
Chapter 4. Effects of Oil Dispersant and Oil on Sorption and Desorption of Phenanthrene with Gulf Coast Marine Sediments.....	71
4.1 Introduction	71
4.2 Materials and methods.....	73
4.2.1 Materials.....	73
4.2.2 Seawater and sediment analyses.....	75
4.2.3 Sorption and desorption of Corexit EC9500A by sediment.....	78
4.2.4 Effects of dispersant on sorption/desorption kinetics of phenanthrene.....	78
4.2.5 Effect of dispersant on sorption/desorption isotherms of phenanthrene	80
4.2.6 Dual-mode sorption equilibrium and kinetic models	80
4.2.7 Effects of dispersant dosage on phenanthrene uptake	81
4.2.8 Effects of WAO and DWAO on sorption kinetics of phenanthrene	81
4.2.9 Chemical analysis.....	82
4.3 Results and discussion.....	83

4.3.1 CMC value of Corexit EC9500A	83
4.3.2 Sorption and desorption of Corexit EC9500A	85
4.3.3 Effects of dispersant on sorption kinetics of phenanthrene	86
4.3.4 Effects of dispersant on desorption kinetics of phenanthrene	89
4.3.5 Effects of dispersant on sorption/desorption isotherms of phenanthrene	92
4.3.6 Effects of dispersant dosage on phenanthrene uptake	95
4.3.7 Effects of aging on sorption isotherms of phenanthrene	97
4.3.8 Effects of WAO and DWAO on sediment sorption of phenanthrene	98
4.4 Conclusions	103
Chapter 5. Effects of Oil Dispersant on Photodegradation of Pyrene in Gulf Coast Marine Water	105
5.1 Introduction	105
5.2 Materials and Methods	108
5.2.1 Materials	108
5.2.2 Experimental apparatus	109
5.2.3 Effects of dispersant on volatilization and photodegradation of pyrene	110
5.2.4 Effects of radical scavengers on UV-mediated photochemical degradation of pyrene	111
5.2.5 Photodegradation pathways of pyrene with and without dispersant	111
5.2.6 Effects of solution chemistry and temperature	111
5.2.7 Analytical methods	112
5.3 Results and Discussion	113
5.3.1 UV spectroscopic studies of pyrene in dispersant solutions	113
5.3.2 Effects of dispersant on photodegradation of pyrene in seawater under UV and sunlight irradiations	114
5.3.3 Effects of dispersant on volatilization and photodegradation of pyrene in seawater	117
5.3.4 Role of radicals on photodegradation of pyrene	119
5.3.5 Photodegradation pathway of pyrene and effects of dispersant	122
5.3.6 Dispersant effects on UV-facilitated pyrene photodegradation	124
5.3.7 Effects of solution chemistry on photochemical degradation of pyrene in dispersant solution	125
5.4 Conclusions	129
Chapter 6. Conclusions and Suggestions for Future Research	132
6.1 Summary and Conclusions	132
6.2 Suggestions for Future Work	136
References	139
Appendix	159

List of Tables

Table 2-1. Pseudo-first-order and pseudo-second-order models used for simulating mercury sorption kinetic data and the resulting fitting parameters.	30
Table 2-2. Best-fitted parameters for Langmuir, Freundlich and dual-mode sorption isotherm models.	33
Table 3-1. Salient physical and chemical properties of soil and sediment samples.....	51
Table 3-2. Equilibrium Hg distribution coefficient (K_d) for the sediment/soil in the absence and presence of CMC-FeS nanoparticles	62
Table 4-1. Salient physical and chemical properties of marine sediments used in this work.....	76
Table 4-2. Characteristics of surfactant compositions in the oil dispersant Corexit EC9500A....	77
Table 4-3. Equilibrium sorption parameters for phenanthrene onto loamy sand and sandy loam sediments in the absence or presence of various concentrations of the dispersant.....	89
Table 4-4. The best-fitted values of phenanthrene diffusivities and the corresponding mean weighted square error (MWSE) in the absence or presence of the dispersant.	89
Table 5-1. First-order photodegradation rate constants for pyrene photodegradation in the absence and presence of Corexit EC9500A under UV light and sunlight irradiations.....	117
Table 5-2. First-order rate constants for pyrene volatilization or/and UV-mediated photodegradation in the absence and presence of Corexit EC9500A	118
Table 5-3. Contributions of radicals ($\cdot\text{OH}$, $^1\text{O}_2$ and $\text{O}_2^{\cdot-}$) to pyrene photodegradation with and without 18 mg/L of Corexit EC9500A.....	121
Table 5-4. First-order rate constants for pyrene photodegradation in the presence of 18 mg/L of dispersant as a function of ionic strength (IS), humic acid (HA) concentration, pH, and temperature.	125
Table A-1. PAHs targeted and detected in the Gulf Coast seawater (seawater was filtered through 0.45 μm membrane without autoclaving), loamy sand, and sandy loam sediments (sediments were only wet-sieved).	161

List of Figures

Figure 1-1. Mechanism of chemical dispersion of oil..	4
Figure 2-1. Procedure for synthesizing CMC-stabilized FeS nanoparticles.....	15
Figure 2-2. XRD spectra for: (a) neat CMC powders, and (b) bare FeS and CMC-FeS nanoparticles.....	21
Figure 2-3. Digital photographs and TEM images of (a) bare FeS aggregates, (b) CMC-FeS nanoparticles (FeS = 0.5 g/L, CMC = 0.05%), and (c) particle size distribution of CMC-FeS nanoparticles based on a random sample of 941 particles from 3 TEM images.	23
Figure 2-4. FTIR spectra of neat CMC powder, bare FeS particles, CMC-FeS nanoparticles, and Hg ²⁺ -laden CMC-FeS.....	24
Figure 2-5. Aqueous suspensions of FeS particles prepared at 500 mg/L as FeS in the presence of various concentrations of CMC: 0, 0.005, 0.01, 0.03, 0.05, 0.08, 0.10, and 0.13 wt% (or CMC-to-FeS molar ratios: 0, 0.0001, 0.0002, 0.0006, 0.0010, 0.0016, 0.0020, and 0.0025). Pictures were taken 24 hours after synthesis.	26
Figure 2-6. Volume weighted hydrodynamic diameters of FeS particles prepared at 500 mg/L as FeS and at various CMC-to-FeS molar ratios, when aged for 1 day and 6 months.	27
Figure 2-7. Mercury uptake by FeS nanoparticles prepared at various CMC-to-FeS molar ratios.	29
Figure 2-8. (a) Mercury sorption kinetics by CMC-FeS, and (b) pseudo-first-order and (c) pseudo-second-order kinetic fittings of mercury sorption by CMC-FeS.....	30
Figure 2-9. Mercury sorption isotherm of CMC-FeS nanoparticles.....	32
Figure 2-10. XRD spectra of A: Hg ²⁺ -laden CMC-FeS nanoparticles, and B: Hg ²⁺ -laden bare FeS aggregates.....	35
Figure 2-11. Mercury uptake by CMC-FeS as a function of equilibrium pH.....	36
Figure 2-12. (a) Dissolution of CMC-FeS measured as soluble Fe as a function of final pH, and (b) Fe speciation (without CMC) simulated using Visual MINTEQ (version 2.61).....	36
Figure 2-13. (a) Effects of chloride on mercury removal by CMC-FeS. (b) Mercury speciation as a function of Cl ⁻ concentrations simulated using Visual MINTEQ (version 2.61).....	38
Figure 2-14. Effects of DOM and HA on mercury uptake by CMC-FeS.....	39

Figure 2-15. Effects of ionic strength on mercury uptake by CMC-FeS.....	41
Figure 2-16. Mercury uptake by CMC-FeS and evolution of suspension pH as a function of aging.....	42
Figure 3-1. UV-vis absorption spectra of: (a) 0.05% CMC, (b) 318 mg/L Fe ²⁺ , (c) Fe ²⁺ -CMC complexes (0.05% CMC, 318 mg/L Fe ²⁺), (d) 182 mg/L S ²⁻ , (e) 50 mg/L CMC-FeS nanoparticles, and (f) 50 mg/L bare FeS.....	57
Figure 3-2. Desorption of Hg from (a) Hg-spiked sediment AL1, (b) soil NJ4, and (c) soil NJ38 in the absence or presence of various concentrations of CMC-FeS nanoparticles.....	59
Figure 3-3. Hg concentrations in the TCLP #1 fluids for Hg-loaded sediment AL1 before and after FeS nanoparticles treatments (Reaction time: 18 hours).....	63
Figure 3-4. (a) Breakthrough curves of a tracer (KBr) and CMC-FeS nanoparticles through sediment AL1 (KBr = 50 mg/L, FeS = 500 mg/L, CMC = 0.05%, pore velocity = 0.22 cm/min, EBCT = 113 min), and (b) Measured FeS nanoparticles retention profiles in the Hg-loaded sediment AL1 column.....	64
Figure 3-5. Breakthrough curves of a tracer (KBr) and CMC-FeS nanoparticles through soil NJ4 (KBr = 50 mg/L, FeS = 500 mg/L, CMC = 0.05%, pore velocity = 0.10 cm/min, EBCT = 102 min).....	66
Figure 3-6. Total and dissolved Hg elution histories from Hg-loaded sediment AL1 when subjected to 500 mg/L CMC-FeS nanoparticles or a CMC solution (CMC = 0.05%, pore velocity = 0.22 cm/min, EBCT = 113 min). Inset: a close-up of dissolved Hg concentration histories.....	67
Figure 3-7. Total and dissolved Hg elution histories from soil NJ4 when subjected to 500 mg/L CMC-FeS nanoparticles or a CMC solution (CMC = 0.05%, pore velocity = 0.10 cm/min, EBCT = 102 minutes). Inset: a close-up of dissolved Hg concentration histories.....	69
Figure 4-1. Solution surface tension as a function of concentration of Corexit EC9500A for determination of the apparent CMC value of the dispersant.....	84
Figure 4-2. Sorption and the corresponding desorption isotherms of Corexit EC9500A on a sandy loam sediment.....	85
Figure 4-3. Sorption kinetics of phenanthrene onto (a) loamy sand and (b) sandy loam sediments in the absence or presence of 18 mg/L of Corexit EC9500A.....	87
Figure 4-4. Desorption kinetics of phenanthrene from loamy sand and sandy loam sediments under four scenarios.....	91
Figure 4-5. Effects of Corexit EC9500A on sorption isotherms of phenanthrene on (a) loamy sand and (b) sandy loam.....	92
Figure 4-6. Effects of Corexit EC9500A on desorption hysteresis of phenanthrene on sediments under four scenarios.....	94
Figure 4-7. Phenanthrene uptake (q_e) by (a) loamy sand and (b) sandy loam sediments in the presence of various concentrations (0-860 mg/L) of Corexit EC9500A.....	96

Figure 4-8. Effects of aging time on phenanthrene uptake (q_e) by (a) loamy sand and (b) sandy loam under various concentrations (0 and 180 mg/L) of Corexit EC9500A.....	97
Figure 4-9. Effects of WAO and DWAO on sorption kinetics of phenanthrene onto (a) loamy sand and (b) sandy loam.....	98
Figure 4-10. GC-MS analysis of WAO and DWAO as a function of the number of carbon atoms (a), and the type of chemical compounds (b).	100
Figure 4-11. Hydrocarbon compositions of WAO and DWAO before and after sorption by loamy sand and sandy loam as a function of the number of carbon atoms or the type of chemical compounds.....	102
Figure 5-1. A schematic of the experimental set-up under (a) UV light, and (b) simulated sunlight.	110
Figure 5-2. UV-Vis absorption spectra of pyrene in seawater and in a monomeric dispersant solution (18 mg/L) and micellar dispersant solution (180 mg/L)	114
Figure 5-3. First-order kinetic plots of (a) photochemical degradation, (b) volatilization, and (c) combined volatilization and photodegradation of pyrene in seawater and in a monomeric dispersant Corexit EC9500A solution (18 mg/L) and micellar dispersant solution (180 mg/L).....	116
Figure 5-4. Photochemical degradation mechanism of pyrene in the aqueous solution.....	123
Figure 5-5. Peak areas of intermediates 1-hydroxypyrene during the photodegradation of pyrene in the presence and absence of Corexit EC9500A	123
Figure 5-6. Effects of (a) IS, (b) HA, (c) pH, and (d) temperature on photodegradation of pyrene in 18 mg/L dispersant solution	127
Figure 5-7. Absorption spectra of 5.5 mg/L HA and 60 μ g/L pyrene in 18 mg/L dispersant solution	128
Figure A-1. (a) An overview of the sampling location of two marine sediments and seawater samples.; and (b) A close-up of the sampling sites.....	160
Figure A-2. Solubility of phenanthrene as a function of Corexit EC9500A dosage.	163

Chapter 1. General Introduction

1.1 Mercury contamination in environmental media

Mercury (Hg) has been known to be one of the most pervasive and bio-accumulative neurotoxins in the environment (Jeong et al., 2007; Xiong et al., 2009). It has three oxidation states (+I, +II and 0), and the ready interconversion of inorganic and organic forms. Among the most cited health effects of Hg are damage of the central nervous system and the gastrointestinal tract, mental and motor dysfunction, impairment of pulmonary and kidney function, and chest pain (Bayramoglu and Arica, 2007; Mercone et al., 1999; Sweet and Zelikoff, 2001). Hg methylation takes place in anaerobic soil/sediment mediated by sulfate reducing bacteria, and the methylated Hg can then accumulate at high levels in the aquatic food chain (Gilmour et al., 1992; Kerin et al., 2006; Stein et al., 1996). Consequently, controlling Hg methylation is considered a key step to mitigate human exposure to Hg.

To mitigate human exposure, the U.S. Environmental Protection Agency (EPA) has set a maximum contaminant level (MCL) of 2 $\mu\text{g/L}$ for mercury in drinking water.

In the subsurface, Hg can be a long-term contaminant source to groundwater and surface water (Bower et al., 2008). Various technologies have been studied to remove Hg from contaminated sites, including phytoremediation, bioremediation, excavation and thermal treatments, and constructed wetland (Atwood and Zaman, 2006). However, these processes bear with some critical constraints. For instance, excavation and *ex situ* treatment of contaminated soil/sediment is environmentally disruptive, and costly if the contamination is distributed over a

large area and/or extends deep in the ground (Bower et al., 2008). Furthermore, conventional technologies are not accessible to Hg plumes located deep in the groundwater aquifer or underneath existing infrastructures. Consequently, innovative *in situ* remediation technologies to immobilize Hg in contaminated soils or sediments are urgently needed.

Sulfide minerals have been known to be effective sorbents for Hg (Brown et al., 1979). In sulfidic sediments, the dominant mineral phases are generally pyrite (FeS_2), greigite (Fe_3S_4), amorphous FeS, and mackinawite (FeS) (Morse and Arakaki, 1993). Of all the sulfide minerals, iron sulfide (FeS) has drawn a lot of attention because it is first formed in most anoxic environments, and has been accepted to be a major constituent of acid-volatile sulfides (Berner, 1964; Rickard et al., 1995; Rickard, 1974). Because of the high sorption capacity for Hg^{2+} , its ubiquitous presence and long-term stability in anoxic sediments, FeS holds the potential for immobilizing Hg^{2+} in the subsurface environment (Jeong et al., 2007).

Numerous studies have shown that FeS can effectively immobilize Hg from aqueous solutions. For example, at an initial FeS solid concentration range of 0.28-0.40 g/L, 100% of 200 mg/L Hg was removed from the aqueous system within 24 hours (Liu et al., 2008). However, natural or conventionally synthesized FeS particles are typically in the millimeter or larger scale, which are too big to be delivered into Hg-contaminated soil or sediment. These macroscale particles are not deliverable into the contaminant source zones, and thus, not suitable for *in situ* immobilization of Hg in soil or sediment. Consequently, nanoscaled FeS particles must be developed to facilitate direct delivery of the nanoparticles into the target contaminated zone. The particle reactivity and transportability should also be investigated.

1.2 Chemical dispersion of oil spill and related knowledge gaps

The 2010 Deepwater Horizon (DWH) oil spill released an estimated 4.6 million barrels of South Louisiana sweet crude oil into the Gulf of Mexico, resulting in the largest marine oil spill in U.S. history and perhaps the second largest in the world, after the first Gulf War oil spill from Kuwait (Abbriano et al., 2011; Graham et al., 2010; Griffiths, 2012; Hemmer et al., 2011). In response to the incident, BP applied approximately 2.1 million gallons of oil dispersants (Corexit EC9500A and Corexit 9527), of which 1.4 million gallons were applied at the surface and 0.77 million gallons at the wellhead (Kujawinski et al., 2011). Oil dispersants lower the oil-water interfacial tension, thereby breaking oil slicks into fine droplets and accelerating dispersal into the water column and dissolution of the hydrophobic oil components (NRC, 2005).

Once oil is released into the marine environment, it undergoes complex physical, chemical and biological transformations, including spreading, drifting, dispersion, stranding, and weathering. The important weathering processes include evaporation, dissolution, biodegradation, emulsification (i.e., “mouse” formation), and photo-oxidation (NRC, 2003). Whole oil droplets may be dispersed into the water column while monocyclic compounds (e.g., benzene and alkyl-substituted benzenes) with $\log K_{ow}$ values between 2.1 and 3.7 and selected lower molecular weight, 2-3 ring polycyclic aromatic hydrocarbons (PAHs) with $\log K_{ow}$ values between 3.7 and 4.8 may undergo partial dissolution (NRC, 2005; Payne et al., 2003). These environmental processes can be strongly affected by interactions between dissolved and dispersed oil components and sediment particles.

Polycyclic aromatic hydrocarbons (PAHs) are considered one of the principal contaminant classes of environmental concern associated with the oil spill due to their toxicity, mutagenicity, carcinogenicity and persistency (Nam et al., 2008). Sorption and desorption play an important

role in governing the fate, transport, bioavailability, and toxicity of PAHs in environmental systems (Johnson et al., 2008).

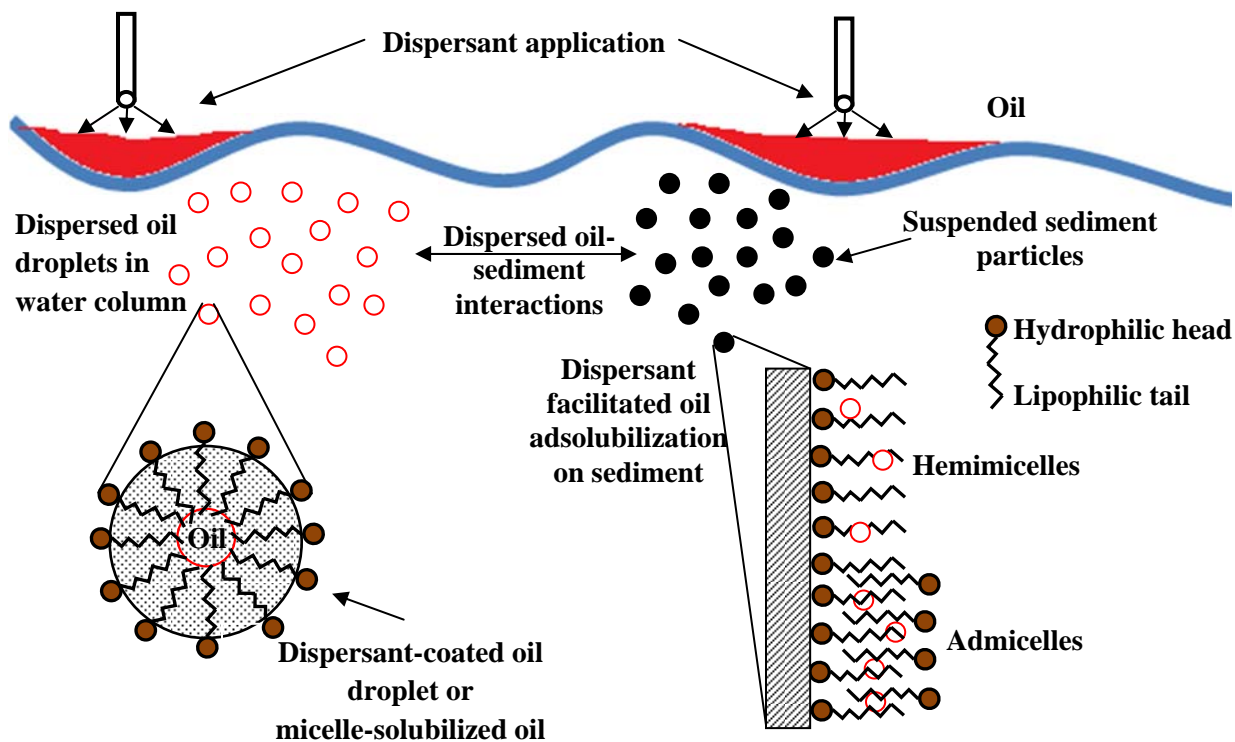


Figure 1-1. Mechanism of chemical dispersion of oil. Left: accumulation of dispersant molecules at oil-water interface facilitates formation of fine oil droplets that become entrained in the water column; Right: accumulation of dispersants at sediment-water interface facilitates sorption (adsolubilization) of oil in the solid phase. Alternatively, dispersed oil droplets may also form agglomerates with suspended particulate material (SPM), which can be stable colloids or re-suspended (temporarily stable) sediment particles.

Figure 1-1 depicts the mechanisms of chemical dispersion of surface oil in aquatic systems containing suspended sediment particles. On one hand, dispersant/surfactant-facilitated dissolution or solubilization of oil is achieved through formation of surfactant-coated oil droplets

or partitioning of oil into the surfactant micelles. On the other hand, dispersant/surfactant can be sorbed onto the sediment surface forming so-called “hemimicelles” and “admicelles” (Behrends, 1999; NRC, 2005), which can in turn enhance uptake of hydrophobic compounds through adsolubilization.

However, there is limited knowledge regarding how oil dispersants affect the fate and transport of PAHs in the marine environment, and specifically in the Gulf of Mexico ecosystem. Therefore, knowledge of sorption and desorption of PAHs in the presence of dispersant is important for understanding the fate and transport mechanisms of PAHs, and predicting its long-term effects following an oil spill.

1.3 Photochemical degradation of PAHs

The fate of petroleum components in the marine environment is controlled by a combination of abiotic and biotic processes. Among the abiotic processes, photochemical degradation is an important pathway for the transformation of crude oil in tropical seawater, especially with the oil rich in aromatics (D'Auria et al., 2008).

Different irradiation sources including mercury lamps, natural sunlight and xenon lamps have been used. The UV light-induced photodegradation is achieved by the cleavage of conjugated chains, which can shift the wavelength of absorbed light from the visible range to ultraviolet range (Chu and Ma, 1998). It has been reported that the superoxide radical anion ($O_2^{\bullet -}$) can be generated when UV is absorbed by dissolved oxygen (DO) (Pajares et al., 1999). D'Auria et al. (2008) conducted a series of photodegradation experiments on an Italian crude oil. The results showed that upon UV irradiation, the predominant fraction of oil components shifted from C7-C12 to C13-C25. Solar irradiation gave similar results: While the relative amounts of branched and cyclic alkanes sharply decreased, the fraction of the linear alkanes and aromatic compounds

increased. The results indicate that small branched and cyclic oil components can be photodegraded rather rapidly, whereas larger paraffins ($C > 13$) and PAHs are more resistant to the photodegradation process.

The water matrix (either photoactive compounds in water or the interactions between photogenerated reactive species and water components) may affect the photochemical processes (Chiron et al., 2006). For instance, dissolved organic matter (DOM) is ubiquitous in natural waters may affect the photodegradation process. Humic acid (HA), the hydrophobic fraction of DOM, can both increase the degradation by acting as photosensitizers and inhibit it by competitive absorption of solar radiation, and the overall effect depends on the balance between the opposing contributions (Andreozzi et al., 2003).

It is evident that PAHs have been found to undergo photochemical degradation or transformation, and the reaction rates can be affected by the environmental conditions. Based on our knowledge, there have been no studies aiming at investigating effects of oil dispersants applied during the DWH oil spill onto PAHs photodegradation. Information is lacking about the PAHs degradation kinetics, mechanisms, and pathways in the presence of the dispersant. Moreover, the influences of many other factors such as pH, ionic strength (IS), temperature, and HA on PAHs degradation in the presence of oil dispersant have not been explored.

1.4 Objectives

The overall goal of this research is to 1) demonstrate and evaluate the performance of a new class of sodium carboxymethyl cellulose (CMC) stabilized iron sulfide (FeS) nanoparticles as a “green” (environmental friendly) and effective *in situ* strategy to immobilize Hg in water and soil/sediment, and 2) investigate effects of a model oil dispersant (Corexit EC9500A) on the

physicochemical processes and reactions of persistent oil components PAHs in the Gulf Coast ecosystems. The specific objectives are to:

- Develop and characterize a new class of CMC-stabilized FeS nanoparticles that are physically more dispersible and chemically more reactive than current non-stabilized FeS particles;
- Elucidate the underlying particle stabilization mechanisms through physical and chemical characterizations of CMC-FeS nanoparticles;
- Evaluate effects of various parameters such as reaction time, stabilizer concentration, pH, chloride, DOM, and IS on the effectiveness of aqueous Hg^{2+} removal by CMC-FeS nanoparticles;
- Investigate the effectiveness of the nanoparticles for immobilization (defined as reduction in solubility and leachability) of Hg in three high-profile, paradigm field soils and sediments;
- Determine the transport behavior of the nanoparticles in the field soils and sediments;
- Determine effects and mechanisms of the oil dispersant Corexit EC9500A on sorption and desorption isotherms and kinetics of PAHs with representative Gulf Coast marine sediments;
- Evaluate effects of water accommodated oil (WAO) and dispersed WAO (DWAO) on sediment sorption of PAHs;
- Explore effects of Corexit EC9500A on UV- or sunlight-facilitated photodegradation of PAHs in surface seawater;
- Elucidate mechanisms underlying photochemical degradation in regard to radicals and reactive intermediates; and

- Evaluate impact of water chemistry (i.e. salinity, IS, HA, and temperature) on the photodegradation of PAHs in the dispersant solution.

The CMC-stabilized FeS nanoparticles are designed to be deliverable into contaminated soil/sediment to facilitate *in situ* immobilization of Hg. The studies on Hg immobilization by the nanoparticles can well address the potential and viability issues of the nanoparticles. The research will examine the performance of the nanoparticles under typical natural water environments and in field Hg-contaminated soils and sediments. The results can provide solid scientific evidence that CMC-stabilized FeS nanoparticles are promising for *in situ* immobilization of Hg.

To facilitate scientifically sound assessment of the long-term environmental impact of the oil spill, it is of critical importance to acquire solid data on the fate and transport of persistent oil components under relevant environmental conditions. However, there has been no knowledge available about the roles of oil dispersants. For the first time, our study will investigate effects of oil dispersant on sorption/desorption kinetics, equilibrium, and mechanisms of dispersed oil to sediments, as well as photochemical degradation. The results can fill in the knowledge gaps, have an implication on how dispersants affect distribution and transport of oil in the marine environment, and provide compelling scientific basis for decision makers.

1.5 Organization

This dissertation includes six chapters. Except for Chapter 1 (General Introduction) and Chapter 6 (Conclusions and Suggestions for Future Research), each chapter of this dissertation is formatted in the journal style of Water Research. **Chapter 1** gives a general introduction of the background and outlines the objectives of this dissertation. **Chapter 2** describes the synthesis and characterization of a new class of CMC-stabilized FeS nanoparticles. The nanoparticles are

tested for removal of aqueous mercury (Hg^{2+}) as a function of CMC concentration, reaction time, pH, chloride, DOM/HA, and IS. This chapter is based on the information that has been published in Environmental Science & Technology (Gong et al., 2014). **Chapter 3** describes the *in situ* immobilization of mercury by CMC-stabilized FeS nanoparticles in high-profile, paradigm field soils and sediments through batch and column experiments. The transport behavior of the nanoparticles in soils/sediments is also investigated. This chapter is based on the information that has been published in Nanotechnology (Gong et al., 2012). **Chapter 4** investigates effects and mechanisms of a model oil dispersant (Corexit EC9500A) on sorption/desorption of phenanthrene with two Gulf Coast marine sediments. This chapter is based on the information that has been published in Environmental Pollution (Gong et al., 2014). **Chapter 5** evaluates effects of the oil dispersant Corexit EC9500A on the UV/sunlight-facilitated photochemical degradation of pyrene in surface seawater. The photodegradation mechanisms with and without dispersant and water chemistry (i.e., IS, pH, HA and temperature) effects on the degradation of pyrene in the dispersant solution are well studied. **Chapter 6** gives a summary of major conclusions of this research and suggestions for future work.

Chapter 2. Immobilization of Mercury by Carboxymethyl Cellulose Stabilized Iron Sulfide Nanoparticles: Reaction Mechanisms and Effects of Stabilizer and Water Chemistry

This chapter studied the feasibility of using sodium carboxymethyl cellulose (CMC) as a green stabilizer to prepare fully stabilized iron sulfide (FeS) nanoparticles. The resultant nanoparticles were characterized with X-ray diffractograms (XRD), fourier transform infrared spectroscopy (FTIR), transmission electron microscope (TEM), dynamic light scattering (DLS), and zeta potential. The underlying mechanism governing immobilization of mercury by CMC-stabilized FeS nanoparticles was examined. Effects of reaction time, CMC concentrations, pH, chloride, dissolved organic matter (DOM)/humic acid (HA), and ionic strength (IS) on the effectiveness of aqueous Hg^{2+} removal were explored. The aging effects on Hg^{2+} immobilization by the nanoparticles, and long-term stability of the nanoparticles were also investigated.

2.1 Introduction

Mercury is a pervasive, persistent and extremely toxic contaminant widely found in surface waters and groundwater (Danwanichakul and Danwanichakul, 2009). Due to its bioaccumulation potential, mercury concentrations along the food chain can reach up to 5000 times greater than the surrounding waters (Holmes et al., 2009; Sarkar et al., 2000). Adverse health effects from mercury exposure include damage of the central nervous system and the gastrointestinal tract, mental and motor dysfunction, impairment of pulmonary and kidney function, and chest pain (Bayramoglu and Arica, 2007; Mercone et al., 1999; Sweet and Zelikoff, 2001). Mercury is included on the list of priority pollutants by U.S. Environmental Protection Agency (USEPA)

with a mandatory discharge limit of 10 µg/L for wastewater (Nam et al., 2003), and a maximum contaminant level (MCL) of 2 µg/L in drinking water (USEPA, 2009).

In aquatic systems, mercury can exist in elemental, inorganic, and organic forms (Wang et al., 2004). Elemental mercury (Hg^0) has high volatility and relatively low water solubility (Lindqvist and Rodhe, 1985). Aqueous inorganic mercury has two oxidation states, 1+ and 2+, with Hg^{2+} being the most predominant form in natural waters (Lyons et al., 1998). The most important organic form of mercury is the methylated mercury or methylmercury (MeHg), which has been known to be the key Hg species that is not only highly toxic, but accumulates over the food chain (Wang et al., 2004). As MeHg is often formed via biological methylation of inorganic mercury species, the key to control human exposure is to restrain the mercury methylation process by removing the bioavailable inorganic mercury species (Xiong et al., 2009).

Various engineered technologies have been studied for mercury removal from water, including coagulation (Zhang et al., 2005), chemical precipitation (Blue et al., 2010), cementation (Ku et al., 2002), ion exchange (Neagu et al., 2007), solvent extraction (Fábrega and Mansur, 2007) and adsorption (Mohan et al., 2000). Adsorption with fixed or mobile natural adsorbents has been considered to largely control the fate and transport of mercury in natural waters (Bower et al., 2008). Naturally occurring sulfide minerals, such as pyrite (FeS_2), pyrrhotite (Fe_{1-x}S), and mackinawite (FeS) have been recognized as important scavengers for mercury (Behra et al., 2001; Brown et al., 1979). Mercury is a soft Lewis acid, and thus, it can interact strongly with a soft Lewis base such as sulfur (Gong et al., 2012). Mercury in the aqueous environment can be immobilized through formation of mercury sulfide, which is virtually insoluble with a solubility product constant (K_{sp}) of 2×10^{-54} for red cinnabar or $\alpha\text{-HgS}$ (Paquette and Helz, 1995) and 4×10^{-54} for black metacinnabar or $\beta\text{-HgS}$ (Benoit et al., 1999;

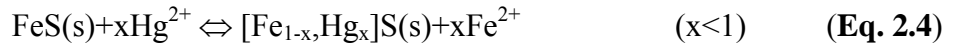
Ravichandran et al., 1999). Hg^{2+} can react with FeS(s) ($K_{\text{sp}} = 8 \times 10^{-19}$) to form a separate phase of metacinnabar ($\beta\text{-HgS}$) in the presence of natural organic matter (Skylberg and Drott, 2010).

Synthetic FeS displays a disordered tetragonal mackinawite structure, with an average primary particle size equivalent to a crystallite size of 4 nm and a corresponding specific surface area of $350 \text{ m}^2/\text{g}$ (Wolthers et al., 2003). FeS can effectively remove divalent metals such as Cd^{2+} , Co^{2+} , Zn^{2+} , and Ni^{2+} through adsorption and coprecipitation (Morse and Arakaki, 1993; Wharton et al., 2000; Wolthers et al., 2003). Mercuric ion can be immobilized by FeS particles through chemical precipitation, ion exchange, and surface complexation by the reactions as follows (Jeong et al., 2007; Morse and Luther, 1999; Skylberg and Drott, 2010; Wolfenden et al., 2005):

a) Precipitation of HgS(s) following partial dissolution of FeS (Skylberg and Drott, 2010)



b) Substitution of Hg^{2+} with FeS (Jeong et al., 2007)

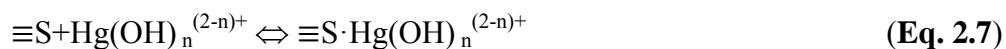


c) Complexation of Hg^{2+} with reactive surface sites on FeS (Jeong et al., 2007)



Jean and Bancroft (1986) suggested that adsorption of mercury by iron sulfides consists of two steps: 1) hydrolysis of mercury ions, which exerts a significant role when initiating the adsorption, and 2) adsorption specifically on the surface sulfide groups up to an approximately monolayer coverage, i.e.,





Compared to bulk particles or natural minerals, nanoscale FeS particles are expected to offer much greater sorption capacity due to their larger specific surface area. Our recent work (Xiong et al., 2009) indicated that a polysaccharide stabilizer, known as carboxymethyl cellulose (CMC), can effectively prevent agglomeration of FeS particles, and thereby facilitate preparation of highly stable, discrete FeS nanoparticles. Our preliminary results demonstrated that the stabilized nanoparticles are able to effectively immobilize Hg^{2+} pre-spiked in marine sediments. However, detailed investigation into the effects of particle stabilization on the removal of Hg^{2+} in the aqueous solution has been lacking. Moreover, as many other factors such as pH, chloride, dissolved organic matter (DOM), and ionic strength have been reported to affect the reactivity of FeS minerals or aggregated FeS particles (Jeong et al., 2007; Liu et al., 2008), the influences of these factors on Hg^{2+} removal by CMC-stabilized FeS (CMC-FeS) nanoparticles have not yet been explored.

The overall goal of this study was to determine the mechanisms governing removal of Hg^{2+} by CMC-FeS nanoparticles and examine the effects of the stabilizer and water chemistry. The specific objectives were to: 1) prepare and characterize CMC-FeS nanoparticles in the presence of various concentrations of CMC, and elucidate the mechanisms governing the particle stabilization; 2) examine the effects of reaction time, stabilizer concentration, pH, chloride, DOM/HA, and IS on the effectiveness of aqueous Hg^{2+} removal; 3) acquire further insights into the underlying Hg^{2+} immobilization mechanisms; and 4) test the aging effects on Hg^{2+} immobilization by the nanoparticles and long-term stability of the nanoparticles.

2.2 Materials and Methods

2.2.1 Chemicals

All chemicals were in the analytical grade or higher, and used as received. Iron sulfate heptahydrate ($\text{FeSO}_4 \cdot 7\text{H}_2\text{O}$), mercury nitrate monohydrate ($\text{Hg}(\text{NO}_3)_2 \cdot \text{H}_2\text{O}$), CMC (M.W. = 90,000 in the sodium form, degree of substitute = 0.7), and humic acid (HA) (sodium salt, 50~60% as humic acid, CAS 68131-04-4) were purchased from Acros Organics (Morris Plains, NJ, USA). According to the manufacture, the HA was extracted from lignite and has an approximate molecular weight of 226. Sodium sulfide nonahydrate ($\text{Na}_2\text{S} \cdot 9\text{H}_2\text{O}$), sodium nitrate (NaNO_3), sodium hydroxide (NaOH), sodium chloride (NaCl) were obtained from Fisher Scientific (Fair Lawn, NJ, USA). Nitric acid was obtained from Mallinckrodt Chemical (St. Louis, MO, USA).

2.2.2 Preparation of CMC-FeS nanoparticles

CMC-FeS nanoparticles were prepared following the method by Xiong et al. (2009). **Figure 2-1** depicts the scheme for synthesizing CMC-FeS nanoparticles. In each batch, 150 mL suspension of CMC-FeS was prepared in a 250 mL flask attached to a vacuum line. First, a CMC stock solution (1%, w/w) was prepared with DI water. Then, 7.5 mL of the stock solution was added into 112.5 mL DI water and the mixture purged with purified N_2 (>99%) for 15 minutes to remove dissolved oxygen (DO). Meanwhile, solutions of 0.043 M FeSO_4 (20 mL) and 0.085 M Na_2S (20 mL) were prepared with N_2 -purged DI water right before use. Under N_2 purging, the FeSO_4 solution (20 mL) was added to the CMC solution to yield a solution with a 0.006 M of Fe^{2+} and 0.054% of CMC. The mixture was then purged with N_2 for 5 minutes to assure complete mixing and formation of Fe^{2+} -CMC complexes. Then, the Na_2S solution (10 mL) was introduced into the solution dropwise under shaking at 150 rpm and vacuum through a burette at an Fe-to-S molar ratio of 1:1. To ensure complete reaction, the system was shaken for

another 5 minutes. The particles were then sealed and aged for 24 hours before use. The resultant nanoparticle suspension contained 0.05 wt.% of CMC and 500 mg/L FeS (i.e. a CMC-to-FeS molar ratio of 0.0010), which was used in characterization and experiments unless indicated otherwise. The soluble S^{2-} concentration in the suspensions was determined to be 4.24 ± 0.16 and 0.96 ± 0.15 mg/L, respectively, for bare and CMC-stabilized FeS (upon filtration of the suspensions through a 25 nm membrane filter).

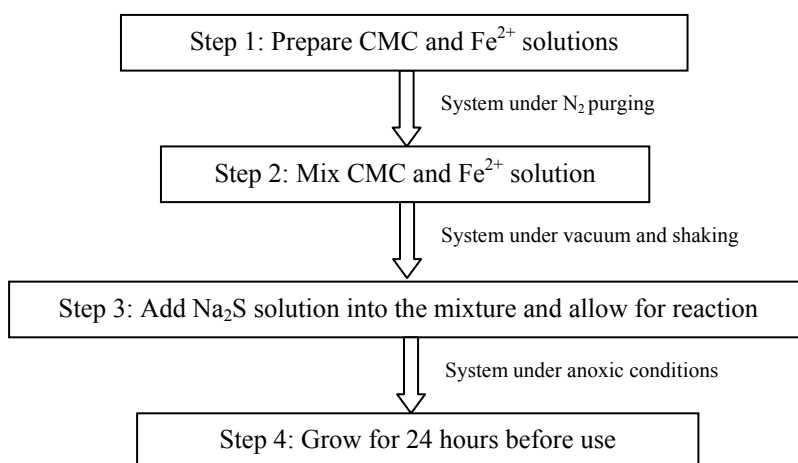


Figure 2-1. Procedure for synthesizing CMC-stabilized FeS nanoparticles.

2.2.3 Characterization of CMC-FeS nanoparticles

The chemical composition and crystallographic structure of the CMC-FeS nanoparticles before and after mercury sorption and the sorbed mercury species were examined by X-ray powder diffraction (XRD) using a Miniflex Diffractometer (9009 New Trials, Rigaku Americas Corporation, Woodlands, TX, USA) with Cu K α ($\lambda=1.54056\text{\AA}$) radiation. The nanoparticles before mercury sorption were prepared at 12 mg/L as FeS with a CMC-to-FeS molar ratio of 0.0010 in 1 L suspension. The nanoparticles after mercury sorption were prepared following the procedure as described in Section 2.2.5 with an equilibration time of 48 h with Hg^{2+} . For XRD

analysis, the nanoparticles were collected by filtering the suspensions using a 25 nm membrane filter of mixed cellulose esters (Millipore Corp., Billerica, MA, USA). The solids were then rinsed three times with N₂-purged DI water, and subsequently freeze-dried under vacuum at -50 °C using a VirTis Freezemobile freeze dryer (Gardiner, NY, USA) for 48 h. For comparison, non-stabilized FeS particles were prepared without the stabilizer but under otherwise identical conditions. The samples were placed in a zero background sample holder and scanned from 10° to 80° 2θ angles using a step interval of 0.02° and a scan speed of 5°/min. The XRD patterns were processed using the computer program known as MDI Jade 6.5 loaded with ICDD database (Materials Data Inc., Livermore, CA, USA).

The specific surface area of freeze-dried bare FeS particles as described above was measured following the multipoint N₂-BET adsorption method (Autosorb1, Quantachrome Instruments, Boynton Beach, FL, USA).

Fourier transform infrared (FTIR) spectroscopy measurements were carried out to explore interactions between CMC and FeS, and between mercury and CMC-FeS. To this end, the freeze-dried samples were mixed with KBr powder to form thin KBr pellets consisting of 2 wt.% of the nanoparticles. FTIR spectra were then obtained using a SHIMADZU IRPrestige-21 spectrometer (Shimadzu Scientific Instruments, Columbia, MD, USA). A pure KBr pellet was used as background to obtain the net FTIR spectra of the samples. For comparison, FTIR spectra for neat CMC and non-stabilized FeS particles were also acquired in the same manner.

Transmission electron microscopy (TEM) images were obtained using a Zeiss EM10 transmission electron microscope (Zeiss, Thornwood, NJ, USA) operated at 60 kV. First, a 10 μL of aqueous sample was placed on a Formvar-carbon coated copper grid (Electron Microscopy Sciences, Hatfield, PA, USA). Second, the droplet was allowed for full contact/spreading on the

grid and vacuum dried for 12 hours. The residual particles attached to the grid were then imaged. The TEM images were analyzed using a specialty image processing software named ImageJ, which also gave the particle size distribution. TEM images for bare FeS were obtained as well following the same procedure described above except that bare FeS was first subjected to sonication with a Fisher Scientific FS28 Ultrasonic Cleaner (Fisher Scientific, Fair lawn, NJ) for 10 minutes before the imaging.

Dynamic light scattering (DLS) tests of the FeS particles were performed with a Malvern Zetasizer Nano ZS (Malvern Instruments, Worcestershire, UK)). The DLS data were processed and analyzed with a software package (Zetasizer Nano series software Version 6.12, Worcestershire, UK) to yield number-weighted particle size distributions and zeta potentials. Suspension viscosity was measured with a Gilmont falling-ball viscometer (Barnant Company, Barrington, IL, USA) and used to correct for the influence of viscosity on the DLS measurements.

2.2.4 Effects of CMC concentration on stability of FeS nanoparticles and mercury sorption

To test the effects of the CMC stabilizer, FeS particles were prepared at a fixed FeS concentration of 500 mg/L as FeS but with various concentrations of CMC, namely, at CMC-to-FeS molar ratios of 0, 0.0001, 0.0002, 0.0006, 0.0010, 0.0016, 0.0020, 0.0025. The freshly prepared particles were sealed and aged for 24 h before characterization measurements or mercury sorption tests. To quantify the stability/settleability of the nanoparticles, the supernatants of the 24 h aged samples were sampled and digested with 12 M HCl (4 mL of HCl for 1 mL sample) for 5 min, which was able to completely dissolve the nanoparticles, and then analyzed for total iron. To determine CMC effects on mercury removal, sorption tests were

carried out with these FeS particles following the procedures as for the kinetic tests described in Section 2.2.5 with a fixed reaction time of 48 h.

2.2.5 Mercury sorption kinetic tests

Batch kinetic experiments of mercury sorption by CMC-FeS (prepared at a CMC-to-FeS molar ratio of 0.0010) were carried out in sealed 30 mL Teflon vials under anoxic conditions. The initial concentrations of Hg^{2+} and CMC-FeS nanoparticles were set at 40 mg/L and 12 mg/L, respectively. In all cases, 0.1 M of NaNO_3 was added in the suspensions to simulate real water ionic strength (note the suspension also contained 2.72×10^{-4} M Na^+ , 1.36×10^{-4} M SO_4^{2-} , and 4×10^{-4} M NO_3^- ions from the precursor chemicals). The pH of the mixture was adjusted to 7.0 with HNO_3 (1 M, 0.1 M) and/or NaOH (1 M, 0.1 M). To avoid oxidation of the nanoparticles, the preparations were conducted under the protection of purified N_2 (>99%). The reaction was initiated by adding a Hg^{2+} stock solution in the nanoparticle suspensions, and the vials were then sealed and agitated on an end-to-end rotator running at 30 rpm at room temperature (20 ± 1 °C). Mercury removal was followed for 20 h by measuring aqueous Hg^{2+} remaining. At predetermined times, duplicate vials were sacrificially sampled. Upon pH measurement, the samples were filtered through the 25 nm membrane filters, and then analyzed for mercury concentration in the filtrates. Separate tests confirmed that the membrane filters were able to completely remove the nanoparticles, but did not retain any soluble mercury in the solution. To investigate effects of aging time on mercury sorption and long-term stability of sorbed mercury, some of the kinetic experiments were extended to 15, 60, 100, and 912 days.

2.2.6 Mercury sorption isotherm tests

Mercury sorption isotherms with CMC-FeS were constructed by carrying out equilibrium sorption experiments in 30 mL Teflon vials in duplicate. The experimental conditions were:

$\text{NaNO}_3 = 0.1 \text{ M}$, $\text{FeS} = 2.5 \text{ mg/L}$, CMC-to-FeS molar ratio = 0.0010, initial $\text{Hg}^{2+} = 4.8$ to 40 mg/L (i.e. Hg-to-FeS molar ratio = 0.84 to 7), and final $\text{pH} = 7.0$. The vials were equilibrated for 48 h in the same manner as in the kinetic tests. The equilibrium mercury uptake was calculated based on the differences between the initial and final concentrations of mercury in the aqueous phase. Control tests conducted in the absence of CMC-FeS nanoparticles showed that loss of mercury onto the vial walls and membrane filter was $<2\%$ for all cases.

2.2.7 Effects of pH, Cl^- , DOM/HA, and IS

Batch equilibrium sorption tests were conducted in 43 mL Teflon vials to investigate the effects of pH, Cl^- , DOM/HA, and IS on Hg^{2+} sorption by CMC-FeS. Each vial was loaded with 12 mg/L of the nanoparticles, 40 mg/L of Hg^{2+} , and 0.1 M NaNO_3 with an initial pH of 7.0 ± 0.3 . To test the pH effect, the initial pH of the mixture was adjusted to a range of 5 to 10. To examine the Cl^- effect, various concentrations of chloride (0, 11, 106, 355, 1775, 3550, and 7100 mg/L) were obtained by adding different volumes of a NaCl solution (2.0 M) into the suspensions. To probe the DOM effect, DOM was extracted from an organic soil purchased from a local Walmart store (Auburn, AL, USA) by DI water. Briefly, 600 g of the soil was mixed with 600 mL DI water to extract soluble organic carbon. After rotating on an end-to-end tumbler continuously for 7 days, the mixture was centrifuged at 6000 g force for 10 min, and the supernatant was filtered through a 0.45 μm Millipore membrane of cellulose esters. The filtrates were measured for total organic carbon (TOC). Batch sorption tests were then carried out in the presence of various concentrations of DOM (0, 1, 7.1, 9.83, 20 mg/L as TOC). In addition, the tests were also conducted in the presence of a standard reference HA (0, 0.05, 1, 5.5, 28 mg/L as TOC). The ionic strength effect was tested by adding various concentrations of NaNO_3 (0, 0.02, 0.05, 0.1, and 0.2 M) in the batch reactors.

In all cases, mercury removal was obtained from differences between the initial and final concentrations of mercury in the aqueous solution. Control tests were conducted in the absence of CMC-FeS nanoparticles but otherwise identical conditions. The geochemical modeling software Visual MINTEQ (version 2.61) was used to simulate the equilibrium speciations of FeS and Hg^{2+} as a function of pH, and the complexation of Hg^{2+} with Cl^- .

2.2.8 Analytical methods

Solution or suspension pH was measured using an Oakton pH meter (pH 510 Benchtip Meter, Oakton, CA, USA). Mercury concentration was analyzed via the cold vapor atomic absorption (CVAA) method (EPA Method 7470A and 7471A) using a Varian SpectrAA 220FS atomic absorption spectrometer (Varian, Canton, MA, USA) equipped with a cold vapor generator using SnCl_2 as a reductant. Prior to analysis, all samples were first preserved and oxidized with 1% BrCl . The residual BrCl was scavenged using 1% hydroxylamine hydrochloride. The detection limit of total mercury was 0.5 $\mu\text{g/L}$ (at a sample volume of 10 mL). Total iron concentration was analyzed with a flame atomic absorption spectrometer (Varian SpectrAA 220FS, Varian, Canton, MA, USA), which has a detection limit of 0.05 mg/L. DOM/HA concentrations were determined as TOC by a Tekmar Dohrmann Pheonix 8000 UV-Persulfate TOC analyzer (Mason, OH, USA) with a detection limit of 0.1 mg/L. Cl^- was analyzed using a Dionex ion chromatography system (Dionex, Sunnyvale, CA, USA) equipped with an AS14 column (the detection limit was 0.5 mg/L at a sample volume of 1 mL). Sulfide was measured following the standard iodometric method with a detection limit of 0.5 mg/L.

2.3 Results and discussion

2.3.1 Characterization of CMC-FeS Nanoparticles

Figure 2-2 shows the XRD diffractograms of neat CMC and the synthesized FeS particles with or without CMC. For bare FeS, a peak at $2\theta = 16.8^\circ$ was evident, which can be attributed to the FeS particles (Liu et al., 2008; Rickard and Morse, 2005; Wolthers et al., 2003). However, the peak for CMC-FeS at the same 2θ value was much weakened. The phenomenon can be attributed to: a) the much smaller particle size of CMC-FeS, and 2) CMC's inhibitive effect on the growth of FeS crystals during the nucleation stage of CMC-FeS. Note that the characteristic peaks of CMC at 20.4° and 40.9° became inconspicuous for the CMC-FeS nanoparticles.

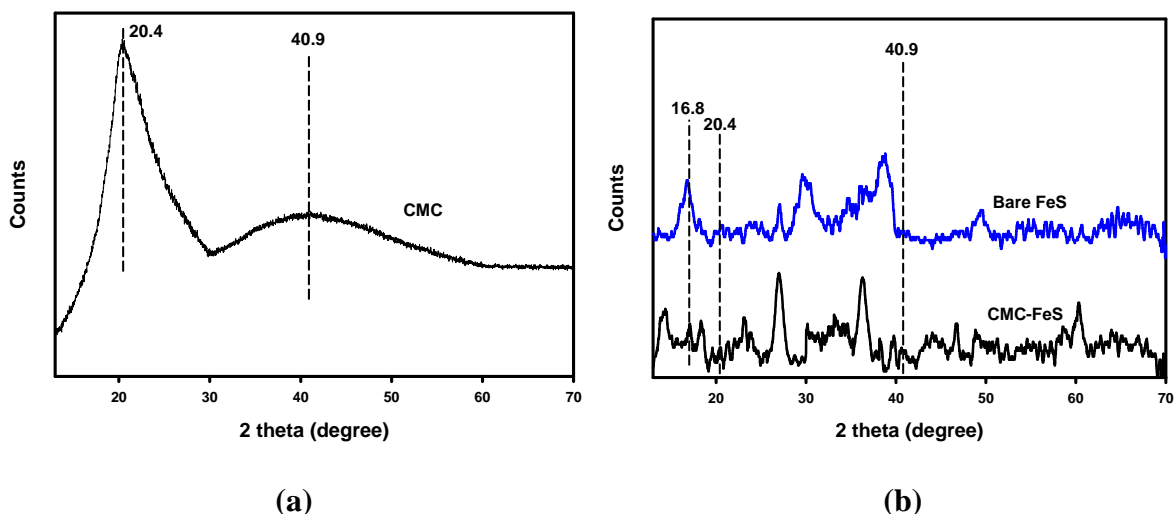
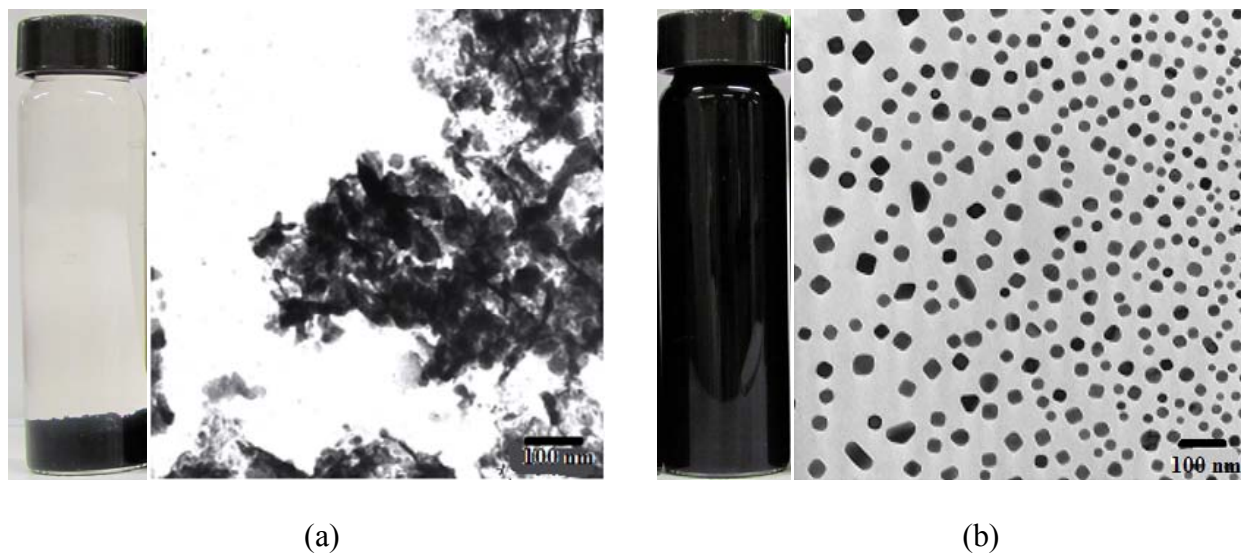


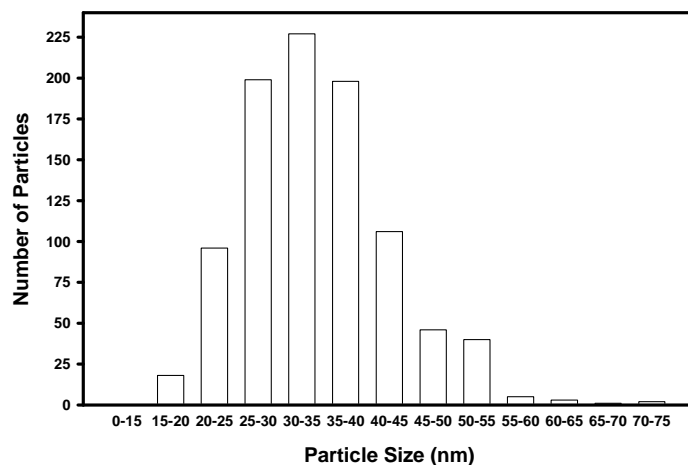
Figure 2-2. XRD spectra for: (a) neat CMC powders, and (b) bare FeS and CMC-FeS nanoparticles. Bare FeS was prepared at 0.5 g/L without CMC, while CMC-FeS was prepared at 0.5 g/L with 0.05 wt% CMC.

Figures 2-3a-b presents images of bare FeS and CMC-FeS. While bare FeS aggregated and precipitated within five minutes, CMC-FeS remained dispersed in water. As shown in the TEM

images, while bare FeS was present as aggregated flocs, CMC-FeS appeared as clearly defined and discrete nanoparticles. Interestingly, the shapes of the CMC-FeS were rather diverse, including spheres, squares, rods, diamonds and triangles. Evidently, the presence of CMC suppressed the growth and aggregation of FeS, and thus, maintained a higher surface area of the particles. The particles were rather poly-dispersed with a size spanning from 15 to 75 nm and a mean size of 34.31 ± 8.34 nm (standard deviation) (**Figure 2-3c**).

While TEM images show the true shape and morphology of the nanoparticles, DLS measurements give hydrodynamic diameters of the particles with the attached stabilizer in situ. As DLS is based on particle diffusivity, the DLS-based size is more relevant to particle transport behavior. For CMC-FeS, the hydrodynamic diameter was measured to be 222.5 ± 3.2 nm (99.9% particles by number), compared to 1632.0 ± 7.0 nm for sonicated bare FeS.





(c)

Figure 2-3. Digital photographs and TEM images of (a) bare FeS aggregates, (b) CMC-FeS nanoparticles (FeS = 0.5 g/L, CMC = 0.05%), and (c) particle size distribution of CMC-FeS nanoparticles based on a random sample of 941 particles from 3 TEM images.

2.3.2 Interactions between CMC and FeS and nature of Hg^{2+} uptake by CMC-FeS

Complete particle stabilization was achieved at a CMC-to-FeS molar ratio of 0.0010. Analysis of the supernatants FeS indicated that after 24 h of standstill, 100% of CMC-FeS nanoparticles remained in the supernatant, while 97% of non-stabilized FeS particles settled by gravity.

To gain insight into the interactions between functional groups of CMC and the nanoparticles, FTIR analysis was performed on neat CMC powder, bare FeS particles, and CMC-FeS. **Figure 2-4** presents the characteristic stretching frequencies of neat CMC, bare FeS, and CMC-FeS. For bare FeS, no stretching frequency was observed in the tested range from 500 to 4000 cm^{-1} , indicating that bare FeS is free of organic compounds (Austin, 2012). In contrast, for CMC-FeS, four strong peaks were observed at the wave numbers of 3368, 1590, 1412 and 1050 cm^{-1} ,

respectively, which are attributed to interactions between COO^- (1590 and 1412 cm^{-1}) or $-\text{OH}$ groups (3368 and 1050 cm^{-1}) and Fe^{2+} (He et al., 2007). The $-\text{OH}$ stretching band shifted from 3523 cm^{-1} for neat CMC to 3368 cm^{-1} for CMC-FeS, which is ascribed to enhanced intermolecular hydrogen bonds between CMC and the FeS surface (Sylvestre et al., 2004). The band observed at 2922 cm^{-1} for neat CMC was shifted to 2879 cm^{-1} upon sorption of CMC to the FeS particles, which indicates the C-H stretching vibration from the CH_2 groups of the stabilizer (Maity and Agrawal, 2007). The bands at 1605 , 1422 and 1060 cm^{-1} for neat CMC are assigned to asymmetric and symmetric vibration of COO^- groups and C-O stretching (RCH_2OH) (Brown et al., 1988). Likewise, these peaks were shifted to 1590 , 1412 and 1050 cm^{-1} , respectively, for CMC-FeS. The wave number separation (Δ) between the asymmetric $\nu_{\text{as}}(\text{COO}^-)$ (1590 cm^{-1}) and symmetric $\nu_{\text{s}}(\text{COO}^-)$ (1412 cm^{-1}) stretches is 178 cm^{-1} , which suggests that the primary mechanism for binding CMC to FeS was bidentate bridging (He et al., 2007; Nakamoto, 1997).

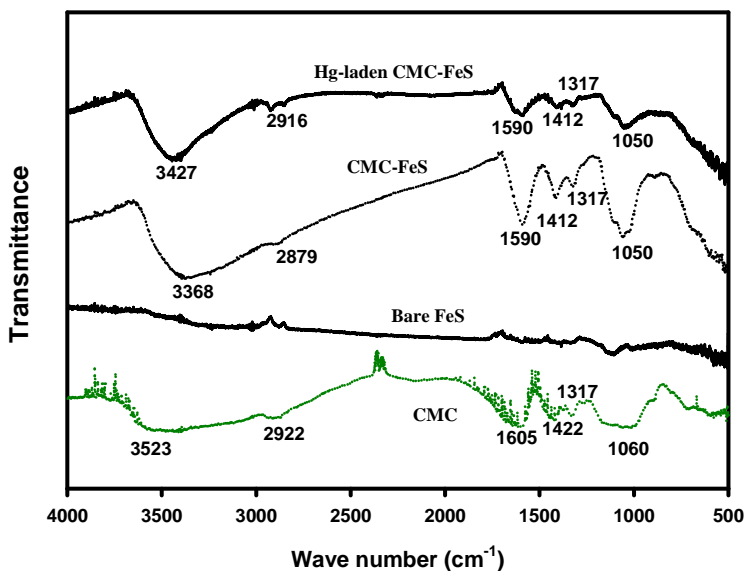


Figure 2-4. FTIR spectra of neat CMC powder, non-stabilized FeS particles, CMC-FeS nanoparticles, and Hg^{2+} -laden CMC-FeS. Non-stabilized-FeS preparation: Initial FeS = 12 mg/L,

and solution pH = 7.0; CMC-FeS was prepared in the presence of 0.0012 wt.% of CMC under otherwise identical conditions; and Hg²⁺-laden CMC-FeS was prepared by equilibrating the same CMC-FeS with 40 mg/L of Hg²⁺.

Based on the FTIR results, it appears plausible that the stabilization of the FeS particles is facilitated through adsorption of CMC molecules onto the surface of the nanoparticles via carboxylate and hydroxyl groups. The partial encapsulation of the nanoparticles with a thin layer of negatively charged CMC induces a strong negative potential that prevents aggregation of the like particles. The CMC-induced negative potential was revealed by the highly negative ζ potential between -43 and -68 mV over the pH range of 5-11, the surface remained negative at pH as low as 2.5 ($\zeta \approx -22$ mV). Therefore, CMC stabilizes the nanoparticles through concurrent electrostatic repulsion and steric hindrance.

Upon Hg uptake, the FTIR spectra (**Figure 2-4**) of CMC-FeS showed similar absorption band characteristics described earlier, namely, -OH group (3427 cm⁻¹), C-H stretching (2916 cm⁻¹), asymmetric and symmetric stretches of COO⁻ groups (1590 and 1412 cm⁻¹), and C-O stretching (RCH₂OH) (1050 cm⁻¹). Yet, the -OH stretching band shifted from 3368 cm⁻¹ for CMC-FeS to 3427 cm⁻¹ for Hg²⁺-laden CMC-FeS, and the C-H stretching vibration shifted from 2879 cm⁻¹ to 2916 cm⁻¹. Meanwhile, the IR frequencies of asymmetric and symmetric stretches of COO⁻ groups (1590 and 1412 cm⁻¹), and C-O stretching (RCH₂OH) (1050 cm⁻¹) were decreased by 60%, 67% and 63%, respectively, upon mercury uptake. These changes can be attributed to surface complexation between CMC-FeS nanoparticles and mercury. There was no new band observed in the wave number range of 500-4000 cm⁻¹ upon Hg²⁺ loading. However,

this does not rule out the formation of HgS because the characteristic absorption bands for HgS are known to be in the range of 83 to 100 cm^{-1} (Ross, 1972).

2.3.3 Effects of CMC concentration on nanoparticle stability and Hg sorption capacity

Figure 2-5 shows the effects of CMC concentration on physical stability of FeS nanoparticles. After 24 h of settling by gravity, 97% of non-stabilized FeS particles (CMC = 0) settled, compared to 87% and 9% sedimentation at a CMC concentration of 0.005 wt% and 0.01 wt%, respectively. In contrast, when the CMC concentration was increased to 0.03 wt% or higher, the particles were fully stabilized (i.e., 100% of particle suspension was achieved). Thus, 0.03 wt% (or CMC-to-FeS molar ratio = 0.0006) was regarded as the critical stabilization concentration (CSC), defined as the minimum CMC needed to fully stabilize the nanoparticles.

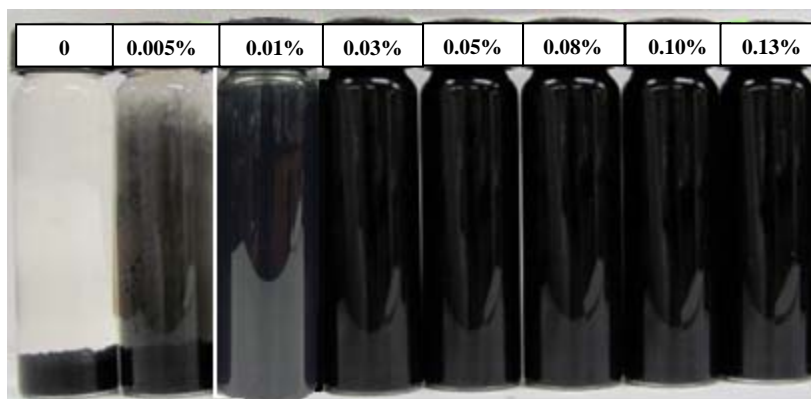


Figure 2-5. Aqueous suspensions of FeS particles prepared at 500 mg/L as FeS in the presence of various concentrations of CMC: 0, 0.005, 0.01, 0.03, 0.05, 0.08, 0.10, and 0.13 wt% (or CMC-to-FeS molar ratios: 0, 0.0001, 0.0002, 0.0006, 0.0010, 0.0016, 0.0020, and 0.0025). Pictures were taken 24 hours after synthesis.

Figure 2-6 compares the volume-weighted hydrodynamic diameters of bare and fully stabilized FeS particles. After 24 h of standstill, the hydrodynamic diameter of the bare FeS

particles was 1,632 nm, compared to 253, 223, and 166 nm, respectively, for the particles which were fully stabilized at a CMC-FeS molar ratio of 0.0006, 0.0010 and 0.0025. After 6 months of aging, the stabilized nanoparticles remained fully suspended, though the hydrodynamic diameter grew slightly to 359, 246, and 234 nm, respectively (1,779 nm for the bare particles). Evidently, increasing CMC concentration above the CSC value resulted in only modest decrease in the hydrodynamic diameters.

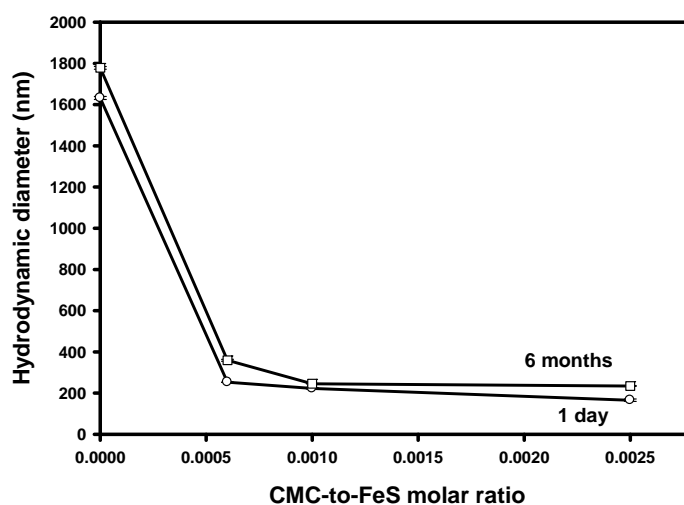


Figure 2-6. Volume weighted hydrodynamic diameters of FeS particles prepared at 500 mg/L as FeS and at various CMC-to-FeS molar ratios, when aged for 1 day and 6 months. Data are plotted as mean of duplicates and error bars (calculated as standard error) indicate data reproducibility.

Figure 2-7 shows effect of the stabilizer concentration on the equilibrium uptake of Hg^{2+} by FeS particles. Hg^{2+} uptake increased with increasing CMC-to-FeS molar ratio from 0 to 0.0004, reaching a peak uptake at CMC-to-FeS molar ratios of 0.0006-0.0010. Compared to bare FeS, fully stabilized FeS nanoparticles offered 20% greater Hg^{2+} uptake. However, further increasing

the CMC-FeS ratio above 0.0010 inhibited Hg^{2+} uptake. For instance, Hg^{2+} uptake was reduced by 14% when the CMC-FeS ratio was elevated from 0.0010 to 0.0025.

It is evident from **Figure 2-6** that increasing CMC concentration resulted in smaller FeS particles, and thus, greater specific surface area and more sorption sites. The specific surface area (S , m^2/g) of the FeS particles is inversely related to the radius (r , m) of nanoparticles (He and Zhao, 2005; Kecskes et al., 2003):

$$r=3(\rho*S)^{-1} \quad \text{(Eq. 2.8)}$$

where ρ is the density of FeS ($4,740 \text{ kg}/\text{m}^3$). Based on the mean particle size of 34.3 nm measured by TEM (Gong et al., 2012), the nanoparticles at a CMC-to-FeS molar ratio of 0.0010 had an S value of $36.9 \text{ m}^2/\text{g}$, compared to $16.7 \text{ m}^2/\text{g}$ for bare FeS. Therefore, the particle stabilization technique not only facilitates soil delivery of the nanoparticles (Xiong et al., 2009), but also increases sorption capacity. Conversely, excessive uptake of CMC molecules on the particle surface results in a denser CMC coating on the nanoparticles, which may inhibit access of Hg^{2+} to the particles' surface sites due to elevated mass transfer resistance and/or blockage of the sorption sites (He and Zhao, 2008). Taken together both mercury sorption capacity and physical stability of the FeS particles, the optimum CMC-to-FeS ratio was determined to be 0.0010, which was used in the subsequent tests.

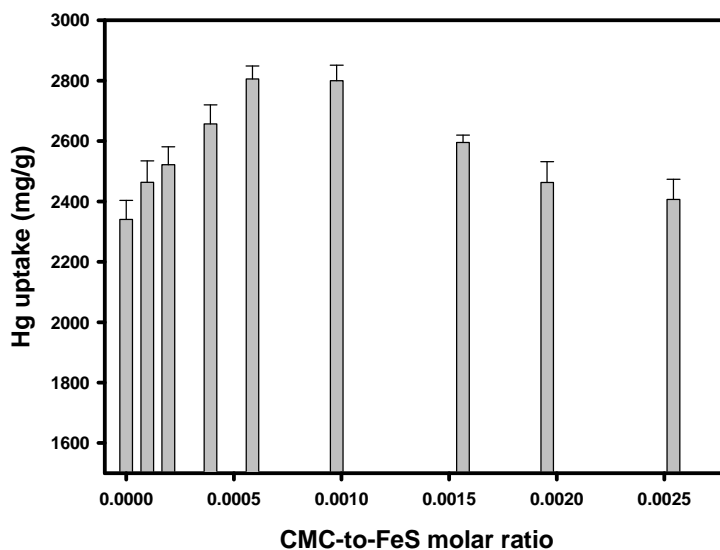


Figure 2-7. Mercury uptake by FeS nanoparticles prepared at various CMC-to-FeS molar ratios. Initial $\text{Hg}^{2+} = 40 \text{ mg/L}$, and $\text{FeS} = 12 \text{ mg/L}$. In all cases, pH was kept at 7.0, and ionic strength was 0.1 M. Data plotted as mean of duplicates and error bars (calculated as standard error) indicate data reproducibility.

2.3.4 Mercury sorption kinetics, isotherm, and mechanisms

Kinetic tests were carried out to determine the sorption rate of mercury by CMC-FeS. **Figure 2-8a** shows the Hg^{2+} removal kinetic data by CMC-FeS. The sorption displayed a rapid initial (< 0.5 h) rate and then slowed down till equilibrium at ~6.7 h, which is consistent with the common notion that more accessible sites are occupied first (Axe and Anderson, 1995). At equilibrium, ~86% mercury was removed from the solution.

The commonly used pseudo-first-order and pseudo-second-order models were applied to simulate the kinetic data (**Figure 2-8b** and **2-8c**). **Table 2-1** summarizes the models, fitting parameters, and the coefficient of determination (R^2) values. The pseudo-second-order kinetic model provided better fitting ($R^2=0.998$) compared to the pseudo-first-order model ($R^2=0.968$), which is consistent with the findings by Ghodbane and Hamdaoui (2008), who modeled the

mercury sorption kinetics by eucalyptus bark. The results suggest that the rate limiting step appeared to be the sorption process rather than diffusion (Ho and McKay, 1999).

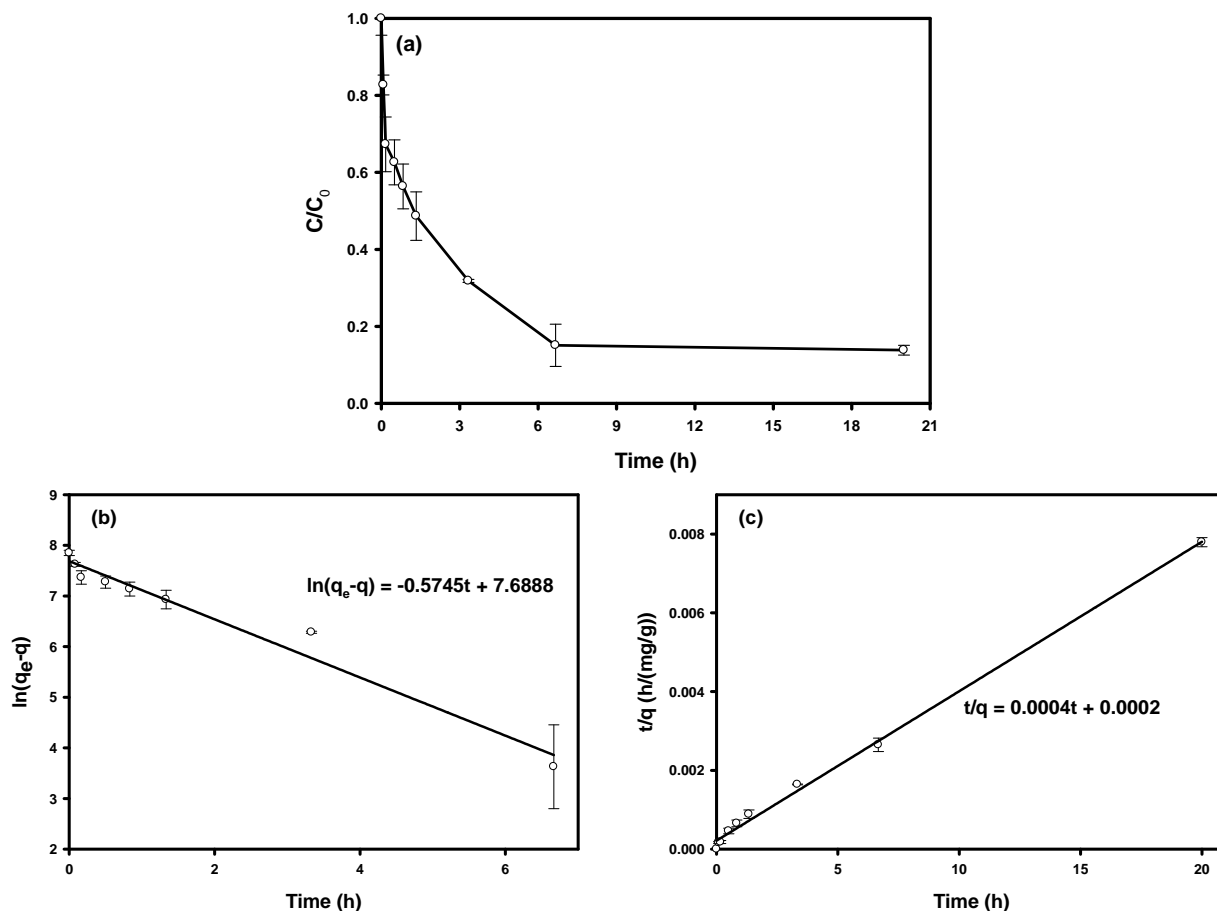


Figure 2-8. (a) Mercury sorption kinetics by CMC-FeS, and (b) pseudo-first-order and (c) pseudo-second-order kinetic fittings of mercury sorption by CMC-FeS. Initial $\text{Hg}^{2+} = 40$ mg/L, FeS = 12 mg/L, CMC-to-FeS molar ratio = 0.0010, pH = 7.0, and ionic strength = 0.1 M. Data plotted as mean of duplicates and the error bars (calculated as standard error) indicate data reproducibility.

Table 2-1. Pseudo-first-order and pseudo-second-order models used for simulating mercury sorption kinetic data and the resulting fitting parameters (Errors given as standard error).

Kinetic models	Governing equation	Plot Equation	Parameters			R ²
Pseudo-first-order	$\frac{dq}{dt} = K_1(q_e - q)$	$\ln(q_e - q) = \ln q_e - K_1 t$	K_1 (h ⁻¹)	q_e (mg/g)	$h_1 = K_1 q_e$ (mg/(g·h))	0.968
			0.57±0.04	2198.41±253.44	1253.09	
Pseudo-second-order	$\frac{dq}{dt} = K_2(q_e - q)^2$	$\frac{t}{q} = \frac{1}{K_2 q_e^2} + \frac{1}{q_e} t$	K_2 (g/(mg·h))	q_e (mg/g)	$h_2 = K_2 q_e^2$ (mg/(g·h))	0.998
			(8.67±2.41)×10 ⁻⁴	2507.95±48.68	5453.27	

Note: q (mg/g): uptake of Hg²⁺ by CMC-FeS nanoparticles at time t (h); q_e (mg/g): uptake of Hg²⁺ at equilibrium; K_1 (h⁻¹): rate constant of the pseudo-first-order sorption; K_2 (g/(mg·h)): pseudo-second-order sorption rate constant; h_1 (mg/(g·h)): the initial rate of the pseudo-first-order sorption; h_2 (mg/(g·h)): the initial rate of the pseudo-second-order sorption. The governing equations of the two models are integrated by applying the boundary conditions $q = 0$ at $t = 0$ (Ghodbane and Hamdaoui, 2008). R²: the coefficient of determination, which is calculated per the equation $R^2 = 1 - \frac{\sum_i (y_i - y_{i(predict)})^2}{\sum_i (y_i - \bar{y})^2}$, where y_i and $y_{i(predict)}$ are the original data values and model values, respectively, and \bar{y} is the mean of the observed data.

Figure 2-9 presents mercury sorption isotherm for CMC-FeS at a fixed pH of 7.0. The classical Langmuir model and Freundlich model were first used to fit the isotherm data, and fitting results are given in **Table 2-2**. However, to be more mechanistically sound, and in light of the aforementioned mercury sorption mechanisms, we propose a dual-mode isotherm model that incorporates surface adsorption and precipitation:

$$q_e = K_d C_e + \frac{bQ C_e}{1 + bC_e} \quad (\text{Eq. 2.9})$$

where q_e represents the total mercury uptake (mg/g), C_e is the equilibrium concentration of mercury in the solution phase (mg/L), K_d is the linear distribution coefficient (L/mg) associated with surface precipitation, b is the Langmuir affinity constant (L/mg), and Q is the Langmuir maximum sorption capacity (mg/g). Mechanistically, the first term represents HgS precipitation, which is considered linearly related to C_e , whereas the second term corresponds to adsorption or surface complexation. The same formula was used for sorption of hydrophobic organic compounds to rubbery and glassy domains of polymeric sorbents (Xing and Pignatello, 1997; Zhao et al., 2001).

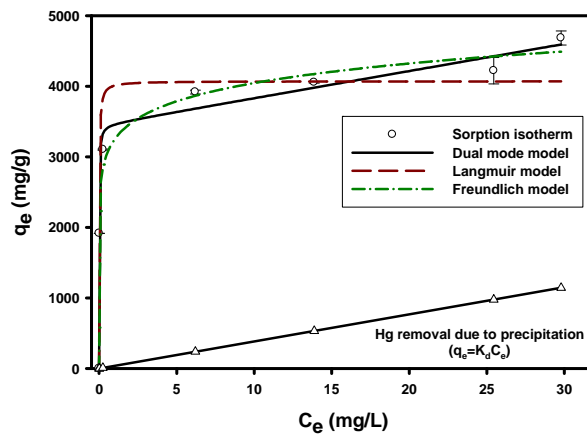


Figure 2-9. Mercury sorption isotherm of CMC-FeS nanoparticles. FeS = 2.5 mg/L, CMC-to-FeS molar ratio = 0.0010, Initial Hg^{2+} = 4.8-40 mg/L, pH = 7.0, and ionic strength = 0.1 M.

Symbols: experimental data; Lines: model fittings. Data plotted as mean of duplicates and the error bars (calculated as standard error) indicate data reproducibility.

Table 2-2. Best-fitted parameters for Langmuir, Freundlich and dual-mode sorption isotherm models (Errors given as standard error).

Adsorption isotherm	Parameters			R ²
Langmuir	Q (mg/g)	b (L/mg)		0.940
	4070.92±205.10	81.85±37.20		
Freundlich	K _f , (mg/g)/(mg/L) ⁿ	n		0.987
	3246.27±101.91	0.096±0.011		
Dual-mode	Q (mg/g)	b (L/mg)	K _d (L/mg)	0.990
	3449.23±163.65	111.07±29.77	(38.38±8.48)×10 ⁻³	

Note: R² is calculated in the same manner as noted in Table 2-1.

Table 2-2 gives the best-fitted model parameters and the R² values. Evidently, the Freundlich model (R²=0.987) outperformed the Langmuir model (R²=0.940), and the dual-mode model gave the best goodness of fitting (R²=0.990).

Figure 2-9 also shows the relative contributions of the two removal mechanisms, indicating that precipitation becomes more important at elevated Hg concentrations. At a Hg-to-FeS molar ratio of 0.84 (C_e = 0.012 mg/L), nearly 100% removal was attributed to adsorption. As Hg loading increases, the adsorption capacity of CMC-FeS becomes saturated, giving rise to the chemical precipitation. For instance, as the molar ratio increased to 4.2 (C_e = 14 mg/L), 13% of Hg removal was due to precipitation and 87% to adsorption, and at C_e = 28 mg/L, 25% of Hg removal was due to precipitation. These findings second the observations by Jeong et al. (2007) who studied mercury removal by synthesized nanocrystalline mackinawite aggregates and

concluded that at $\text{Hg-to-FeS} < 0.05$, adsorption was mainly responsible for Hg removal based on the availability of reactive surface sites.

Based on the capacity data, CMC-FeS offers much greater Hg sorption capacity ($Q = 3449$ mg/g) than other FeS particles or materials reported. For example, Liu et al. (2008) synthesized and tested a class of non-stabilized FeS particles (with a specific surface area of $7.8 \text{ m}^2/\text{g}$), and observed a q_e of 1700 mg/g corresponding to a C_e of 11.9 mg/L with the addition of 0.4 g/L of FeS to 700 mg/L Hg^{2+} solution at an initial pH 5.6. Wang et al. (2009) reported a Q of 600 mg/g at pH 5.5 for a polyaniline-based sorbent, and Ghodbane and Hamdaoui (2008) obtained a Q of 33.11 mg/g at pH 5 using eucalyptus bark.

Figure 2-10 presents XRD spectra of bare FeS and CMC-FeS particles upon equilibration with Hg^{2+} . The three highest peaks appeared at 2θ values of 26.5° , 43.8° and 51.7° , consistent with the characteristic peaks of metacinnabar HgS (ICDD, 06-0261), cinnabar HgS (ICDD, 06-0256), and $(\text{Hg}_{0.89}\text{Fe}_{0.11})\text{S}$ (ICDD, 50-1151). Similar findings were reported by Liu et al. (2008), who studied Hg^{2+} removal with synthesized mackinawite aggregates and found the formation of mercuric sulfides, including mercury-iron sulfide. The XRD results support the rationale of the dual mode sorption model, i.e., CMC-FeS takes up Hg^{2+} through concurrent chemical precipitation (formation of metacinnabar and cinnabar) (**Eqs. 2.1-2.3**) and adsorption (**Eqs. 2.4-2.5**).

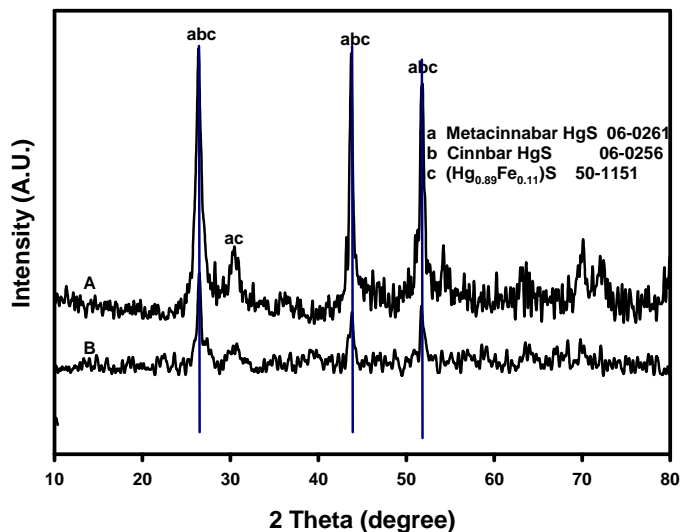


Figure 2-10. XRD spectra of **A:** Hg^{2+} -laden CMC-FeS nanoparticles, and **B:** Hg^{2+} -laden bare FeS aggregates. Notations: “a” for metacinnabar, “b” for cinnabar, and “c” for $(\text{Hg}_{0.89}\text{Fe}_{0.11})\text{S}$. XRD powders were prepared in the conditions: FeS = 12 mg/L, initial Hg^{2+} = 40 mg/L, pH = 7.0, and ionic strength = 0.1 M.

2.3.5 Effects of pH

Figure 2-11 shows effects of pH on mercury removal by CMC-FeS. The mercury uptake rose sharply from 2450 to 2800 mg/g as equilibrium pH increased from 6.0 to 6.5, and then remained at a plateau of 2800 mg/g from pH 6.5 to pH 10.5. The much lower uptake at pH 6.0 is attributed to partial dissolution of FeS nanoparticles and thus partial loss of the binding sites (ion exchange and surface complexation). This observation indicates that although the precipitation mechanism is favored at acidic pH, the loss in the adsorption capacity outweighs the gain in the formation of $\text{HgS}(\text{s})$. **Figure 2-12a** shows the particle dissolution (measured as soluble Fe^{2+}) over a pH range of 3-12. While the nanoparticles were stable at $\text{pH} \geq 7$, 32% of Fe was dissolved at pH 6. The observation is consistent with the speciation profiles of FeS simulated per MINTEQ (**Figure 2-12b**).

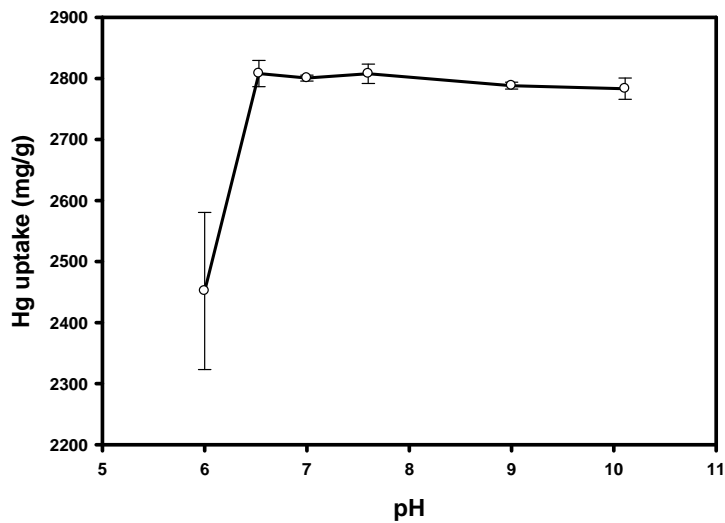


Figure 2-11. Mercury uptake by CMC-FeS as a function of equilibrium pH. CMC-to-FeS molar ratio = 0.0010, FeS = 12 mg/L, Initial Hg^{2+} = 40 mg/L, and ionic strength = 0.1 M. Data are plotted as mean of duplicates, with error bars (calculated as standard error) showing data reproducibility.

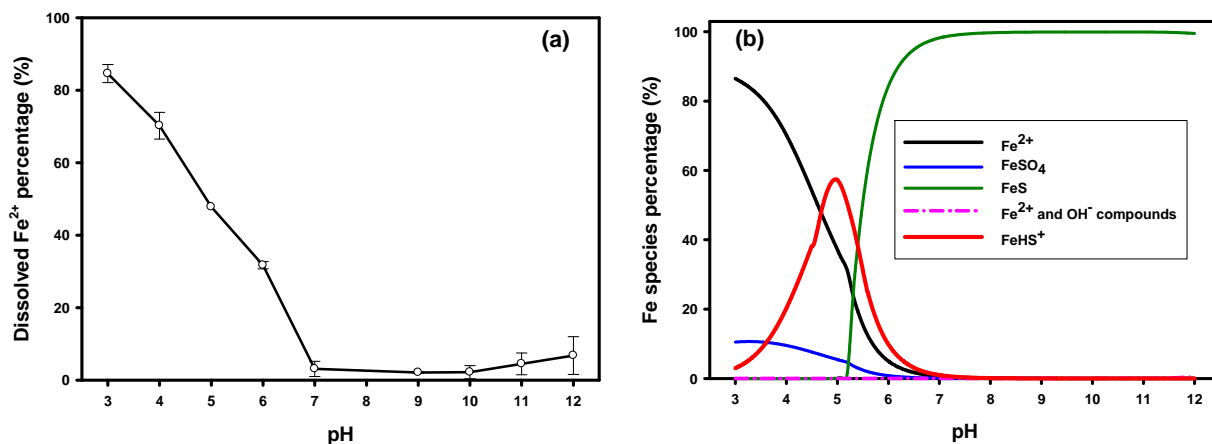


Figure 2-12. (a) Dissolution of CMC-FeS measured as soluble Fe as a function of final pH, and (b) Fe speciation (without CMC) simulated using Visual MINTEQ (version 2.61). FeS = 100 mg/L, CMC-to-FeS molar ratio = 0.0010. Data are plotted as mean of duplicates, with error bars (calculated as standard error) showing data reproducibility.

The pH of the point of zero charge for CMC-FeS was <2.5 (Gong et al. 2012). Therefore, the surface of the nanoparticles is negatively charged at pH≥6.5. Over the pH range of 6.5-10.5, Hg(OH)₂ (aq) and FeS are the predominant species, i.e., mercury was taken up by FeS in the form of the hydrolyzed species. This agrees with the observation of Jean and Bancroft (1986) who studied sorption of Hg²⁺ by pyrite and pyrrhotite and asserted that Hg(OH)₂ was adsorbed directly on the sulfur groups up to approximately monolayer coverage in the pH range of 7.0-11.0.

2.3.6 Effect of chloride

Chloride has been known to hinder Hg²⁺ sorption by sulfide minerals (Behra et al., 2001; Hyland et al., 1990; Jean et al., 1986). **Figure 2-13a** shows equilibrium mercury uptake by CMC-FeS in the presence of various Cl⁻ concentrations. At Cl⁻≤106 mg/L (typical in natural fresh waters), the effect was negligible; however, increasing Cl⁻ from 106 to 1775 mg/L lowered Hg²⁺ uptake by 14% (from 2800 to 2400 mg/g). At the Cl⁻>1775 mg/L, Hg²⁺ uptake remained at 2400 mg/g.

In the solution phase, Cl⁻ ions compete with OH⁻ ions to form Hg-Cl complexes, which have lower affinity to CMC-FeS than Hg-OH complexes. The stepwise complexation between Hg²⁺ and Cl⁻ can be described as follows (Snoeyink and Jenkins, 1980):



Figure 2-13b gives calculated mercury speciation as a function of Cl⁻ concentration. At Cl⁻≤106 mg/L, Hg(OH)₂ and HgOHCl are the predominant species. At elevated Cl⁻ concentrations, the

less favorable mercury species $\text{HgCl}_2(\text{aq})$, HgCl_3^- , and HgCl_4^{2-} become the predominant species, resulting in the observed diminished mercury uptake. The complexation capacity became exhausted at $\text{Cl}^- > 1775 \text{ mg/L}$, and thus, no further inhibitive effect was observed.

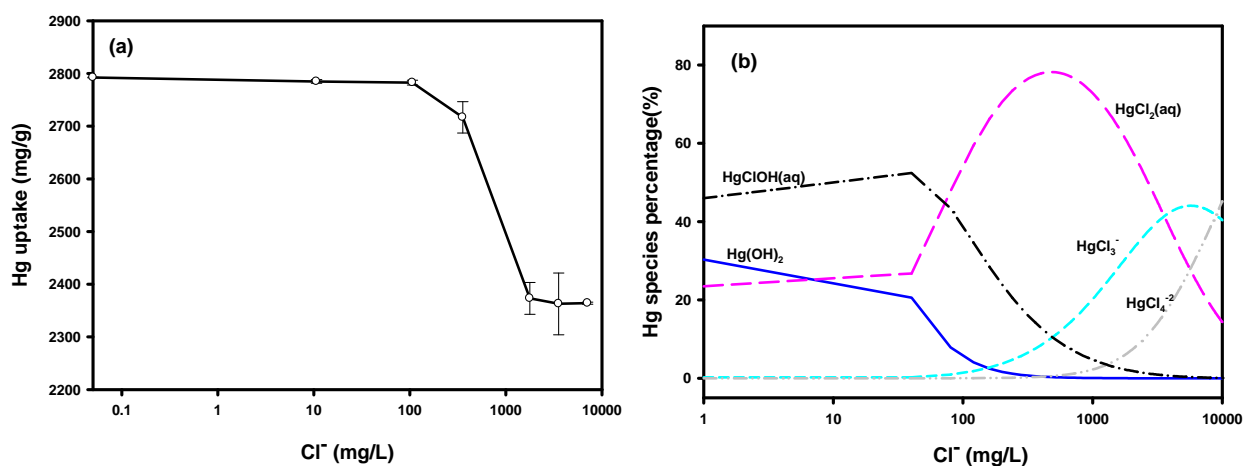


Figure 2-13. (a) Effects of chloride on mercury removal by CMC-FeS. CMC-to-FeS molar ratio = 0.0010, FeS = 12 mg/L, Initial Hg^{2+} = 40 mg/L, pH = 7.0, and ionic strength 0.1 M. Data are plotted as mean of duplicates, and the error bars indicate standard error from the mean. (b) Mercury speciation as a function of Cl^- concentrations simulated using Visual MINTEQ (version 2.61). Hg^{2+} = 40 mg/L, pH = 7.0, and ionic strength = 0.1 M.

2.3.7 Effect of DOM

Figure 2-14 shows the effects of soil-extracted DOM and a standard HA on Hg^{2+} removal by CMC-FeS. The presence of 5.5 mg/L HA (as TOC) reduced Hg^{2+} uptake by 12% (from 2800 to 2475 mg/g). However, further increasing HA from 5.5 to 28 mg/L did not show any further inhibition. The presence of 7-10 mg/L DOM (as TOC) reduced the Hg^{2+} uptake from 2800 to

2258 mg/g. Further increasing DOM to 20 mg/L reduced the uptake to 1800 mg/g. Skyllberg and Drott (2010) reported similar inhibitive effects on Hg^{2+} uptake by synthetic mackinawite.

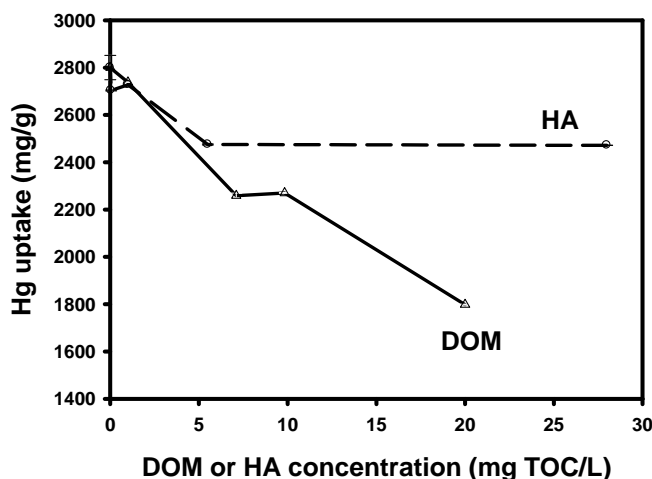


Figure 2-14. Effects of DOM and HA on mercury uptake by CMC-FeS. FeS = 12 mg/L, CMC-to-FeS molar ratio = 0.0010, Initial Hg^{2+} = 40 mg/L, pH = 7.0, and ionic strength 0.1 M. Data are plotted as mean of duplicates and the error bars (calculated as standard error) indicate data reproducibility.

DOM can inhibit the Hg^{2+} uptake in several ways. First, DOM can serve as competitive ligands to complex with mercury, which can compete with FeS for the aqueous mercury. For example, Hg^{2+} can form two-coordinate complexes with thiol groups (RSH) (Skyllberg et al., 2006). Skyllberg and Drott (2010) observed competitive complexation between Hg^{2+} and organic thiols [$\text{Hg}(\text{SR})_2$] and with inorganic sulfides. Second, DOM can compete with CMC molecules, altering the stabilizing effectiveness of CMC, the ζ potential, and thus, aggregation of the nanoparticles. Based on DLS measurements, the mean particles size in the presence of 20 mg/L of extracted DOM increased from 222 nm (without DOM) to 295 nm, and the ζ potential from -

55.6 to -39.2 mV. Competitive uptake of DOM, especially low-molecular weight DOM molecules, would diminish accessibility of available sorption sites on the nanoparticles both thermodynamically and kinetically (Zhang et al., 2011). Interestingly, the presence of 28 mg/L of HA reduced the DLS-based hydrodynamic size from 222 nm to 146 nm. Noting that the DLS-based size includes both the core FeS and the organic coatings, and the molecular weight of HA used in this study (226) is nearly 400 times smaller than that of CMC (90 k), the reduced DLS size indicates substantial replacement of CMC by HA on the particle surface. The molecular weight of natural HA can range from <700 to >200,000 (Ishiwatari, 1971). The HA effect observed in this work may represent a worst-case scenario as larger HA molecules behave more like the CMC molecules. Further details are to yet be investigated in this regard. **Figure 2-14** also suggests that the nanoparticles are easily saturated by HA (at 5.5 mg/L). As a result, no further inhibitive effect was evident at higher HA concentrations.

2.3.8 Effects of ionic strength

Figure 2-15 shows that ionic strength in the range of 0.02-0.2 M exerted negligible effect on mercury uptake by CMC-FeS. While Wang et al. (2009) reported similar observation on Hg²⁺ sorption by polyaniline, others reported inhibitive effect at elevated ion strength. For instance, Ghodbane and Hamdaoui (2008) reported that the presence of 10 g/L Na₂SO₄ decreased Hg uptake by eucalyptus bark by 51% due to the competitive effect of Na⁺.

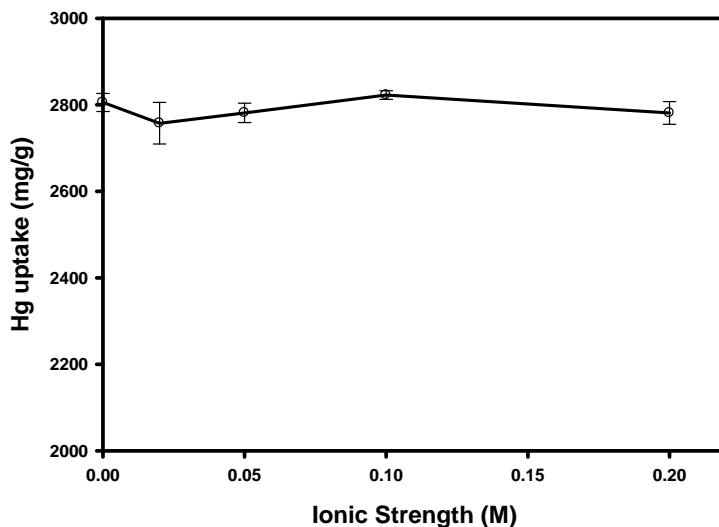


Figure 2-15. Effects of ionic strength on mercury uptake by CMC-FeS. FeS = 12 mg/L, CMC-to-FeS molar ratio = 0.0010), Initial Hg^{2+} = 40 mg/L, and pH = 7.0. Data are plotted as mean of duplicates and the error bars (calculated as standard error) indicate data reproducibility.

2.3.9 Aging effect and long-term stability

For engineered remediation uses, it is desirable that both material integrity of the nanoparticles and stability of immobilized mercury are maintained over prolonged periods of time. **Figure 2-16** shows effects of aging time (i.e., reaction time between Hg^{2+} and CMC-FeS) on mercury sorption. The sorption capacity dropped by 4% from 2800 to 2682 mg/g after 60 d, 9.2 % after 100 d, and 14% after 912 days of aging at room temperature and an initial pH of 7.0. The partial loss in the sorption capacity was associated with the gradual pH drop to 6.2 after 912 d, which in turn dissolves part of the nanoparticles (**Figure 2-12a**). When the pH of the samples after 912 d was adjusted to 6.8, the sorption capacity rebounded to 2585 mg/g. The observation confirms that at pH above neutral, the nanoparticles are likely to facilitate long-term immobilization of mercury.

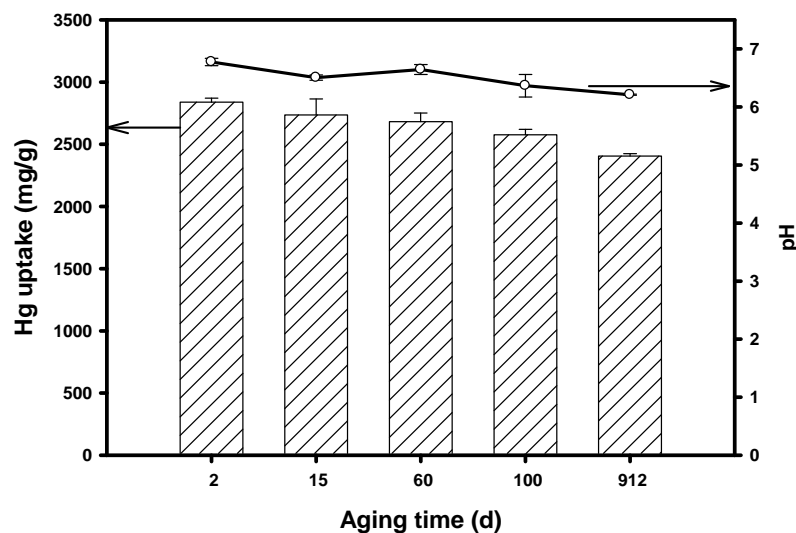


Figure 2-16. Mercury uptake by CMC-FeS and evolution of suspension pH as a function of aging. FeS = 12 mg/L, CMC-to-FeS molar ratio = 0.0010, Initial Hg^{2+} = 40 mg/L, and ionic strength = 0.1 M. Data are plotted as mean of duplicates and the error bars (calculated as standard error) indicate data reproducibility.

2.4 Conclusions

This study demonstrates potential and viability of CMC-stabilized FeS nanoparticles for enhanced immobilization of mercury from contaminated water or groundwater. The primary findings are summarized as follows:

- 1) CMC was confirmed to be a highly effective stabilizer for preparing highly dispersible FeS nanoparticles. The critical CMC-to-FeS molar ratio for complete particle stabilization was determined to be 0.0006. The DLS-based particle size remained nearly the same at CMC concentrations above the CSC value.
- 2) FTIR analysis revealed that CMC molecules were attached to the surface of FeS nanoparticles through bidentate bridging and hydrogen bonding. An examination of FTIR

spectra of Hg-free and Hg-laden FeS indicates that surface complexation between CMC-FeS and Hg^{2+} is an important mechanism for Hg immobilization. On the other hand, XRD analysis showed that cinnabar, metacinnabar, and $\text{Hg}_{0.89}\text{Fe}_{0.11}\text{S}$ were formed during the sorption process, indicating that precipitation is concurrently operative. However, the relative contributions of surface complexation (adsorption) and precipitation were found to vary according to the Hg-to-FeS molar ratio.

- 3) The particle stabilization technique increased mercury sorption capacity by 20% as the CMC-to-FeS molar ratio increased from 0 to 0.0010. However, further increasing CMC-to-FeS ratio from 0.0010 to 0.0025 diminished mercury sorption capacity by 14%.
- 4) Sorption kinetic tests indicated a fairly rapid Hg sorption rate of CMC-FeS, with an equilibrium time within 6.7 h. A pseudo-second-order kinetic model was able to adequately interpret the rate data.
- 5) We proposed a dual-mode isotherm model to simulate the Hg sorption isotherm, which considers both precipitation and surface adsorption mechanisms. Compared to the classical Langmuir or Freundlich models, the proposed model not only provides improved goodness of fitting, but offers a mechanistically sounder physical basis.
- 6) High mercury uptake was observed over the pH range of 6.5-10.5. Acidic pH should be avoided due to partial dissolution of the nanoparticles. Effect of chloride at <106 mg/L on Hg^{2+} sorption was negligible, while Hg^{2+} uptake decreased by 14% when chloride increased from 106 to 1775 mg/L. However, no further inhibitive effect was observed at higher Cl^- mg/L, suggesting the nanoparticles hold the potential for brine treatment. High concentrations of DOM may inhibit mercury immobilization, whereas effect of ionic strength (0-0.2 M) was negligible.

7) The CMC-FeS nanoparticles and immobilized Hg thereon remained stable when preserved for 2.5 years under anoxic conditions and room temperature. However, acidic pH should be avoided for long-term Hg immobilization.

The findings in this work indicate that CMC-stabilized FeS nanoparticles hold the promise to be employed as an effective sorbent for the immobilization of mercury in contaminated soil and groundwater.

Chapter 3. Immobilization of Mercury in Field Soil and Sediment Using Carboxymethyl Cellulose Stabilized Iron Sulfide Nanoparticles

Effective *in situ* mercury remediation technologies have been lacking. This chapter investigated effectiveness of a class of soil-deliverable sodium carboxymethyl cellulose (CMC) stabilized iron sulfide (FeS) nanoparticles for *in situ* immobilization of Hg in high-profile mercury-contaminated field soil/sediment through a series of batch and column experiments. TCLP (Toxicity Characteristic Leaching Procedure) based on mercury leachability after the treatments was measured to validate the performance of the nanoparticles. The transport behaviors of the nanoparticles in the soil/sediment were also described.

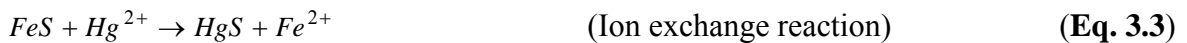
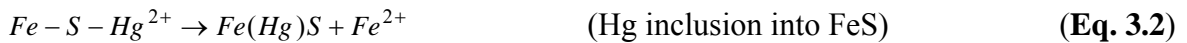
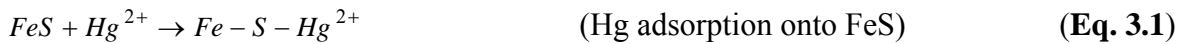
3.1 Introduction

Mercury (Hg) is one of the most pervasive and bio-accumulative toxins. The primary anthropogenic sources of Hg include mining activities, oil and coal combustion, waste incineration, crematoria, chlor-alkali industries, municipal wastes, and sewage sludge combustion (Bower et al., 2008; Fitzgerald et al., 1998; Hogue, 2007).

Depending on environmental conditions, Hg can be present in three valence states (+I, +II and 0), and can be transformed both biotically and abiotically to methylmercury (Zhang and Planas, 1994). Methylmercury has been the primary environmental concern because of its ability to bio-accumulate in organisms along the food chains, where concentrations could apex one million times greater than in the water column (Stein et al., 1996; UNEP, 2007).

In the subsurface, non-aqueous phase Hg could serve as a long-term contaminant source to groundwater and surface water (Bower et al., 2008). Traditionally, remediation of Hg-containing soils or sediments employs excavation and thermal treatments such as incineration, retorting and roasting (Piao and Bishop, 2006). However, these technologies bear with some serious drawbacks, such as high cost, potential hazards to workers, emission of element Hg, and disruption of the environment. Consequently, innovative *in situ* remediation technologies to immobilizing Hg in soils or sediments are urgently needed.

Hg(II) is a soft Lewis acid and shows a distinct tendency to form strong bonds with soft Lewis bases such as sulfur. Formation of HgS in sulfidic soils and sediments has been considered one of the primary sinks for Hg in the environment (Zhang and Planas, 1994). Natural sulfide minerals such as pyrite (FeS₂), pyrrhotite (Fe_{1-x}S_x), and mackinawite (FeS) are known to be excellent adsorbents for Hg (Brown et al., 1979). Iron sulfide (FeS), which represents a major constituent of acid-volatile sulfides, is generally thought to have a high sorption capacity for Hg²⁺. The possible reactions include adsorption, structural incorporation and precipitation as a discrete phase of HgS (Jeong et al., 2007; Morse and Luther, 1999; Svensson et al., 2006; Wolfenden et al., 2005), as depicted below:



HgS(s) is extremely stable ($K_{sp} = 2 \times 10^{-53}$) in the environment (Barnett et al., 2001). Formation of metacinnabar (black) and mercury-iron sulfide were detected by X-ray diffraction (XRD) when Hg was reacted with non-stabilized FeS (bare FeS) aggregates (Jeong et al., 2007; Liu et al., 2008). Spectroscopic studies revealed that Hg can strongly complex with reduced

sulfur groups in soil/sediment organic matter (SOM), and the high affinity of Hg for S prevails even in highly oxic environments (Wolfenden et al., 2005; Skyllberg et al., 2006).

Numerous recent studies have been reported on the development of various nanoparticles for sorption of elemental Hg and mercuric ion in water (Borderieux et al., 2004; Jeong et al., 2007; Liu et al., 2008; Meyer et al., 2007; Pacheco et al., 2006; Pitoniak et al., 2005; Sumesh et al., 2011; Yantasee et al., 2007). For example, iron oxide (Fe_2O_3) nanoparticles (Borderieux et al., 2004), titania doped silica nanocomposites (Pitoniak et al., 2005), and copper doped iron nanoparticles modified with organic sulfur (Meyer et al., 2007) were reported for successful capture of elemental mercury vapor (Hg^0) for potential coal-fired power plants applications. Mackinawite nanoparticles (Jeong et al., 2007; Liu et al., 2008;), alumina nanoparticles (Pacheco et al., 2006), silver nanoparticles supported on activated alumina (Sumesh et al., 2011), and magnetite (Fe_3O_4) nanoparticles functionalized with dimercaptosuccinic acid (Yantasee et al., 2007) were developed and proved to be effective sorbent materials for Hg^{2+} in aqueous systems.

In recent years, *in situ* immobilization of trace metals in the subsurface by delivering reactive nanoparticles into the contaminated source zones has been considered a promising alternative (Liu and Zhao, 2007; Pan et al., 2010; Xiong et al., 2009). In a prior work, Xiong et al (2009) proposed a strategy for preparing soil-deliverable FeS nanoparticles using carboxymethyl cellulose (CMC) as a stabilizer and observed that the CMC-stabilized FeS (CMC-FeS) nanoparticles can effectively immobilize Hg^{2+} spiked in a marine sediment. They proposed an *in situ* Hg immobilization remediation technology by delivering CMC-FeS nanoparticles into contaminated soils or sediments. Compared to bare FeS aggregates, the stabilized nanoparticles offer some unique advantages, including 1) the nanoparticles are deliverable in soils or sediments, 2) they offer higher sorption capacity and affinity toward Hg^{2+} , 3) the materials are low-cost and

environmentally friendly. However, the effectiveness of CMC-FeS nanoparticles for treating field-contaminated soils or sediments has not been investigated.

The overall goal of this study was to investigate effectiveness of the CMC-FeS nanoparticles for immobilization of Hg in some of the high-profile Hg-contaminated field soils and sediments. The specific objectives were to: 1) modify the particle preparation recipe by understanding long-term nanoparticle stability and interactions between CMC and FeS; 2) investigate the effectiveness of the nanoparticles for immobilization (defined as reduction in solubility and leachability) of Hg in three high-profile, paradigm field soils and sediments; and 3) determine transport behavior of the nanoparticles in the model soils and sediment.

3.2 Materials and methods

3.2.1 Materials

Three field soil and sediment samples were collected from two national-caliber Hg-impacted sites. One sediment (designated as AL1) was collected from an Alabama site that is designated as both a Resource Conservation and Recovery Act (RCRA) facility and a National Priority List (NPL) site. Hg contamination of soil and groundwater at the site has been the primary problem and various cleanup efforts have been ongoing for more than a decade. Two soil samples (denoted as NJ4 and NJ38) were collected from a New Jersey site which is associated with several NPL sites. Elevated concentrations of Hg were historically detected at this site and have been related to ongoing remediation efforts (excavation, waste incineration and smelting) at the NPL sites as well as surface water runoff. The samples were preserved in sealed buckets and stored at 4°C in the refrigerator. Before use, the samples were air-dried and sieved through a 2-mm screen.

All chemicals used in this study were of analytical or higher grade. Iron sulfate heptahydrate ($\text{FeSO}_4 \cdot 7\text{H}_2\text{O}$) and CMC (M.W. = 90,000 in sodium form) were purchased from Acros Organics (Morris Plains, NJ, USA). All other chemicals were obtained from Fisher Scientific (Fair lawn, NJ, USA).

3.2.2 Soil and sediment analysis

Soil and sediment analysis was performed by the Soil Testing Laboratory at Auburn University. The total carbon, nitrogen and sulfur contents were determined using an Elementar Vario Macro CNS analyzer (Elementar, Hanau, Germany) at 140 °F following the combustion method (Kirsten, 1979). The soil texture was analyzed following the hydrometer method (Bouyoucos, 1962). The metal contents were measured with an Inductively Coupled Plasma Atomic Emission Spectrometry (ICP-AES, Varian Vista-MPX Axial Spectrometer, Varian, Walnut Creek, CA, USA) per EPA method 3050B. Soil calcium, magnesium, potassium and sodium were first extracted per the Mehlich 1 procedure, filtered through a #1 qualitative filter paper and then determined by a Varian Vista-MPX Radial Spectrometer (Varian, Walnut Creek, CA, USA). Soil/sediment pH was measured on a 1:1 soil/sediment:water mixture via the Reference Soil Test Methods for the Southern Region of the United States: Southern Cooperative Series Bulletin 289. Hydraulic conductivity was determined following the constant head method (He et al., 2009). **Table 3-1** gives salient properties of the sediment and soils. In general, the soil/sediment texture conformed to the class of sandy clay loam. The SOM content ranged from 1.0% to 5.5%, and the sulfur content from 0.032% to 0.062%.

Air-dried soil and sediment samples were digested per U.S. EPA method 3050B and analyzed for Hg using a Cold Vapor Atomic Adsorption Spectroscopy (CVAA) following U.S. EPA method 1631E. The Hg content for NJ4 and NJ38 was 400.52 ± 1.01 mg/kg and 193.04 ± 9.08

mg/kg, respectively. The sediment AL1 has a relatively low content of Hg (21.96 ± 1.97 mg/kg). To facilitate the subsequent Hg treatment experiments, this sediment sample was pre-spiked with Hg(II) to obtain a higher Hg content. The procedure by Xiong et al (2009) was modified to prepare the Hg-spiked sediment. First, 475 g of air-dried sediments were mixed with 0.185 g $\text{Hg}(\text{NO}_3)_2 \cdot \text{H}_2\text{O}$ and 25 mL of DI water in a sealed 1 L Teflon container. The mixture was rotated on an end-to-end tumbler continuously for 30 days. Then, 900 mL of DI water was added to the sediments and the mixture was rotated for 15 days, which was sufficient to reach equilibrium (confirmed by intermittent analysis of Hg concentration in the aqueous phase). The difference between the initial and final concentrations of Hg in the aqueous phase gave the amount of Hg adsorbed by the sediment. Upon centrifuging, the sediment samples were air-dried and homogenized by mixing. The final total Hg content in the sediment was confirmed via EPA method 3050B to be 247.67 ± 20.60 mg/kg. Therefore, Hg in NJ4 and NJ38 represents historically aged field Hg, while Hg in AL1 exemplifies Hg in freshly contaminated sites.

Table 3-1. Salient physical and chemical properties of soil and sediment samples

Sample	Sand	Silt	Clay	SOM	pH	Cation Exchange Capacity	Hydraulic conductivity	C	N	S	Ca	K	Mg	Al	Fe	Mn	Na	Zn
	(%)	(%)	(%)	(%)		(meq/100g)	(cm/s)	(%)	(%)	(%)				mg/kg				
AL1	80.0	0.0	20.0	1.0	7.51	4.6	0.0004	0.61	0.04	0.034	557	45	134	148	5170	28	134	2
NJ4	46.7	20.0	33.3	5.5	7.07	16.8	0.000111	3.19	0.22	0.062	2608	288	327	269	18644	65	78	14
NJ38	61.7	11.7	26.7	4.1	7.56	28.8	0.000164	2.37	0.12	0.032	5061	64	353	139	29243	45	82	23

3.2.3 Preparation of CMC-FeS nanoparticles

CMC-FeS nanoparticles were prepared following the method by Xiong et al (2009). In each batch, a 150 mL suspension of CMC-FeS was prepared in a 250 mL flask attached to a vacuum line. First, a CMC stock solution (1%, w/w) was prepared with DI water. Then, 7.5 mL of the stock solution was added into 112.5 mL DI water and the mixture purged with purified N₂ (>99%) for 15 minutes to remove dissolved oxygen (DO). Meanwhile, solutions of 0.043 M FeSO₄ (20 mL) and 0.085 M Na₂S (20 mL) were prepared with N₂-purged DI water right before use. Under N₂ purging, the FeSO₄ solution (20 mL) was added to the CMC solution to yield a solution with a 0.006 M of Fe²⁺ and 0.054% of CMC. The mixture was then purged with N₂ for 5 minutes to assure complete mixing and formation of Fe²⁺-CMC complexes. Then, the Na₂S solution (10 mL) was introduced into the solution dropwise under shaking at 150 rpm and vacuum through a burette at an Fe-to-S molar ratio of 1:1. To ensure complete reaction, the system was shaken for another 5 minutes. The resultant nanoparticle suspension contained 0.05% of CMC and 500 mg/L FeS. For comparison, bare FeS were also prepared following the same procedure but without CMC. The particles were then sealed and aged for 24 hours before use.

3.2.4 Characterization of CMC-FeS nanoparticles

The UV-vis absorption spectra were obtained using a Hewlett Packard 8453 UV-Visible spectrophotometer in the wavelength range of 200 to 900 nm.

The mean hydrodynamic diameter and zeta potential (ζ) of the nanoparticles were determined by dynamic light scattering (DLS) tests, which were performed with a Malvern Zetasizer Nano ZS (Malvern Instruments, Worcestershire, UK). Suspension viscosity was measured with a Gilmont falling-ball viscometer (Barnant Company, Barrington, IL, USA) and used to correct for the influence of viscosity on the DLS measurements.

3.2.5 Immobilization of Hg: batch tests

Batch Hg immobilization experiments were conducted in sealed Teflon vials (28 mL) under anoxic conditions. Control tests showed that Hg adsorption on the Teflon vials was negligible. Prior to the tests, all solutions were purged with N₂ for at least 30 minutes. For sediment AL1, the tests were initiated by mixing 2.7 g of the sediment to 27 mL of a nanoparticle suspension. The nanoparticle dosage was varied at 100, 200, 500 and 1000 mg/L as FeS (or an FeS-to-Hg molar ratio of 9:1, 18:1, 46:1, 92:1), respectively. For soil NJ38, 1.35 g of a soil sample was treated with 27 mL of the nanoparticles at concentrations of 500 and 1000 mg/L, respectively (or an FeS-to-Hg molar ratio of 118:1, 235:1). The same nanoparticle dosage was applied to soil NJ4. However, due to the different Hg contents of NJ38 and NJ4, the FeS-to-Hg molar ratio for NJ4 was lowered to 28:1 and 57:1. The mixtures were then sealed and rotated on an end-to-end rotator at 30 rpm at room temperature (20±1 °C). At predetermined time intervals, duplicate vials were sacrificially sampled, and the samples were measured for pH and centrifuged at 6000 g-force for 10 minutes to separate the solid from the aqueous phase. The supernatant was then filtered through 50 nm Millipore membrane filters (Millipore Corp., Billerica, MA, USA). The filtration was able to retain >96% of the nanoparticles as determined by analyzing total iron in the filtrate, without retaining any soluble Hg. The filtrates were preserved with BrCl (1%), which can dissolve any Hg species including HgS, for Hg analysis. Control tests were also carried out using CMC solutions of various concentrations (0, 0.01%, 0.02%, 0.05% and 0.10%). All tests were conducted in duplicate.

3.2.6 TCLP tests

TCLP (Toxicity Characteristic Leaching Procedure) tests were performed following EPA Method 1311 to determine the leachability of Hg in the untreated and nanoparticle-amended

samples. The TCLP tests were conducted by adding 1.2 g of an air-dried soil/sediment sample to 24 mL of the fluid #1 (acetic acid, initial pH = 4.93). The mixtures were rotated at 30 rpm at room temperature ($20\pm 1^\circ\text{C}$) for 18 hours and then centrifuged at 6000 g for 10 minutes. The supernatant was filtered through 50 nm membrane filters. The filtrates were then preserved with BrCl (1%), and then analyzed for Hg. All tests were conducted in duplicate.

3.2.7 Deliverability of CMC-FeS nanoparticles

For *in situ* remediation uses, the nanoparticles must be deliverable into contaminated sediments or soils. To probe the deliverability, nanoparticle breakthrough tests were carried out through a fixed-bed column packed with AL1 and NJ4, respectively. For AL1, the experimental setup included a glass column (1 cm in inner diameter and 10 cm in length; Omnifit, Cambridge, England), a PHD 2000 infusion syringe pump (Harvard Apparatus, Holliston, MA, USA), a fraction collector (Eldex Laboratories Inc., Napa, CA, USA), and Teflon tubing. First, 11 g of sediment was wet-packed in the column, yielding a porosity of 0.35 and a bulk bed volume of 6.75 mL. About 0.3 cm (height) of glass wool was placed at the bottom of the column. Then a CMC-FeS nanoparticle suspension (FeS = 500 mg/L, CMC = 0.05%, pH = 7.0) was pumped through the sediment bed in the down-flow mode and at an empty bed contact time (EBCT) of 113 minutes. Similar column tests were also carried out with NJ4. However, because of the much lower hydraulic conductivity for this soil (Table 1), an HPLC pump, which was able to exert much greater injection pressure, and a high-strength PVC (polymerized vinyl chloride) column (1.3 cm in inner diameter and 20 cm in length) were employed. First, 7 g of the soil was wet-packed in the column, yielding a porosity of 0.46 and a bulk bed volume of 6.12 mL. Then a CMC-FeS nanoparticle suspension (FeS = 500 mg/L, CMC = 0.05%, pH = 7.0) was pumped through the soil bed at an EBCT of 102 minutes. Effluent samples were then digested with 12 M

HCl (1 mL sample vs. 4 mL HCl) for 5 minutes, which was able to completely dissolve the nanoparticles, and analyzed for total iron. To acquire information on hydrodynamic behavior and dispersion characteristics of the sediment/soil, breakthrough curves for a conservative tracer (50 mg/L KBr) were also conducted in parallel. The response curves were followed by analyzing the concentration histories of Br⁻ in the effluents.

3.2.8 Immobilization of Hg: column tests

Column tests of *in situ* Hg immobilization were conducted with the same experiment setup and procedure as described in the deliverability tests. In brief, 11 g of AL1 was wet-packed in the column. Then, 95 pore volumes of the CMC-FeS nanoparticle suspension (FeS = 500 mg/L) was passed through the sediment bed at an EBCT of 113 minutes. For NJ4, 7 g of the soil was wet-packed in the column. The soil was then treated by passing 52 pore volumes of the same CMC-FeS nanoparticle suspension through the soil bed at an EBCT of 102 minutes. The effluent samples were analyzed in two different ways to distinguish between nanoparticle-bound Hg and dissolved or free Hg in the aqueous phase. First, the total Hg (both nanoparticle-bound and free Hg) was quantified by analyzing the whole samples, i.e. the collected samples were treated with BrCl (1%) and then analyzed for total Hg. Second, effluent samples were filtrated using 25 nm membrane filters to remove all CMC-FeS nanoparticles, and thus, nanoparticle bound Hg. The filtrates were then digested with 1% BrCl, and analyzed to give the concentration of dissolved Hg. For comparison, control Hg elution tests were also carried out using a 0.05% CMC solution as the influent.

3.2.9 Chemical analysis

Hg analysis was conducted by CVAA method with SnCl₂ as a reductant using a Varian SpectrAA 220FS Atomic Absorption Spectrometer (Varian, Canton, MA, USA) equipped with a

cold vapor generator. Prior to analysis, all samples were first preserved and oxidized with 1% BrCl, then 1% hydroxylamine hydrochloride was added to destroy the unreacted BrCl. All reagents for Hg analysis were prepared following U.S. EPA Method 1631E. The detection limit of total mercury was 0.5 µg/L (at a sample volume of 10 mL). Br⁻ was analyzed using a Dionex Ion Chromatography (Dionex, Sunnyvale, CA, USA) equipped with an AS14 column (detection limit was 0.5 mg/L). Iron concentration was measured using a Flame Atomic Absorption Spectrometer (Varian SpectrAA 220FS, Varian, Canton, MA, USA) (detection limit was 0.05 mg/L).

3.3 Results and discussion

3.3.1 Characterization of CMC-FeS Nanoparticles

To determine the effect of CMC on the particle stability, FeS particles were prepared at a fixed particle concentration of 318 mg/L as Fe but with a CMC-to-FeS molar ratio ranging from 0 to 0.0025. After 24 hours of standstill, the particle stability was examined by analyzing the particle concentration (measured as Fe) that remained suspended in the supernatants. The results indicated that at a CMC-to-FeS molar ratio of 0, 0.0001, and 0.0002, the percentage of particles that remained suspended was 3%, 13% and 91%, respectively. When the CMC-to-FeS molar ratio was at 0.0006 or higher, all particles were stable. Based on this observation and equilibrium Hg sorption capacity tests (Gong et al., 2014), a CMC-to-FeS molar ratio of 0.001 was chosen in the subsequent Hg immobilization tests.

The UV-vis spectra in **Figure 3-1** provide a convenient indication of the formation of CMC-FeS nanoparticles. The pK_a value of CMC is 4.3. In all case, the pH was above 5.3. Hence, the carboxylic groups of CMC were fully dissociated. For the individual homogeneous solutions of CMC, Fe²⁺, S²⁻ or complexed Fe²⁺-CMC, no absorbance was observed at a wavelength of >280

nm, and all solutions appeared transparent. Upon addition of S^{2-} into the Fe^{2+} -CMC solution, the solution color rapidly turned black, giving rise of the strong absorbance profile over a broad wavelength of 200-900 nm. The spectra of CMC-FeS were characterized with a “bimodal” profile with a peak at 346 nm and another at 646 nm. In contrast, the suspension for the bare FeS did not show any distinctive peak. Furthermore, we observed that the absorbance for the CMC-FeS obeyed the Beer-Lambert law in the wavelength 300-700 nm when the nanoparticle concentration was varied from 12 to 60 mg/L. The UV-vis spectra in sealed vials were monitored for 30 days. Neither precipitation nor conspicuous change in UV-vis absorbance was observed for the CMC-FeS, indicating that the nanoparticles are quite stable both physically and chemically.

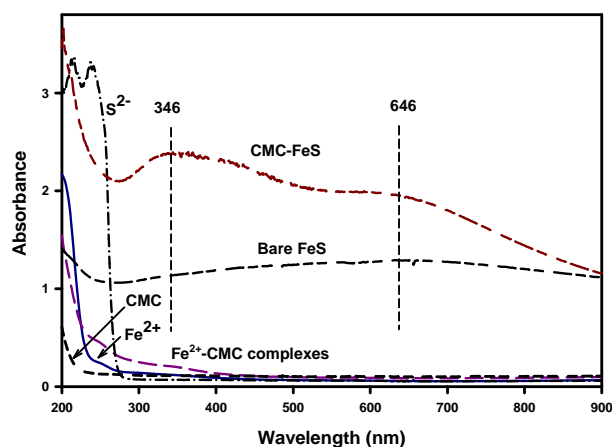


Figure 3-1. UV-vis absorption spectra of: (a) 0.05% CMC, (b) 318 mg/L Fe^{2+} , (c) Fe^{2+} -CMC complexes (0.05% CMC, 318 mg/L Fe^{2+}), (d) 182 mg/L S^{2-} , (e) 50 mg/L CMC-FeS nanoparticles, and (f) 50 mg/L bare FeS.

DLS measurements give hydrodynamic diameters of the particles with the attached stabilizer in situ. As DLS is based on particle diffusivity, the DLS-based size is relevant to particle

transport behavior. For CMC-FeS, the hydrodynamic diameter was measured to be 222.5 ± 3.2 nm (99.9% particles by number), compared to 1632.0 ± 7.0 nm for sonicated bare FeS.

After 6 months of storage at 4°C , the CMC-FeS nanoparticles remained suspended in the solution, whereas the DLS based hydrodynamic diameter increased slightly to 245.6 ± 0.5 nm. DLS measurements also revealed that as long as the CMC-to-FeS molar ratio was kept at 0.001, the hydrodynamic diameter remained constant at ~ 225 nm when the FeS concentration was varied from 100 to 1000 mg/L. This observation suggests that the transportability of the nanoparticles is likely independent of the nanoparticle concentration.

Zeta potential (ζ) is an important parameter that can reflect the stability of colloidal dispersions and the degree of electrostatic repulsion among colloids. ζ for CMC-FeS was between -43 and -68 mV over the pH range of 5 to 11, the surface remained negative at pH as low as 2.5 ($\zeta = \sim 22$ mV). The highly negative surface of CMC-FeS confirmed that the attachment of CMC on the FeS particles induced strong electrostatic repulsion, thereby preventing the particles from agglomeration. Based on the ζ measurements, the pH of the point of zero charge (PZC) would be < 2.5 , which is much lower than those reported for bare FeS, e.g. 7.5 for disordered mackinawite by Wolthers et al (2005), 5.7 by Liu and Huang (1992), and 2.9 by Widler and Seward (2002).

3.3.2 Immobilization of mercury: batch tests

The effectiveness of CMC-FeS nanoparticles for immobilization of Hg in the field contaminated soils and sediment was tested in a series of batch experiments. **Figure 3-2a** shows the transient release of Hg when 2.7 g of sediment AL1 was mixed with 27 mL of DI water or the nanoparticle suspension containing various concentration of FeS. The initial Hg peaking during the DI water leaching tests can be attributed to the heterogeneous Hg binding sites in the

sediment, i.e., Hg is released from lower energy sites and then bound to higher energy sites (Kot et al., 2007). In the absence of the nanoparticles, the aqueous phase concentration of Hg reached $87.13 \pm 9.08 \mu\text{g/L}$ during the 48 hours of leaching tests. In the presence of 100, 200, 500, and 1000 mg/L of CMC-FeS nanoparticles, the steady state Hg leached was reduced by 83%, 92%, 95% and 96%, respectively. The steady state was achieved between 4 hours (CMC-FeS = 1000 mg/L) and 24 hours (CMC-FeS = 100 mg/L).

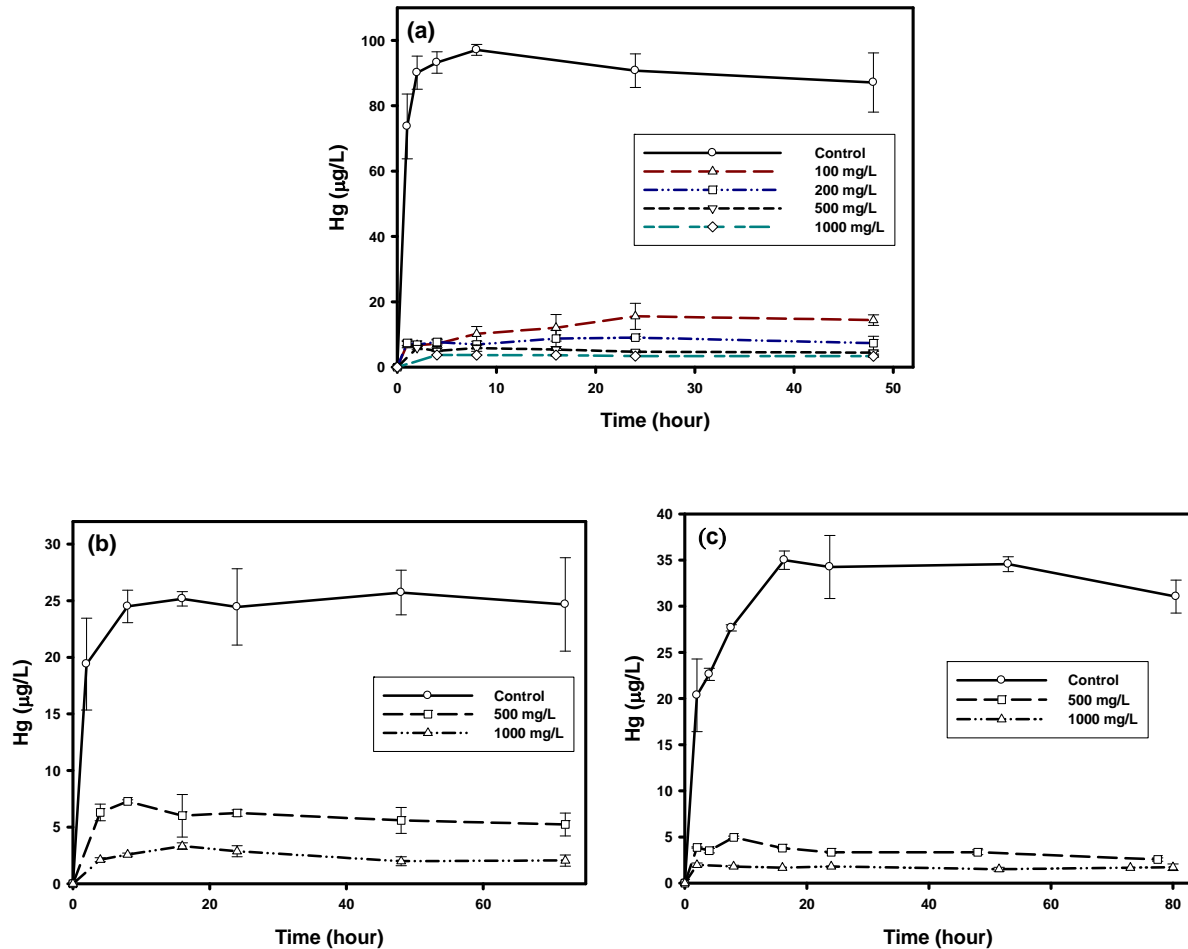


Figure 3-2. Desorption of Hg from (a) Hg-spiked sediment AL1, (b) soil NJ4, and (c) soil NJ38 in the absence or presence of various concentrations of CMC-FeS nanoparticles. Initial Hg

content in the samples was 247.67 mg/kg, 400.52 mg/kg, and 193.04 mg/kg, respectively. The pH value was constant during the whole reaction for all cases (7.0 for AL1 and NJ38, and 7.8 for NJ4). Data plotted as mean of duplicates, and error bars indicate standard derivation from the mean.

Figure 3-2b shows the Hg leaching histories when 2.7 g of soil NJ4 was mixed with 27 mL of DI water or the nanoparticle suspensions containing 500 or 1000 mg/L FeS. In the absence of CMC-FeS, the Hg desorption reached steady state after 16 hours, with an aqueous Hg concentration of 24.68 ± 4.13 $\mu\text{g/L}$. In the presence of 500 and 1000 mg/L of CMC-FeS, the Hg leached was reduced by 79% and 92%, respectively, during the 72 hour testing.

Figure 3-2c shows the transient release of Hg when 1.35 g of another field contaminated soil NJ38 was mixed with 27 mL of DI water or a nanoparticle suspension of 500 or 1000 mg/L FeS. In the absence of the nanoparticles, the peak aqueous phase concentration of Hg reached 34.56 ± 0.80 $\mu\text{g/L}$ during the testing period of 80 hours. In the presence of 500 and 1000 mg/L of CMC-FeS, the Hg mass leached was reduced by 90% and 96%, respectively. At CMC-FeS = 1000 mg/L, the steady state concentration of 1.51 ± 0.21 $\mu\text{g/L}$ was achieved within 3 hours. However, at FeS = 500 mg/L, the Hg concentration continued to decrease till nearly 80 hours, suggesting Hg adsorption to the nanoparticles' high energy sites was still taking place. After 78 hours, the aqueous phase Hg concentration reached 2.56 ± 0.18 $\mu\text{g/L}$.

Although the three media fall into the same soil category of sandy clay loam, they displayed markedly different Hg leaching profiles. For the two field contaminated soils NJ4 and NJ38, although both soils have been contaminated for several decades, a small, yet enough to be harmful, fraction of Hg remained water leachable. NJ4 contained >2 times greater Hg than NJ38,

indicating its greater Hg sorption capacity and affinity. Accordingly, the Hg leachability of NJ4 was much lower than that of NJ38 (the water-leached Hg was 0.062% for NJ4 and 0.36% for NJ38). SOM and clay contents have been associated with high mercury retention (Parkpoin et al., 2001). Diffusion of Hg through intraparticle micropores of SOM was held responsible for irreversible sorption of Hg (Yin et al., 1997). These assertions are supported by the fact that NJ4 contained higher SOM and clay (5.5% SOM and 33.3% clay) than NJ38 (4.1% SOM and 26.7% clay) (**Table 3-1**). In addition, the binding of Hg to high affinity sites, such as S-containing groups, can lead to irreversible Hg adsorption (Reimers and Krenkel, 1974). This is consistent with the fact that the sulfur content of NJ4 was nearly twice that of NJ38 (**Table 3-1**). For the sediment AL1, a much greater Hg leachability was evident (**Figure 3-2**), which can be attributed to: 1) the spiked Hg was less aged, and thus, more reversible, and 2) the SOM and lay contents (1.0% and 20.0%, respectively) were much lower.

The relative Hg sorption capacity and affinity can be approximately measured by the equilibrium Hg distribution coefficient (K_d) between the aqueous phase and the solid phase:

$$K_d = \frac{q}{C} \quad (\text{Eq. 3.4})$$

where q and C are Hg concentrations in the solid (soil/sediment and FeS) and aqueous phases, respectively. **Table 3-2** lists the K_d values for the sediment and soil samples in the absence or presence of CMC-FeS. Evidently, the addition of the nanoparticles greatly enhanced the solid phase Hg capacity and affinity by serving as a strong sink, resulting in the much lower aqueous phase Hg concentration. Separate Hg sorption isotherm tests (data not shown) with CMC-FeS revealed a K_d value of 19,131 L/g over an equilibrium Hg concentration range of 0-140 $\mu\text{g/L}$, which is more than three orders of magnitude greater than K_d for the sediment/soils.

Table 3-2. Equilibrium Hg distribution coefficient (K_d) for the sediment/soil in the absence and presence of CMC-FeS nanoparticles.

Sample	CMC-FeS (mg/L)	C ($\mu\text{g/L}$)	K_d (L/g)
AL1	0	87.1	2.8
	100	14.4	17.2
	200	7.4	33.6
	500	4.5	55.4
	1000	3.4	73.0
NJ4	0	24.7	16.2
	500	5.2	76.2
	1000	2.0	196.3
NJ38	0	34.6	5.6
	500	3.3	57.1
	1000	1.5	125.7

3.3.3 TCLP leachability of Hg

TCLP has been used as a standard method for classifying hazardous wastes including Hg (Ghosh et al., 2004). TCLP-based Hg leachability tests were performed with the untreated and nanoparticle-treated sediment. **Figure 3-3** shows that the TCLP-leachable Hg for the untreated sediment was 51.1 $\mu\text{g/L}$, which exceeded the TCLP threshold of 25 $\mu\text{g/L}$ according to Land Disposal Restrictions for low Hg wastes. When treated with 100 mg/L of CMC-FeS, the leached Hg concentration was reduced to 2.5 $\mu\text{g/L}$ (a 95% reduction). Increasing the CMC-FeS dosage by 10 times further lowered to 1.5 $\mu\text{g/L}$, which was only a 1% gain, and thus, may not be practical. For the two field contaminated soils, the effectiveness was somewhat discounted. At an FeS dosage of 500 mg/L, the TCLP-leached Hg concentration was reduced by 26% and 76% for NJ4 and NJ38, respectively. The lower effectiveness can be attributed to the interferences of some soluble soil compositions. Note that while the two the field contaminated soils were used as they were obtained, Hg spiking was applied to AL1. Ineluctably, some soluble sediment

compositions and fine colloids were lost during the spiking for AL1, which resulted in a “cleaner” sediment compared to the intact raw soils.

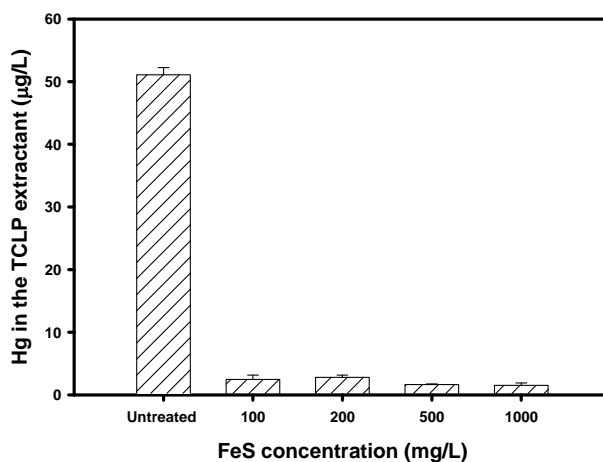


Figure 3-3. Hg concentrations in the TCLP #1 fluids for Hg-loaded sediment AL1 before and after FeS nanoparticles treatments (Reaction time: 18 hours). Data plotted as mean of duplicates, and error bars indicate standard derivation from the mean.

3.3.4 Deliverability and transport of CMC-stabilized FeS nanoparticles in sediment and soil

To demonstrate the soil/sediment deliverability and transport behavior of the nanoparticles, column breakthrough tests were carried out with the sediment AL1. **Figure 3-4a** shows breakthrough profiles of a tracer (KBr) and CMC-FeS through a column packed with the sediment AL1. The full breakthrough of the nanoparticles occurred at ~9 pore volumes (PVs), compared to ~7 PVs for the tracer. At full breakthrough, about 70% of the influent nanoparticles exited the column and remained constant (i.e. $C/C_0 = 0.7$). For comparison, bare FeS was retained completely on the top of the sediment bed because of the large particle size (1632.00 ± 7.00 nm). This observation indicates that CMC-FeS are deliverable in the sediment

under the external pressure of 0.4 psi (estimated based on Darcy's law), which is attributed to the small particle size (222.5 ± 3.20 nm) and negative surface charges of CMC-FeS. The CMC-FeS breakthrough curve also revealed that $\sim 30\%$ of the delivered nanoparticles were consistently retained during the nanoparticle delivery period. To determine the spatial distribution of the retained nanoparticles, the nanoparticle-laden sediment bed was sectioned into four parts following the breakthrough test, and the amount of the nanoparticles was quantified as total Fe following acid extraction (the background Fe content in the sediment (5.17 mg/g) was deducted in the calculation). Mass balance checking revealed that the nanoparticles recovered from the column effluent and the solid phase extraction amounted to 95% of the mass introduced. **Figure 3-4b** shows that the particle distribution profile is typical of an incipient filtration process, where most (61%) of the retained particles were in the top 2 cm layer. Based on the classical filtration theory (Logan, 1999), a more even distribution is expected as the filtration process proceeds because of the increasing flow shear force in the top layer as the nanoparticles accumulate.

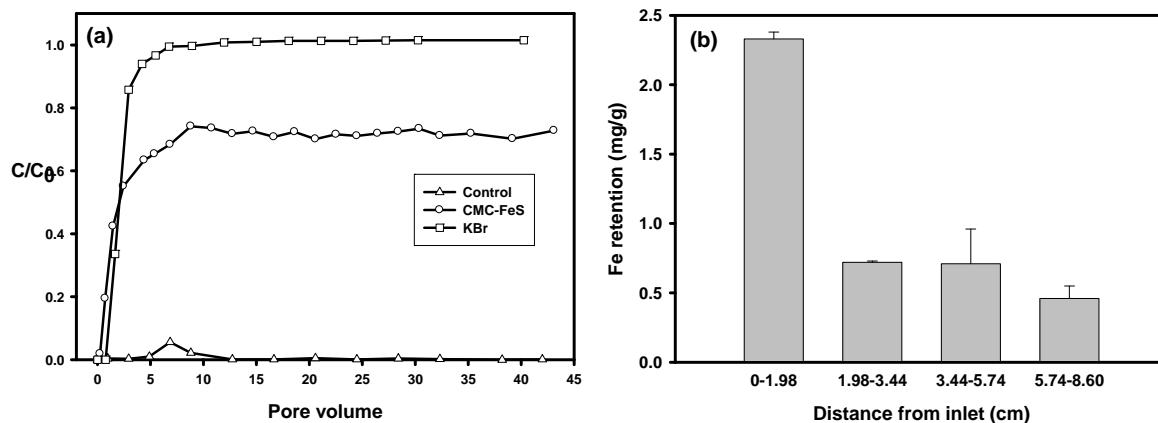


Figure 3-4. (a) Breakthrough curves of a tracer (KBr) and CMC-FeS nanoparticles through sediment AL1 (KBr = 50 mg/L, FeS = 500 mg/L, CMC = 0.05%, pore velocity = 0.22 cm/min,

EBCT = 113 min), and **(b)** Measured FeS nanoparticles retention profiles in the Hg-loaded sediment AL1 column.

From an *in situ* remediation standpoint, transport of the nanoparticles must satisfy two fundamental criteria. On the one hand, the particles must be deliverable to the target contaminated zone (as demonstrated above); on the other hand, when the external injection pressure is released, the delivered nanoparticles themselves should remain immobilized or, to a minimum, remain in a confined domain to avoid nanoparticle-facilitated spreading of the contaminants. Based on the nanoparticle breakthrough curve (**Figure 3-4**) and the filtration modeling approach used by He et al (2009), the maximum transport distance (MTD) of the CMC-FeS nanoparticles was calculated to be 1.11 m under the injection pressure (i.e. 0.4 psi). If desired, the MTD can be increased by elevating the injection pressure. For example, if the injection pressure is doubled, the MTD is increased to 1.85 m (assuming that the attachment efficiency α remains the same). Conversely, under a typical groundwater flow velocity of 0.1 m/d (He et al., 2009), the MTD reduces to 18 cm. Therefore, the injected nanoparticles will retain virtually immobile in the ground under typical natural groundwater flow conditions. From a chemical evolution viewpoint, once CMC is degraded (in weeks to months), the particles become “sticky” again and will either aggregate into larger agglomerates or become associated with the sediment/soil matrices.

Figure 3-5 shows breakthrough profiles of a conservative tracer (KBr) and CMC-FeS through the field soil (NJ4) under an external pressure of 0.5 psi. The full breakthrough plateau ($C/C_0 = 0.8$) of the nanoparticles was reached at ~12 PVs, compared to ~8 PVs for the tracer.

About 20% of the stabilized FeS nanoparticles were retained in the soil after ~50 PVs. The MTD was estimated to be 0.95 m at this injection pressure.

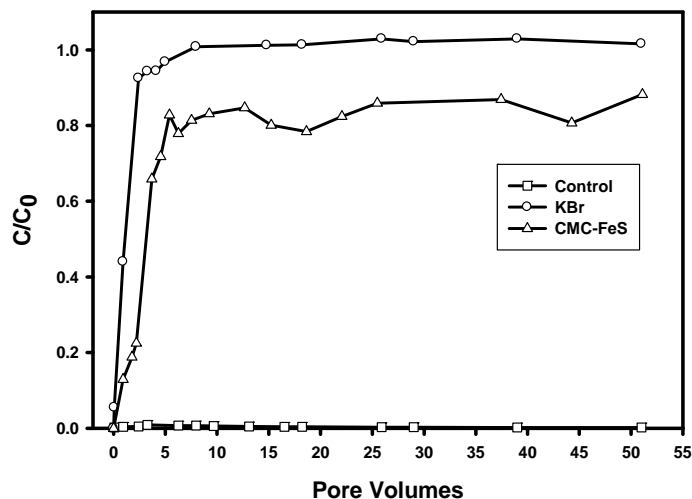


Figure 3-5. Breakthrough curves of a tracer (KBr) and CMC-FeS nanoparticles through soil NJ4 (KBr = 50 mg/L, FeS = 500 mg/L, CMC = 0.05%, pore velocity = 0.10 cm/min, EBCT = 102 min).

3.3.4 *In situ* immobilization of mercury: column tests

Figure 3-6 compares concentration histories of dissolved or free Hg eluted from sediment AL1 during column elution tests using 0.05% CMC solution or a suspension of 500 mg/L CMC-FeS as eluents. The peak dissolved Hg concentration in the effluent was 152 $\mu\text{g/L}$ when CMC solution was used as the eluent, compared to 135 $\mu\text{g/L}$ when the nanoparticle suspension was applied. Based on mass balance calculations, CMC solution eluted ~1% of Hg in the sediment during the 95 PVs elution test, compared to 0.1% with the nanoparticle suspension, a 90% reduction in Hg leachability.

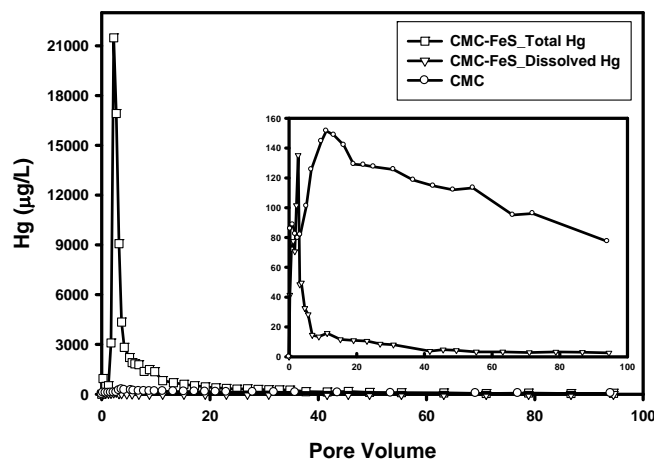


Figure 3-6. Total and dissolved Hg elution histories from Hg-loaded sediment AL1 when subjected to 500 mg/L CMC-FeS nanoparticles or a CMC solution (CMC = 0.05%, pore velocity = 0.22 cm/min, EBCT = 113 min). Inset: a close-up of dissolved Hg concentration histories.

When the effluent Hg was measured as the total Hg (i.e. dissolved and nanoparticle-bound Hg), the nanoparticles leached 5% of the Hg mass from the sediment after 95 PVs of elution, confirming the nanoparticles' strong affinity toward Hg. However, 99% of the total Hg eluted was bound to the nanoparticles (i.e. only ~1% of the Hg was free Hg). This observation reveals that the nanoparticle treatment is largely a process where water-leachable Hg is transferred from the sediment to thermodynamically more stable nanoparticles. Because the delivered nanoparticles are virtually immobile upon removal of the exerted hydraulic head, the Hg associated therewith is immobilized. From the kinetic aspect, the sharp and high peak concentration (22 mg/L) profile of eluted Hg indicates that the most efficient Hg mass transfer occurred within the first 10 PVs treatment, and nanoparticles thereafter primarily serve as an added long-term sink or an *in situ* built sorptive barrier that scavenges any bleeding Hg. Given that Hg desorption from soil/sediment is likely an extremely slow process as evidenced by the

field contaminated soils in this work, delivering some excess amounts of FeS may be necessary to assure long-term effect.

TCLP tests were performed to compare the physical-chemical availability of Hg in the sediment before and after the nanoparticle treatment as presented in **Figure 3-6**. The results showed that the nanoparticle treatment lowered the TCLP extractable Hg from 51 $\mu\text{g/L}$ to 4.4 $\mu\text{g/L}$, a 91% reduction.

Similar column tests were performed with the field contaminated soil (NJ4). **Figure 3-7** shows the dissolved and total mercury elution histories from the soil by using 0.05% CMC solution and a suspension of 500 mg/L CMC-FeS, respectively. In this case, the CMC solution eluted a peak dissolved Hg concentration of 211 $\mu\text{g/L}$, compared to 66 $\mu\text{g/L}$ with the nanoparticle suspension. Mass balance calculations revealed that during the 52 PVs of the tests, the presence of the nanoparticles reduced the water-soluble Hg by 93%. All elution curves displayed an initial peaking followed by slow tailing, although the peak height of total Hg overwhelms that of free Hg. Within 52 PVs of elution, the total Hg and dissolved Hg leached out from the soil amounted to 0.89% and 0.04% of the total soil Hg, respectively. The difference indicates that 96% of the total Hg eluted was associated with the FeS nanoparticles. TCLP tests showed that the Hg concentration in the TCLP extractant was reduced from 22 $\mu\text{g/L}$ to 7.7 $\mu\text{g/L}$ (a 65% reduction) upon the nanoparticle amendment.

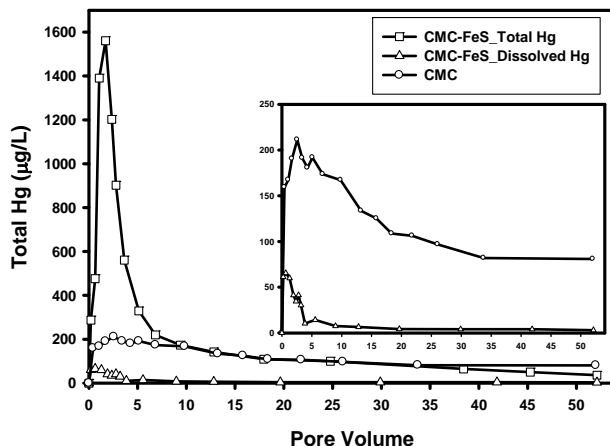


Figure 3-7. Total and dissolved Hg elution histories from soil NJ4 when subjected to 500 mg/L CMC-FeS nanoparticles or a CMC solution (CMC = 0.05%, pore velocity = 0.10 cm/min, EBCT = 102 minutes). Inset: a close-up of dissolved Hg concentration histories.

3.4 Conclusions

This study investigated the feasibility of using a new class of CMC-stabilized FeS nanoparticles to immobilize Hg in some high profile field contaminated sediment/soils through a series of batch and column experiments. The primary findings are summarized as follows:

- (1) The CMC-FeS nanoparticles remained stable both physically and chemically over prolonged period of time (6 months), and the hydrodynamic diameter of the nanoparticles was measured to be 222.5 ± 3.2 nm, which was independent on the FeS concentration.
- (2) The CMC-FeS nanoparticles can be delivered in the field media under the moderate injection pressure (0.4 psi for sediment AL1 and 0.5 psi for soil NJ4). The travel effective distance, measured as MTD, can be manipulated by regulating the injection pressure. The delivered nanoparticles remained virtually mobile under typical groundwater flow conditions.

(3) The CMC-FeS nanoparticles are highly effective for immobilizing water-leachable or TCLP-leachable Hg in sediment/soils. For the Hg-loaded sediment (AL1), the nanoparticles reduced the water-leachable Hg by 96% and the TCLP leachability by 96% at an FeS-to-Hg molar ratio of 92:1. For the field contaminated soil (NJ38), the water-leachable Hg concentration was reduced by 90% and the TCLP leachability by 76% at an FeS-to-Hg molar ratio of 118:1. For the other field soil (NJ4), the water-leachable Hg concentration was reduced by 79% and the TCLP leachability by 26% at an FeS-to-Hg molar ratio of 28:1. In all cases, the nanoparticle treatment lowered the TCLP-leachable Hg to far below the Land disposal restriction threshold of 25 µg/L.

(4) The CMC-FeS nanoparticles showed a very high affinity for Hg ($K_d = 19,131$ L/g). When the Hg-loaded sediment (AL1) was treated with 95 PVs of a 500 mg/L FeS nanoparticle suspension, the water-leachable Hg was reduced by 90%, and the TCLP leachability by 91%. When the Hg-contaminated soil (NJ4) was treated with 52 PVs of a 500 mg/L FeS nanoparticle suspension, the water-leachable Hg was reduced by 93%, and the TCLP leachability by 65%.

The results provide compelling evidence that CMC-stabilized FeS nanoparticles are promising for *in situ* immobilization of Hg in both freshly contaminated sediment and historically contaminated soil.

Chapter 4. Effects of Oil Dispersant and Oil on Sorption and Desorption of Phenanthrene with Gulf Coast Marine Sediments

This chapter investigated effects and mechanisms of a model oil dispersant (Corexit EC9500A) on sorption/desorption kinetics and isotherms of phenanthrene with two Gulf Coast marine sediments. Models were employed to simulate sorption isotherm and kinetic data. Effects of water accommodated oil (WAO) and dispersant-enhanced WAO (DWAO) on the phenanthrene sorption kinetics were also evaluated.

4.1 Introduction

Chemical dispersants have been widely used for mitigating oil spill impacts since the 1950s (Ramachandran et al., 2004). During the 2010 Deepwater Horizon (DWH) oil spill, 859 million liters (5.4 million barrels) of South Louisiana Sweet Crude oil were released, of which 731 million liters (4.6 million barrels) entered the Gulf of Mexico (Griffiths, 2012); and ~7.9 million liters of chemical dispersants (Corexit EC9500A and Corexit 9527A) were applied at the sea surface and near the 1500 m deep wellhead (Kujawinski et al., 2011).

Typically, oil dispersants are mixtures of anionic and nonionic surfactants and solvents. Oil dispersants are able to lower the oil-water interfacial tension, thereby breaking surface oil slicks into fine droplets and facilitating dispersion and dissolution of hydrophobic components of oil into the water column (Kujawinski et al., 2011; Ramachandran et al., 2004). Corexit 9527A consists of two nonionic surfactants (48%) and an anionic surfactant (35%) in an aqueous hydrocarbon solvent (17%) (Scelfo and Tjeerdema, 1991). Corexit EC9500A contains the same

surfactants as Corexit 9527A, but it does not contain 2-butoxy ethanol, which is an ingredient in Corexit 9527A (George-Ares and Clark, 2000).

Polycyclic aromatic hydrocarbons (PAHs) are pollutants associated with oil spills that are of great concern due to their toxicity, mutagenicity, carcinogenicity, and persistency (Nam et al., 2008). The DWH oil contained ~3.9% PAHs by weight, and the incident released $\sim 2.1 \times 10^{10}$ g of PAHs into the Gulf of Mexico (Reddy et al., 2012).

Sorption and desorption affect the transport, physical and biological availabilities, toxicity, and ultimate fate of PAHs in the environment (Johnson et al., 2008). In the marine environment, suspended particulate matter (SPM) is a major transport medium for pollutants (Voice and Weber Jr, 1983; Wu and Gschwend, 1986). Because of their hydrophobic nature, PAHs can be strongly sorbed to SPM and accumulate in bottom or coastal sediments through SPM-facilitated transport and settling (Yang et al., 2005), which can greatly alter the weathering rate and environmental fate of PAHs (Gearing et al., 1980).

Sediment organic matter (SOM) is the key component for sorption of hydrophobic compounds (Braida et al., 2001; White and Pignatello, 1999). In addition to sorption, the extent and rate of desorption are also important factors in controlling physical/biological availabilities of sorbed contaminants (Pignatello and Xing, 1995). Yet, it remains unknown how oil dispersants affect such interactions between sediment particles and persistent oil components such as PAHs.

Due to the amphiphilic nature of surfactants, dispersants can cause contrasting effects on the sorption of PAHs by sediments (Cheng and Wong, 2006; Pan et al., 2009; Zhang and He, 2011). On one hand, a surfactant can increase the apparent solubility of PAHs through its hydrophobic tail which reduces sorption and favors desorption of PAHs. On the other hand, the sorption of

surfactant on sediments enhances the partitioning of additional PAHs onto the immobilized surfactant. The overall effects of a dispersant would depend on the extent of these contrasting factors. Cheng and Wong (2006) observed that desorption of phenanthrene and pyrene from soil was enhanced in the presence of a nonionic surfactant (Tween 80) at concentrations higher than the critical micelle concentration (CMC), however, no significant desorption enhancement was evident in the surfactant concentration range of 0-7.5 mg/L. Pan et al. (2009) reported that the presence of 4.3 mg/L of an anionic surfactant increased sediment sorption of perfluorooctane sulfonate.

The overall goal of this study was to investigate effects of a model oil dispersant (Corexit EC9500A) on the distribution of a model PAH (phenanthrene) in a sediment-seawater system. The specific objectives were to: (1) investigate sorption and desorption behaviors of Corexit EC9500A with representative Gulf Coast marine sediments; (2) determine effects and mechanisms of the dispersant on sorption and desorption isotherms and kinetics of phenanthrene; and (3) evaluate effects of water accommodated oil (WAO) and dispersed WAO (DWAO) on sediment sorption of phenanthrene.

4.2 Materials and methods

4.2.1 Materials

Two marine sediments (0-30 cm) were collected at Grand Bay, AL, USA, in December 2010. The latitudes/longitudes of the two sites were 30.37926/88.30684 and 30.37873/88.30679, respectively. The sampling sites sit in the neighborhood with some sites affected by the DWH oil spill, such as Bayou La Batre and Dauphin Island (**Figure A-1**). The wet sediments were placed in sealed plastic buckets and shipped within four hours to the lab and stored in a refrigerator (4 °C). The sediment samples were wet-sieved with seawater to obtain a size fraction of 75-840 μm

and then air-dried for 7 days. The aggregates were broken by a ceramic mortar and pestle. Subsamples used for sorption/desorption experiments were oven dried for 6 hours at 80 °C. These relatively moderate pretreatments were necessary to eliminate interferences such as fine colloids, water-leachable compositions, and biological activities. While it was attempted to minimize alteration of the natural characteristics of the sediments, it is inevitable that the treated sediments may deviate from the original materials in the physical-chemical and biological properties. Therefore, cautions should be exercised when applying the research results to the natural marine sediments. In particular, the biological activities are eliminated in this work. The sediments were classified as loamy sand and sandy loam based on particle size analysis (**Table 4-1**). Seawater samples were collected from the top 30 cm of the water column from the same area. The seawater was first filtered through 0.45 µm membrane filters to remove suspended solids, and then sterilized at 121 °C for 35 minutes via autoclaving.

All chemicals used in this study were of analytical or higher grade. ¹⁴C-radiolabeled phenanthrene (in methanol) with a specific activity of 52.0 mCi/mmol (99.5% purity) was purchased from Moravek Biochemicals Inc. (Brea, CA, USA). Nonradioactive phenanthrene, methanol, and dichloromethane were purchased from Alfa Aesar (Ward Hill, MA, USA). Sodium azide (NaN₃) and sodium sulfate (Na₂SO₄) were obtained from Fisher Scientific (Fair lawn, NJ, USA). Corexit EC9500A was acquired through the courtesy of Nalco Company (Naperville, IL, USA). **Table 4-2** shows salient surfactant compositions of the dispersant. The CMC value of Corexit EC9500A was determined following the surface tension measurement method (Ahn et al., 2010). A surrogate Louisiana sweet crude oil was used. According to the manufacture, the oil is physically, chemically, and toxicologically similar to the Macondo Well crude oil in Mississippi Canyon Block 252.

4.2.2 Seawater and sediment analyses

Salient properties of the seawater sample are: pH = 8.8, dissolved organic carbon (DOC) = 0.43 mg/L, $\text{Cl}^- = 18.55 \text{ g/L}$, $\text{NO}_3^- = 2.55 \text{ g/L}$, $\text{SO}_4^{2-} = 4.25 \text{ g/L}$, and an ionic strength of 0.7 M. Sodium azide was added to the seawater at 200 mg/L to minimize bacterial activity during batch sorption/desorption experiments. Sediment analysis was performed by the Soil Testing Laboratory at Auburn University. Method details have been described elsewhere (Gong et al., 2012). **Table 4-1** gives salient properties of the sediments. **Tables A-1** shows that 6 PAHs were detected at the ppb level in the filtered seawater, 8 and 10 PAHs were detected at ppb or sub-ppm levels in the unheated loamy sand and sandy loam sediments, respectively. Despite the oil exploration activities in the Gulf region and the DWH oil spill, the concentrations are relatively low. The reasons include: 1) The sampling sites were harbored in the ~250 m inlet within the bay area, 2) The sites were shielded by several naturally belt-shaped offshore islands such as the Dauphin Island and the Petit Bois Island, and 3) There have been fewer boating activities nearby. Upon the aforementioned heat treatments, all PAHs became undetectable presumably due to oxidation of the PAHs at elevated temperatures.

Table 4-1. Salient physical and chemical properties of marine sediments used in this work.

Sample	Nitrogen ^a (%)	Carbon ^a (%)	Sulfur ^a (%)	SOM ^b (%)	pH ^c	Cation Exchange Capacity (meq/100g)					Sand ^d (%)	Silt ^d (%)	Clay ^d (%)	Textural Class ^e
Loamy Sand	0.07	0.43	0.210	0.7	7.00	21.21					85.0	5.0	10.0	Loamy Sand
Sandy Loam	0.15	1.58	0.682	2.7	7.38	37.38					56.3	31.3	12.5	Sandy Loam
Sample	Ca	K	Mg	P	Al	Cd	Cr	Cu	Fe	Mn	Na	Ni	Pb	Zn
	(mg/kg)													
Loamy Sand	301	177	536	11	60	0.1	0.1	5	241	35	3068	0.1	1	4
Sandy Loam	780	336	988	8	119	0.3	0.1	11	701	65	5057	0.4	2	9

^a Total carbon, nitrogen and sulfur contents were determined following the combustion method (Kirsten, 1979).

^b SOM was obtained based on the empirical relationship: SOM = 1.72×TOC (Davies, 1974).

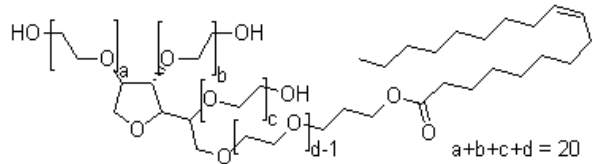
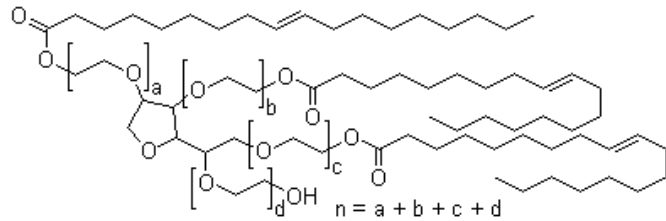
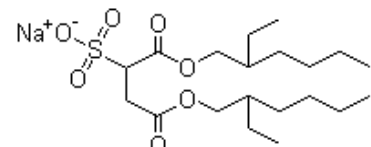
^c Sediment pH was measured on a 1:1 sediment:water mixture via the Reference Soil Test Methods (UGA, 1983).

^d Categorized based on USDA-definition.

^e Sediment texture was conducted following the hydrometer method (Bouyoucos, 1962).

Note: Metal contents were measured per EPA method 3050B. Soil calcium, magnesium, potassium and sodium were first extracted per the Mehlich 1 procedure, filtered through a #1 qualitative filter paper, and then determined by a Varian Vista-MPX Radial Spectrometer.

Table 4-2. Characteristics of surfactant compositions in the oil dispersant Corexit EC9500A.

Surfactants	Ionic property	Molecular formula	Molecular weight (g/mol)	Critical micelle concentration (CMC) (mg/L)	Chemical structure
Polyoxyethylene (20) sorbitan monooleate (Tween 80)	Neutral	$C_{64}H_{124}O_{26}$	1310	14 (Yeom et al., 1995)	
Polyoxyethylene(20) sorbitan trioleate (Tween 85)	Neutral	$C_{60}H_{108}O_8(C_2H_4O)_n$		23 (Wan and Lee, 1974)	
Sodium dioctyl sulfosuccinate (SDSS)	Anionic	$C_{20}H_{37}NaO_7S$	444.56	578 (Yehia, 1992)	

4.2.3 Sorption and desorption of Corexit EC9500A by sediment

Batch experiments were conducted in duplicate to determine dispersant sorption isotherms with sandy loam using 43-mL glass vials with Teflon-lined caps. Each vial was first filled with 0.21 g of sandy loam mixed with 2 mL of seawater, and then filled with 40 mL of dispersant solutions, resulting in initial dispersant concentrations from 0 to 1080 mg/L. The mixtures were then equilibrated on an end-to-end rotator at 30 rpm kept at 21 ± 1 °C for 5 days. Then, the solids were separated from aqueous solution by centrifuging at 3000 rpm for 10 minutes, and aliquots (40 mL each) of the supernatants were pipetted out for surface tension analysis (CSC-DuNoüy Tensiometer, Central Scientific Company, Fairfax, VA, USA). The dispersant concentration was then determined based on the surface tension. Control tests conducted without the sediments showed that the loss of dispersant due to sorption to the vial walls and septa was <5% in all cases. Dispersant uptake by the sediment (mg/g) was calculated based on the difference in initial and final aqueous dispersant concentrations.

To test sorption reversibility of the dispersant, desorption isotherm tests were carried out. Following the sorption equilibrium, 99% of the supernatant was replaced with an equal volume of dispersant-free seawater. To assure equal background compositions, the sediment-amended replacement seawater was first amended with the same sediment by mixing the sediment with seawater at the same sediment-to-water ratio as in sorption isotherm tests. The vials were then re-equilibrated for 7 days, and desorption isotherms were then obtained in the same manner.

4.2.4 Effects of dispersant on sorption/desorption kinetics of phenanthrene

A stock solution of nonradioactive phenanthrene was prepared at 1.4 g/L in methanol. The ¹⁴C-radiolabeled phenanthrene was diluted 10 times using methanol. The two solutions were then

mixed at a volume ratio of 1:9, which was then diluted with seawater to a phenanthrene concentration of 630 µg/L.

Batch phenanthrene sorption kinetic tests were conducted in duplicate in 43-mL glass tubes with Teflon-lined caps. First, a known mass of sterilized sediments (1.05 g of loamy sand or 0.21 g of sandy loam) was mixed with 2 mL of seawater in each vial. The phenanthrene sorption was then initiated by adding 40 mL of the phenanthrene solution to each sediment-seawater suspension, which resulted in an initial phenanthrene concentration of 600 µg/L. Nearly zero headspace was maintained in the vials to minimize volatilization loss of phenanthrene. The volume fraction of methanol in all cases was <0.1% to avoid co-solvent effect. The vials were then sealed and rotated on an end-to-end rotator operated at 60 rpm in an incubator at 21 ± 1 °C. After the predetermined time intervals, vials were sacrificially centrifuged at 3000 rpm for 10 minutes to separate the solids from the solution. After 5 minutes, 1 mL of each supernatant was sampled and added to 10 mL of Ecoscint cocktail (National Diagnostics, Atlanta, GA, USA) for liquid scintillation counting. To determine the dispersant effect, the kinetic tests were also carried out in the presence of 18 mg/L of Corexit EC9500A. Control experiments carried out without sediments showed that phenanthrene loss was consistently <4%.

Following the sorption equilibrium, phenanthrene desorption tests were initiated by replacing 99% of the supernatant with an equal volume of sediment-amended seawater. The vials were then mixed and sacrificially sampled in the same manner as in the sorption tests. To evaluate effects of the dispersant on the desorption rate and extent, four experimental scenarios were evaluated: (1) Phenanthrene was pre-sorbed onto the sediments without dispersant, then subjected to desorption without dispersant; (2) Sorption was the same as in scenario (1), but desorption was conducted with dispersant; (3) Phenanthrene was pre-sorbed on the sediments

with dispersant, then subjected to desorption without dispersant; and (4) Sorption was the same as in scenario (3), but desorption with dispersant.

4.2.5 Effect of dispersant on sorption/desorption isotherms of phenanthrene

Sorption isotherm tests were conducted following the same protocols as described in Section 2.4 with an equilibration time of 5 days and a range of initial phenanthrene concentrations (24-864 µg/L). Isotherms were constructed in the presence of 0, 18 and 180 mg/L of the dispersant. Control tests without the sediments showed that the loss in phenanthrene and the dispersant was <4%. Following the sorption equilibrium tests, desorption isotherms were obtained by replacing 99% of each supernatant with an equal volume of the replacement fluid, and re-equilibrating the systems for 7 days. To test effects of the dispersant on sorption reversibility, the equilibrium tests were carried out according to the aforementioned four scenarios.

To confirm mass balance, phenanthrene in the sediment phase was extracted with hot methanol (1.05 g loamy sand in 50 mL methanol, and 0.21 g sandy loam in 40 mL methanol) at 70 °C for 4 hours. Mass balance results showed that the overall error was <5%.

4.2.6 Dual-mode sorption equilibrium and kinetic models

The dual-mode model proposes that SOM consists of expanded rubbery and condensed glassy domains. It is assumed that sorption of PAHs on SOM results from a combination of solid-phase dissolution (partitioning) in the rubbery domain and adsorption (or hole-filling) in the glassy domain of SOM (Pignatello, 1998; Pignatello and Xing, 1995; Xing et al., 1996). For a single solute, the dual-mode isotherm model equation is as follows:

$$q_e = K_D C_e + \frac{bQC_e}{1+bC_e} \quad \text{(Eq. 4.1)}$$

where q_e is the equilibrium uptake, C_e the solute concentration in solution, K_D the partition coefficient between the solution and the dissolution domain of SOM (including sorbed dispersant

aggregates), and b and Q are the Langmuir affinity and capacity coefficients, respectively. It is assumed that the uptake of the dispersant on sediments adds an additional domain of partitioning. As a result, the first term in Eq. (1) includes phenanthrene partitioning in both immobilized dispersant and the rubbery domain of SOM. The model parameters (K_D , b and Q) were acquired through fitting the model to the corresponding experimental isotherms.

The dual-mode radial diffusion model was used to simulate the sorption kinetic data. The governing equation is (Zhao et al., 2002):

$$\frac{\partial q_D}{\partial t} = D_a \left(\frac{\partial^2 q_D}{\partial r^2} + \frac{2}{R} \frac{\partial q_D}{\partial r} \right) \quad (\text{Eq. 4.2})$$

where q_D is the uptake in the dissolution domain, r is the radial coordinate, t is time, and D_a is the apparent diffusivity defined by

$$D_a = D_D \left(1 + \frac{bQ/K_D}{[1+(b/K_D)q_D]^2} \right) \quad (\text{Eq. 4.3})$$

where D_D is the diffusivity in the dissolution domain. The equation was solved using the Crank-Nicolson finite difference method under the batch experimental initial and boundary conditions. The value of D_D/r_0^2 was obtained by fitting the model to the experimental kinetic data.

4.2.7 Effects of dispersant dosage on phenanthrene uptake

Effects of dispersant dosage on equilibrium uptake of phenanthrene by the sediments was tested following the same protocol as in the sorption kinetic tests (Section 4.2.4), but with a broader span of dispersant concentration from 0 to 860 mg/L and an equilibration time of 5 days.

4.2.8 Effects of WAO and DWAO on sorption kinetics of phenanthrene

WAO and DWAO were prepared with the surrogate oil following the protocol (Singer et al., 2000). The procedure represents a compromise which balances the need to prepare environmentally realistic media with the requirement for media of highly repeatable

compositions (Singer et al., 2000). WAO was prepared in 2200 mL glass aspirator bottles containing a hose bib fitted with silicon tubing and clamp at the bottom of the vessels. Each bottle was filled with 1760 mL of seawater, leaving a 20% headspace. Crude oil was carefully added at the volume ratio of 1:200 to the seawater surface, and the mixture was sealed and magnetically stirred for 18 hours. The stir plate was adjusted to obtain an oil vortex of 25% of the total volume of seawater. The mixture was then allowed to gravity-settle for 6 hours. Then, the WAO fraction was collected in glass vials with Teflon lined caps from the bottom without disturbance of the oil/seawater surface, allowing no headspace in the vials. DWAO was prepared following the same protocol except that the dispersant was added to the oil-seawater mixture at a dispersant:oil volume ratio of 1:20.

To determine the effects of WAO and DWAO on phenanthrene sorption, batch sorption kinetic tests were performed following the same procedure as described in Section 2.4 except that known amounts of WAO or DWAO were present.

Petroleum hydrocarbons in the aqueous phase were extracted using dichloromethane in three consecutive steps (10 mL solution with 2 mL dichloromethane in each step) (Ramachandran et al., 2004). The extracts were then passed through 0.3 g anhydrous granular sodium sulfate loaded in a Pasteur pipette to remove moisture (Saeed et al., 2011), and then blown to dryness under a stream of nitrogen gas. The dried extracts were re-dissolved in 0.2 mL of dichloromethane for Gas chromatography-mass spectrometry (GC-MS) analysis.

4.2.9 Chemical analysis

Petroleum hydrocarbons in WAO/DWAO were analyzed using a GCT Premier time-of-flight (TOF) mass spectrometer operated in the splitless mode. A DB-5 fused silica capillary column (length 30 m; inner diameter 0.25 μm ; film thickness 0.25 μm) was used to separate the analytes.

The GC oven temperature was programmed as follows: 80 °C (hold for 3 mins), ramp to 160 °C at 10 °C/min, ramp to 280 °C at 4 °C/min, and ramp to 300 °C at 20 °C/min (hold for 2 mins). Helium was used as the carrier gas (flow rate = 1.0 mL/min), and sample injection volume was 3 µL. The system was operated in the total ion current mode, and the chemical compounds were identified through high probability matching using the NIST spectral library.

Total organic carbon (TOC) was measured by a Tekmar Dohrmann Pheonix 8000 UV-Persulfate TOC analyzer (Mason, OH, USA) with a detection limit of 0.1 mg/L. Solution pH was measured using an Oakton pH meter (pH 510 Benchtip Meter, Oakton, CA, USA). SO_4^{2-} , Cl^- and NO_3^- were analyzed using a Dionex ion chromatography system (Dionex, Sunnyvale, CA, USA) equipped with an AS14 column, with a detection limit of 0.2, 0.2, and 0.1 mg/L, respectively.

4.3 Results and discussion

4.3.1 CMC value of Corexit EC9500A

Figure 4-1 shows the surface tension (ST) as a function of the dispersant concentration. ST decreased linearly with a sharper slope of -21.32 at $\log(\text{dispersant}) < 1.3$, then underwent a distinctive turn at elevated dispersant concentrations to a slope of -10.12. The CMC value was then located at the dispersant concentration of 22.5 mg/L, where the two regression lines intersect (Ahn et al., 2010).

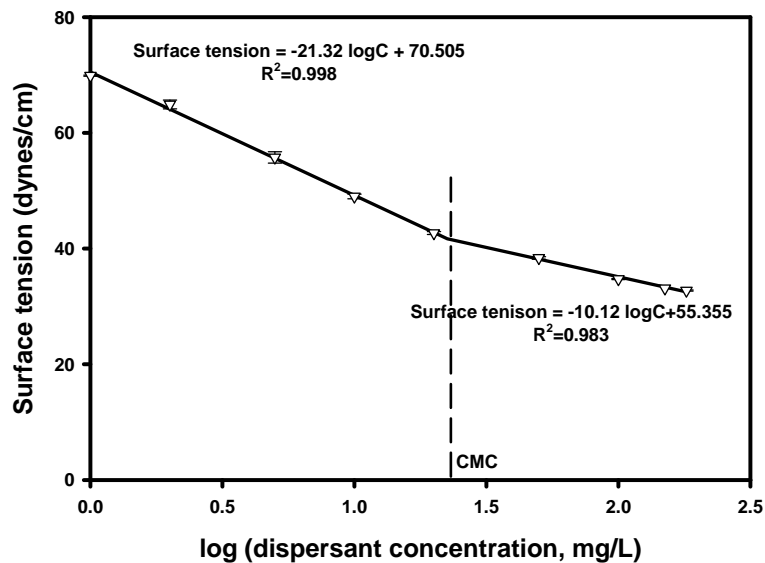


Figure 4-1. Solution surface tension as a function of concentration of Corexit EC9500A for determination of the apparent CMC value of the dispersant.

Since Corexit EC9500A is a mixture of three surfactants, the apparent CMC should be envisioned as a lumped parameter reflecting the collective effects of the surfactants and co-solvents. Interestingly, the mixture CMC was nearly the same as that (23 mg/L) of Tween 85, higher than that (14 mg/L) of Tween 80, but much lower than that (578 mg/L) of sodium dioctyl sulfosuccinate (SDSS) (**Table 4-2**). This observation suggests that Tween 85 plays a predominant role in the mixed micelles (Ahn et al., 2010). While both nonionic surfactants tend to partition into anionic surfactant micelles or semimicelles, Tween 80 is more prone to interact with the anionic surfactant due to its smaller molecular size (Zhao et al., 2005). The interaction of nonionic surfactants with the anionic surfactant decreases the repulsive forces among the ionic heads of the anionic surfactant, and the hydrophobic interactions of the alkyl chains of anionic and nonionic surfactants facilitate formation of mixed micelles at a much lower concentration than the CMC of SDSS (Zhao et al., 2005).

4.3.2 Sorption and desorption of Corexit EC9500A

Figure 4-2 presents sorption and the corresponding desorption isotherms of the dispersant with sandy loam. The sorption isotherm exhibits the characteristic S-shape, indicative of transition of monomeric uptake to formation of dispersant hemimicelles or admicelles on the sediment surface (Ko et al., 1998a). At dispersant concentration <123 mg/L (designated as region 1), low (<8.4 mg/g) but steadily growing dispersant uptake was observed. In the dispersant concentration range from 123 to 211 mg/L (denoted as region 2), the sorption capacity increased sharply from 8.4 to 134.5 mg/g. At elevated dispersant concentrations (>211 mg/L) (region 3), a sorption plateau (~156.3 mg/g) was reached.

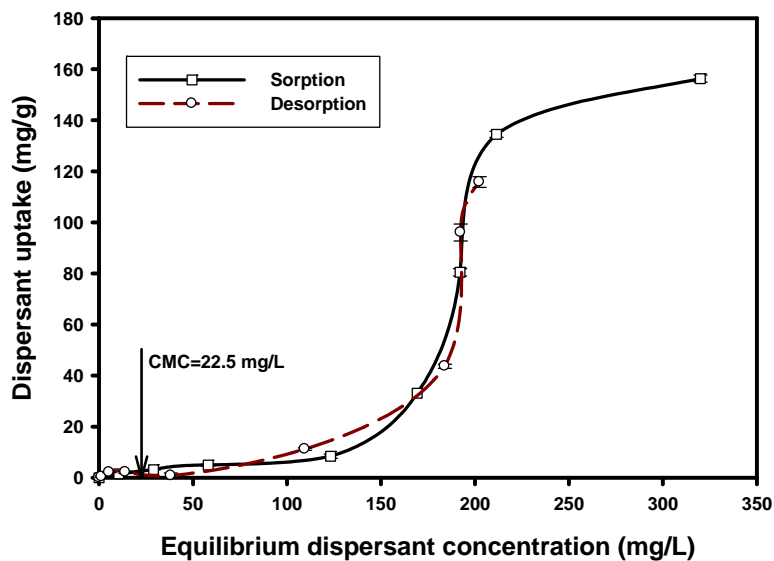


Figure 4-2. Sorption and the corresponding desorption isotherms of Corexit EC9500A on a sandy loam sediment. Experimental conditions: sandy loam = 0.21 g, dispersant initial concentration = 0-1080 mg/L, solution volume = 42 mL, and pH = 6.7-7.4. Data are plotted as mean of duplicates, and error bars indicate standard error from the mean.

In the low concentration region 1, the dispersant was adsorbed as monomers. Sorption of SDSS is not favored due to electrostatic repulsions between the anionic headgroups and the negatively charged sediment surface, which results from deprotonation of the SOM functional groups (e.g., carboxyls and hydroxyls) (Shen, 1999) at the prevailing pH. Sorption of the dispersants results from hydrogen bonding between the hydrophobic surfactant tails and SOM (Zhang and Zhu, 2010). In region 2, the surfactant concentration is sufficiently high to offset the electrostatic repulsion, as such, sorbed surfactant monomers begin to aggregate and form hemimicelles/admicelles presumably through lateral interactions of the hydrophobic tails (Ko et al., 1998b). A sorption plateau (~156.3 mg/g) was reached at elevated dispersant concentrations (>211 mg/L), owing to elevated electrostatic repulsion, saturation of surface coverage, and/or the attainment of a constant surfactant monomer concentration in the aqueous phase (Ko et al., 1998b).

Figure 4-2 also shows that the desorption isotherm nearly coincides with the sorption isotherm, indicating that the dispersant sorption was a reversible process, which excludes the possibility of irreversible deformation of SOM and/or precipitation of SDSS with mineral ions from the sediment such as Ca^{2+} and Mg^{2+} (Zhang and Zhu, 2010).

4.3.3 Effects of dispersant on sorption kinetics of phenanthrene

Figure 4-3 shows phenanthrene sorption kinetics with the two sediments in the absence or presence of 18 mg/L of Corexit EC9500A. In the absence of the dispersant, loamy sand removed 67% of phenanthrene at equilibrium within 96 hours (**Figure 4-3a**). The presence of the dispersant increased the phenanthrene uptake by 7%. Likewise, the dispersant increased phenanthrene uptake from 66% to 71% for sandy loam after 96 hours (**Figure 4-3b**). Based on the t-tests, the differences between the equilibrium phenanthrene uptakes with and without

dispersant for both sediments are statistically significant with a p value of <0.05 at the 0.05 level of significance.

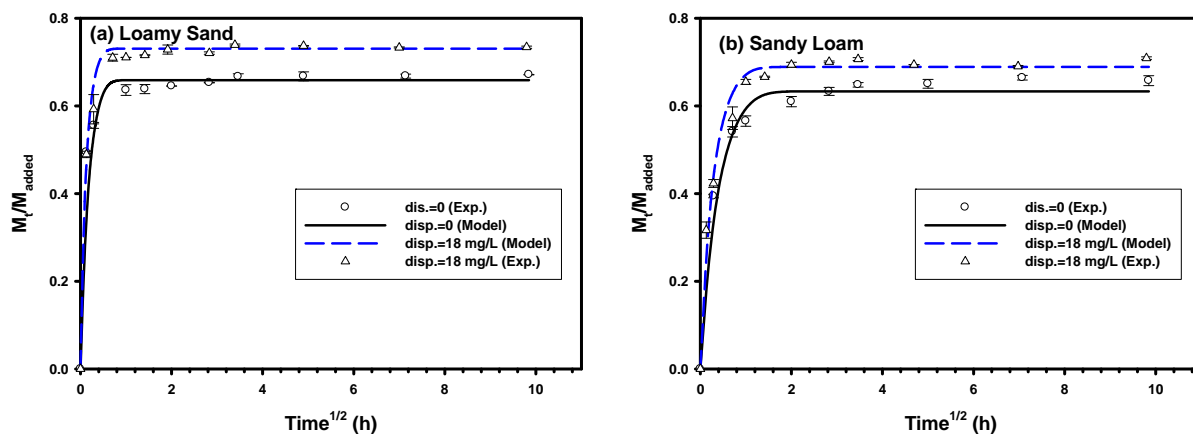


Figure 4-3. Sorption kinetics of phenanthrene onto (a) loamy sand and (b) sandy loam sediments in the absence or presence of 18 mg/L of Corexit EC9500A. Experimental conditions: initial phenanthrene = 600 $\mu\text{g/L}$, pH = 7.4-7.9, loamy sand = 1.05 g, sandy loam = 0.21 g, and solution volume = 42 mL. M_t : phenanthrene mass uptake at time t , and M_{added} : total mass in the system. Symbols: experimental data, lines: dual-mode model fittings. Data are plotted as mean of duplicates, and error bars indicate standard error from the mean.

The dispersant can affect phenanthrene uptake by sediments in two ways (Park and Jaffe, 1993; Yuan et al., 2007): First, sediment sorbed dispersant provides additional sorption capacity. Second, the dispersant increases the solubility of phenanthrene in the aqueous phase (Figure A-2), which diminishes the thermodynamic driving force for phenanthrene diffusion and sorption. The overall effect depends on the extent of these two contrasting factors. In the presence of 18 mg/L dispersant, considering the strong sorption of the dispersant on sediments (Figure 4-2) and the weak solubilization of phenanthrene (Figure A-2), the phenanthrene uptake was enhanced.

The equilibrium phenanthrene distribution coefficient (K_d) between the sediment phase and the aqueous phase was determined to be 81 mL/g for loamy sand and 388 mL/g for sandy loam in the absence of the dispersant. The dispersant increased the K_d values to 114 and 490 mL/g, respectively. Note that the greater K_d value for sandy loam results from its higher SOM content (2.7%) than loamy sand (0.7%) (**Table 4-1**).

To estimate the relative contribution of the sorbed dispersant to overall phenanthrene uptake, K_d is split into two terms (Lu and Zhu, 2012):

$$K_d = \frac{q_e}{C_e} = K_{oc}f_{oc} + K_{df}Q_{df} \quad (\text{Eq. 4.4})$$

where K_{oc} is the sediment organic carbon-normalized distribution coefficient, f_{oc} is the mass fraction of sediment organic carbon, which is calculated based on SOM fraction ($f_{om} = 1.72 \times f_{oc}$), K_{df} is the dispersant-normalized distribution coefficient, and Q_{df} is the mass fraction of the sorbed dispersant, which was estimated to be 1.5 mg/g from dispersant sorption isotherm (**Figure 4-2**). For sandy loam, K_{df} was calculated to be 67.6 mL/mg, which was 2.7 times greater than K_{oc} for the sediment (24.7 mL/mg).

Based on the sorption equilibrium parameters (**Table 4-3**), the diffusion rate parameter (D_D/r_0^2) was obtained (**Table 4-4**) by fitting the dual-mode kinetic model to the sorption kinetic data with and without dispersant (**Figure 4-3**). Considering a mean radius (r_0) of 457.5 μm , the diffusivity D_D was calculated to be 1.7×10^{-7} and 2.3×10^{-8} m^2/h for loamy sand and sandy loam, respectively, without dispersant. At 18 mg/L of the dispersant, D_D was escalated by 12% (to 1.9×10^{-7}) and by 35% (to 3.1×10^{-8} m^2/h) for loamy sand and sandy loam, respectively (The differences between the D_D values with and without dispersant are statistically significant with a p value of 0.01 and 0.0002, respectively, at the 0.05 level of significance). Evidently, the remarkable increment in the D_D value suggests that the sorbed dispersant offers not only greater

sorption affinity, but less mass transfer resistance. The dispersant-enhanced mass transfer rate of phenanthrene in SOM can be attributed to the partial softening or swelling of the more rigid SOM domains upon sorption of the dispersant (Jonker et al., 2003).

Table 4-3. Equilibrium sorption parameters for phenanthrene onto loamy sand and sandy loam sediments in the absence or presence of various concentrations of the dispersant. Errors are given as standard errors.

Sample	Corexit EC9500A (mg/L)	Dual-mode Isotherm Model		
		K_D (mL/g)	b (mL/ μ g)	Q (μ g/g)
Loamy Sand	0	42.1 \pm 8.6	4.6 \pm 1.4	16.2 \pm 6.5
	18	52.8 \pm 1.4	4.6 \pm 1.4	16.2 \pm 6.5
	180	190.6 \pm 2.7	4.6 \pm 1.4	16.2 \pm 6.5
Sandy Loam	0	312.4 \pm 27.3	26.7 \pm 2.3	10.2 \pm 8.2
	18	374.8 \pm 6.3	26.7 \pm 2.3	10.2 \pm 8.2
	180	1058.1 \pm 20.0	26.7 \pm 2.3	10.2 \pm 8.2

Table 4-4. The best-fitted values of phenanthrene diffusivities and the corresponding mean weighted square error (MWSE) in the absence or presence of the dispersant. Errors are given as standard errors.

Sample	Corexit EC9500A (mg/L)	D_D/r_0^2 (1/h)	D_D (m ² /h)	MWSE
Loamy Sand	0	0.8 \pm 0.010	(1.7 \pm 0.02) $\times 10^{-7}$	0.0008
	18	0.9 \pm 0.005	(1.9 \pm 0.01) $\times 10^{-7}$	0.0010
Sandy Loam	0	0.11 \pm 0.0005	(2.3 \pm 0.01) $\times 10^{-8}$	0.002
	18	0.15 \pm 0.00005	(3.1 \pm 0.001) $\times 10^{-8}$	0.001

4.3.4 Effects of dispersant on desorption kinetics of phenanthrene

Figures 4-4a and **b** show desorption kinetics of phenanthrene from loamy sand and sandy loam under scenarios (1) and (2). For both sediments, the kinetic profiles agreed with the commonly cited biphasic process: rapid initial (8 hours) desorption from more easily accessible

sites, followed by slow desorption due to slow diffusion in the micropores of SOM (Pavlostathis and Mathavan, 1992; Pignatello and Xing, 1995; Sahoo and Smith, 1997). Desorption equilibrium was reached in ~2 days, compared to ~4 hours for sorption equilibrium (**Figure 4-3**). At equilibrium, 29% of phenanthrene on loamy sand was desorbed, compared to 32% for sandy loam. The presence of the dispersant (18 mg/L) during desorption hindered phenanthrene desorption by 4% for loamy sand and 5% for sandy loam (p value <0.04 at the 0.05 level of significance). **Figures 4-4c** and **d** depict desorption kinetics of phenanthrene under scenarios (3) and (4). Again, the dispersant during desorption hindered phenanthrene desorption by 3% and 2% for loamy sand and sandy loam, respectively (p value <0.02 at the 0.05 level of significance). The underlying mechanisms for the inhibition are explained in Section 4.3.5 below.

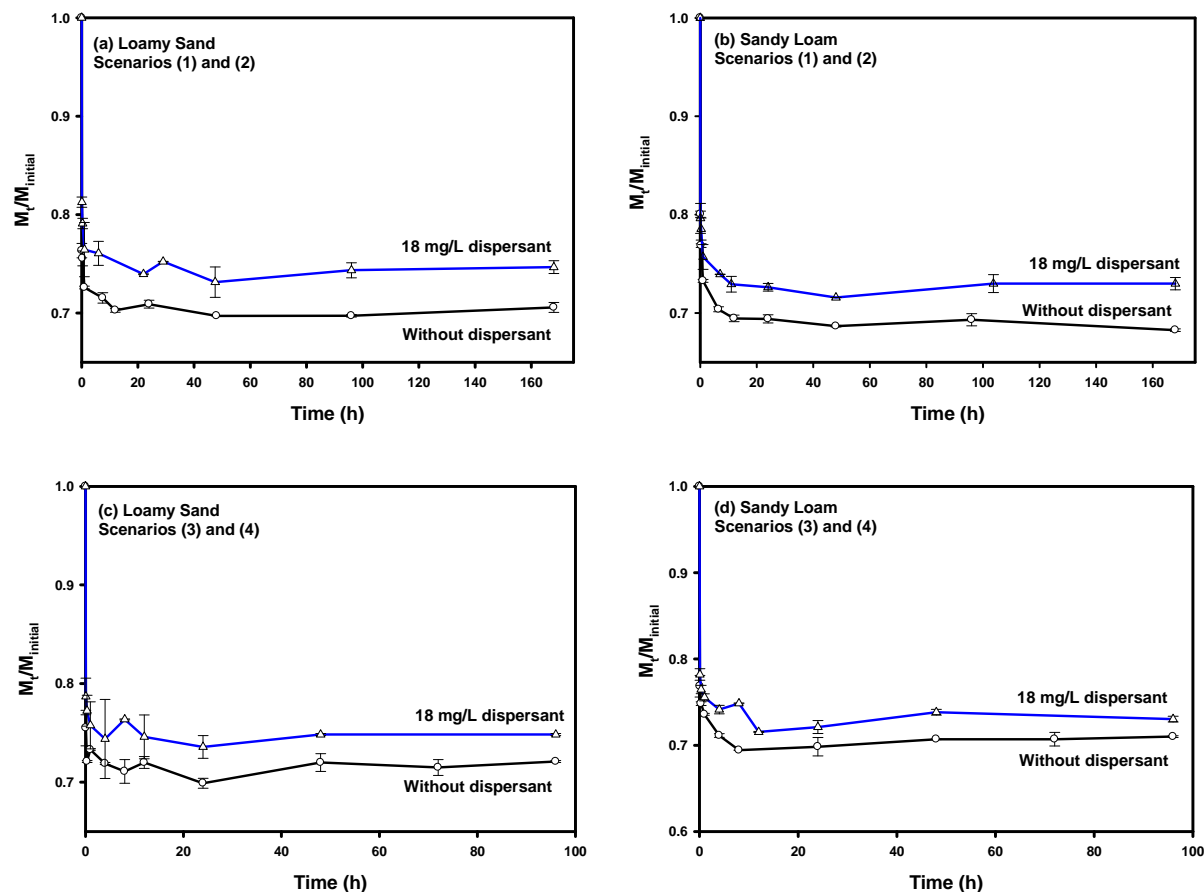


Figure 4-4. Desorption kinetics of phenanthrene from loamy sand and sandy loam sediments under four scenarios. Scenarios (1) and (2): Phenanthrene was pre-sorbed without dispersant, then subjected to desorption in the absence (1) or presence (2) of 18 mg/L of Corexit EC9500A. Scenarios (3) and (4): Phenanthrene was pre-sorbed with 18 mg/L of the dispersant present, then subjected to desorption in the absence (3) or presence (4) of 18 mg/L of Corexit EC9500A. Experimental conditions: loamy sand = 1.05 g, sandy loam = 0.21 g, solution volume = 42 mL, and pH = 7.3-7.5. M_t : phenanthrene mass sorbed at time t, $M_{initial}$: the initial phenanthrene mass in the sediments. Data are plotted as mean of duplicates, and error bars indicate standard error from the mean.

4.3.5 Effects of dispersant on sorption/desorption isotherms of phenanthrene

Figure 4-5 shows phenanthrene sorption isotherms by the sediments in the presence of 0, 18, and 180 mg/L of Corexit EC9500A, respectively. The results confirmed that increasing the dispersant concentration progressively increases phenanthrene uptake for both sediments. As illustrated in Section 4.3.3, the adsorption of the dispersant on the sediments adds a strong hydrophobic sink, resulting in the enhanced adsorption affinity and capacity for phenanthrene.

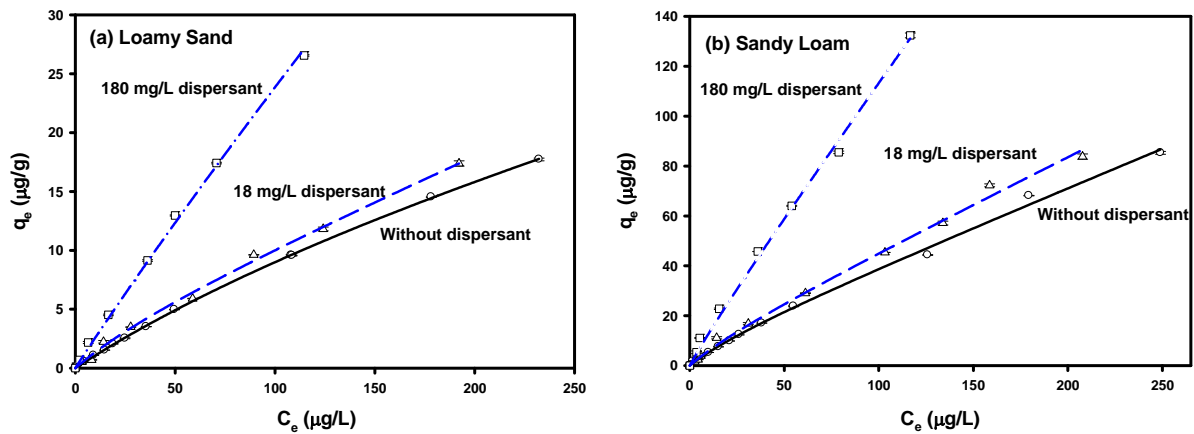


Figure 4-5. Effects of Corexit EC9500A on sorption isotherms of phenanthrene on (a) loamy sand and (b) sandy loam. Experimental conditions: loamy sand = 1.05 g, sandy loam = 0.21 g, initial phenanthrene concentration = 12-864 $\mu\text{g/L}$, solution volume = 42 mL, total dispersant = 0, 18 and 180 mg/L, pH = 6.8-7.7, and equilibrium time = 5 days. Symbols: experimental data, Lines: dual-mode equilibrium model fittings. Data are plotted as mean of duplicates, and error bars indicate standard error from the mean.

The dual-mode isotherm model (Eq. 4.1) was able to adequately simulate the isotherm data. Table 4-1 gives the best-fitted model parameters (K_D , b and Q). For loamy sand, K_D increased from 42.1 to 52.8, and 190.6 mL/g in the presence of 18 and 180 mg/L of the dispersant,

respectively. For sandy loam, K_D escalated from 312.4 to 374.8 and 1058.1 mL/g, respectively. Between the two sediments, sandy loam contains not only much higher SOM, but possesses nearly two times greater cation exchange capacity (CEC) (**Table 4-1**). As both SOM and CEC favor surfactant uptake (Wang and Keller, 2008), sandy loam offered much greater phenanthrene sorption capacity. The findings confirm that the sorbed dispersant added an additional domain of partitioning, resulting in enhanced phenanthrene uptake by the sediments.

Figure 4-6 shows desorption isotherms of phenanthrene from the two sediments under the four scenarios. Overall, phenanthrene sorption was fully reversible in the absence of the dispersant during desorption. The presence of the dispersant during sorption increased phenanthrene sorption capacity, but did not induce hysteresis. However, the presence of the dispersant (18 or 180 mg/L) during desorption caused remarkable sorption hysteresis and the extent of sorption irreversibility increases with increasing dispersant concentration. The dispersant-induced hysteresis is attributed to the elevated hydrophobicity and added sorption capacity/affinity due to sorption of the dispersant (Rodríguez-Cruz et al., 2005). Zhang and Zhu (2010) reported that Tween 80 at 852 mg/L desorbed 38% and 39%, respectively, less phenanthrene and pyrene from a PAH-contaminated soil than plain water.

It is noteworthy that micelles are likely formed at the 180 mg/L dispersant, which may compete with sediment-sorbed dispersant for phenanthrene. Section 4.3.6 provides details on the effects of the micelles.

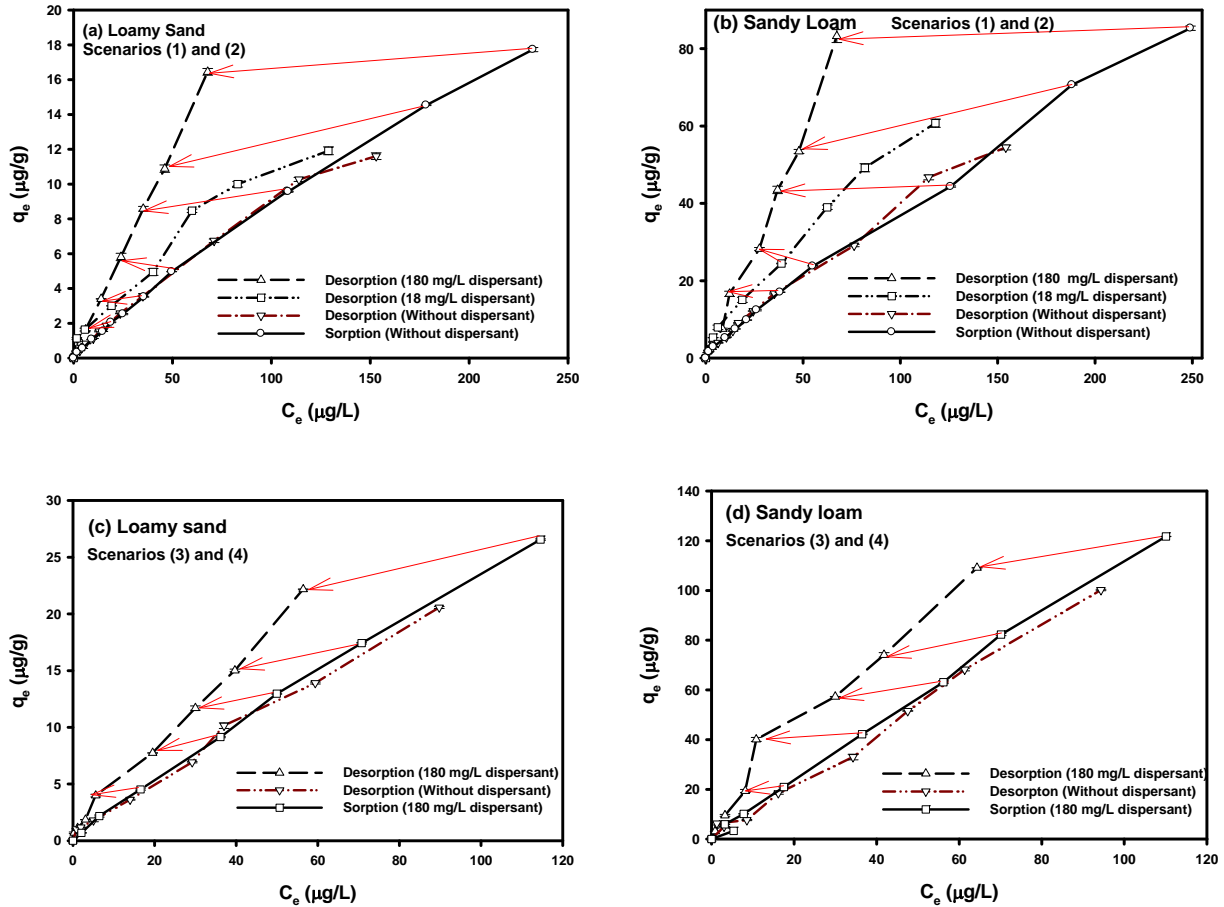


Figure 4-6. Effects of Corexit EC9500A on desorption hysteresis of phenanthrene on sediments under four scenarios. Lines with arrows indicate the corresponding points from the sorption isotherm to the desorption isotherm. Scenarios (1) and (2): Phenanthrene sorption was carried out without dispersant, but desorption with various initial concentrations of Corexit EC9500A (0, 18 or 180 mg/L). Scenarios (3) and (4): Phenanthrene sorption was carried out with 180 mg/L of dispersant, but desorption without or with 180 mg/L of Corexit EC9500A. Experimental conditions: loamy sand = 1.05 g, sandy loam = 0.21 g, initial phenanthrene = 12-864 µg/L, pH = 6.8-7.7, and solution volume = 42 mL. Data are plotted as mean of duplicates, and error bars indicate standard error from the mean.

4.3.6 Effects of dispersant dosage on phenanthrene uptake

Figure 4-7 shows equilibrium phenanthrene uptake by the sediments in the presence of various concentrations of the dispersant. For loamy sand, phenanthrene uptake increased nearly linearly from 15.8 to 21.8 $\mu\text{g/g}$ when the dispersant concentration increased from 0 to 230 mg/L. Further increase of the dispersant concentration to 860 mg/L resulted in a steady, though lesser, increase in phenanthrene sorption (24.7 $\mu\text{g/g}$). The increment in phenanthrene uptake concurs with the sorption isotherm of the dispersant (**Figure 4-2**), and is associated with elevated uptake of the dispersant on the sediments. Taken together that the dispersant can boost both water solubility (**Figure A-2**) and sediment uptake of phenanthrene, **Figure 4-7a** indicates that in the low dispersant concentration range (0-230 mg/L), the dispersant more favors sorption enhancement; in the higher concentration range (230-860 mg/L), the sorption enhancement is largely offset by the solubility enhancement.

It is noteworthy that the apparent CMC value (22.5 mg/L) was exceeded at the initial dispersant concentration of 86 mg/L and higher. Yet, the slope (proportionality) of the q_e versus dispersant dosage remained nearly the same over the concentration range of 0-230 mg/L (**Figure 4-7a**). This observation can be attributed to: 1) the surfactants of the dispersant were not equally sorbed by the sediment (e.g., Tween 85 is likely more preferably sorbed than the more soluble Tween 80 and SDSS), resulting an elevated CMC value; 2) micelles were not fully developed (i.e., only associates were formed); and/or 3) the number of the aqueous micelles was not enough to outweigh the sink effect of the sorbed surfactants. However, further increasing the dispersant concentration to above 230 mg/L diminished the percentage uptake of the dispersant, resulting in the reduced distribution coefficient (i.e., the smaller slope of the uptake curve) (**Figure 4-7a**).

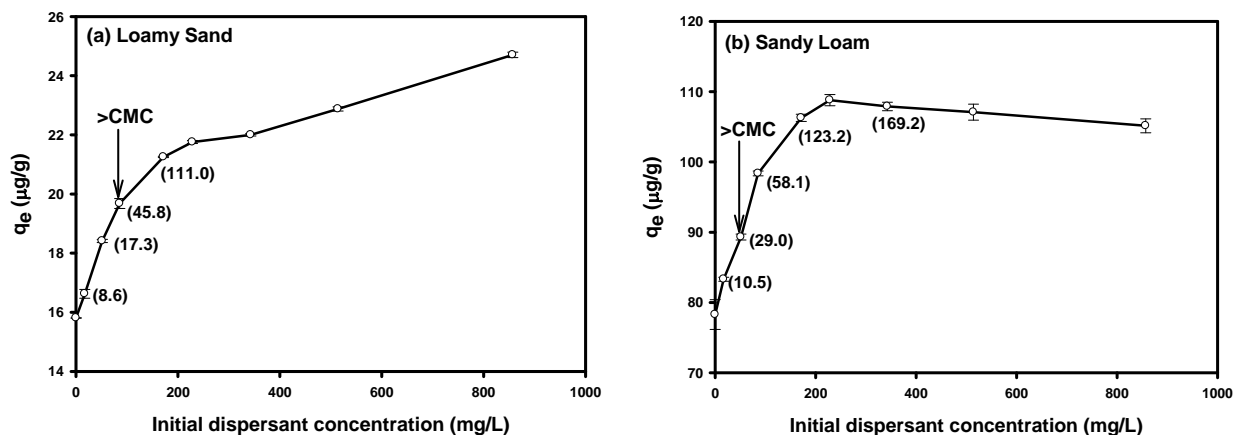


Figure 4-7. Phenanthrene uptake (q_e) by (a) loamy sand and (b) sandy loam sediments in the presence of various concentrations (0-860 mg/L) of Corexit EC9500A. Experimental conditions: loamy sand = 1.05 g, sandy loam = 0.21 g, initial phenanthrene = 600 $\mu\text{g/L}$, pH = 6.8-7.4, and solution volume = 42 mL. Numbers in brackets refer to the corresponding equilibrium dispersant concentration. Arrows indicate the points where the equilibrium concentration may exceed CMC. Data are plotted as mean of duplicates, and error bars indicate standard error from the mean.

For the sandy loam sediment, the effect of the dispersant on phenanthrene sorption was concentration-dependent. The dispersant displayed a sharp increase in phenanthrene sorption in the dispersant concentration range of 0-230 mg/L (**Figure 4-7b**). The uptake reached a maximum (108.8 $\mu\text{g/g}$) at a dispersant level of 230 mg/L followed by decreased uptake to 105.1 $\mu\text{g/g}$ when the dispersant was further increased to 860 mg/L. Again, the sharply enhanced phenanthrene uptake in the low dispersant concentration range is attributed to the dispersant being more favorably sorbed by the sediment. This is evident by comparing the magnitude of the two contrasting effects of the dispersant: increasing the dispersant concentration from 18 to 180 mg/L increases the solubility of phenanthrene by 2.4 times, but also increases the sediment uptake of the dispersant by 4.6 times. However, at elevated dispersant concentrations (343-860 mg/L), a

decreasing trend in phenanthrene uptake was observed. The decrease in phenanthrene uptake can be attributed to: 1) partial leaching of SOM from the sediment at elevated dispersant concentrations (though SOM leaching by seawater without dispersant was negligible), resulting in reduced sediment uptake of both phenanthrene and the dispersant; and 2) formation of micelles, causing more phenanthrene to partition in the solution.

4.3.7 Effects of aging on sorption isotherms of phenanthrene

Figure 4-8 shows that in the absence of the dispersant, the phenanthrene sorption capacity for both sediments slightly increased after 6 months of aging. The aging effect is attributed to mass transfer limitations through extremely narrow and tortuous paths and/or in condensed matrix structure of SOM (Pignatello and Xing, 1995). However, in the presence of the dispersant, the sorption capacity of phenanthrene slightly decreased after 6 months of aging, although the overall sorption capacity remained much higher than that without dispersant. The capacity drop is probably associated with dispersant-facilitated partial leaching of SOM, and partial dissolution of sorbed dispersant molecules resulting from, for example, dissolution of mineral cations (e.g., Ca^{2+}) from the sediments (Yang et al., 2006).

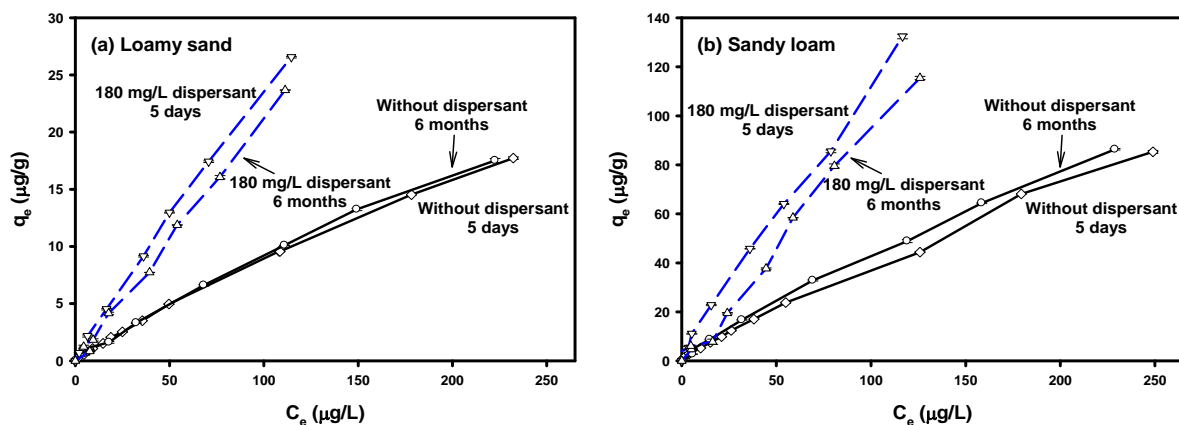


Figure 4-8. Effects of aging time on phenanthrene uptake (q_e) by (a) loamy sand and (b) sandy loam under various concentrations (0 and 180 mg/L) of Corexit EC9500A. Experimental

conditions: loamy sand = 1.05 g, sandy loam = 0.21 g, initial phenanthrene concentration = 12-864 $\mu\text{g/L}$, pH= 6.6-7.7, and contact time = 5 days to 6 months. Data are plotted as mean of duplicates, and error bars indicate standard error from the mean.

4.3.8 Effects of WAO and DWAO on sediment sorption of phenanthrene

Figure 4-9a shows that the equilibrium uptake of phenanthrene on loamy sand reached 67% without oil, 75% with WAO, and 89% with DWAO (p value <0.001 at the 0.05 level of significance). The presence of WAO/DWAO increased the K_d values from 81 mL/g for plain sediment to 120 mL/g with WAO and 324 mL/g with DWAO. Likewise, **Figure 4-9b** shows that WAO and DWAO increased the equilibrium phenanthrene uptake on sandy loam by 5% and 22%, respectively (p value <0.05 at the 0.05 level of significance); and the K_d values from 388 to 490 (with WAO) and 1467 mL/g (with DWAO).

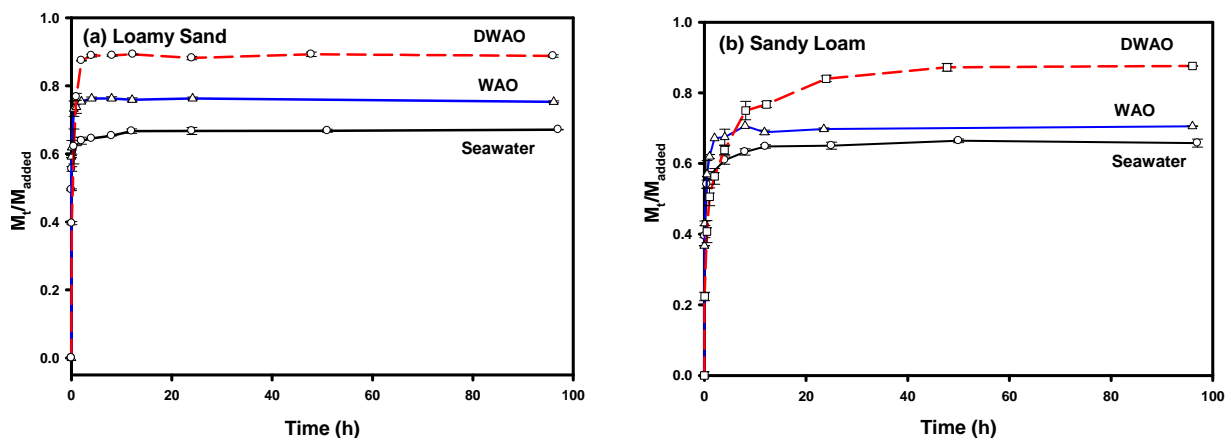


Figure 4-9. Effects of WAO and DWAO on sorption kinetics of phenanthrene onto (a) loamy sand and (b) sandy loam. Experimental conditions: loamy sand = 1.05 g, sandy loam = 0.21 g, initial phenanthrene = 600 $\mu\text{g/L}$, solution volume = 42 mL, and pH = 6.7-7.4. WAO was prepared at an oil-to-seawater volume ratio of 1:200, resulting in a WAO of 7.8 mg/L as TOC.

DWAO was prepared at a dispersant-to-oil-to-seawater volume ratio of 1:20:4000, resulting in a DWAO of 42 mg/L as TOC. M_t : phenanthrene mass uptake at time t , and M_{added} : total mass in the system. Data are plotted as mean of duplicates, and error bars indicate standard error from the mean.

Figure 4-10a shows the distribution of the hydrocarbons in WAO and DWAO based on the number of carbon atoms. The presence of the dispersant increased the fractions of C8-10, C12-16, C20, C21, and C26 hydrocarbons. **Figure 4-10b** presents the distribution of the hydrocarbons based on the type of the compounds, i.e., linear aliphatic hydrocarbons (LH), branched aliphatic hydrocarbons (BH), cyclic aliphatic hydrocarbons (CH), aromatic hydrocarbons (AH), and alkenes (A). The dispersant greatly increased the amounts of LH, BH, CH, AH, and alkenes. As would be expected, more hydrocarbons are found in the dissolved phase in the system with added dispersant. **Figure 4-11** shows hydrocarbon distributions of WAO and DWAO in the aqueous phase before and after sorption to the sediments. For WAO, the fractions C8-10, C13-14, C16-19, C21, and C26 were remarkably removed by both sediments (**Figures 4-11a** and **4-11e**). In terms of types of hydrocarbons, loamy sand removed 30% of LH, 38% of BH, 48% of AH, and 81% of alkenes (**Figure 4-11b**), whereas sandy loam removed 33%, 49%, 52%, and 65%, respectively (**Figure 4-11f**). Evidently, sorption of LH, BH, AH, and alkenes is responsible for enhanced phenanthrene uptake by the sediments in the presence of WAO.

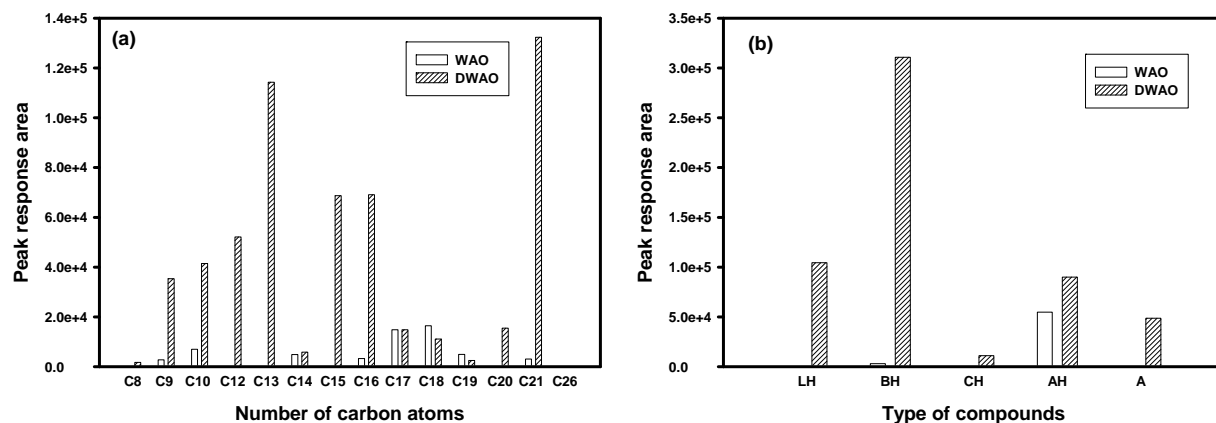
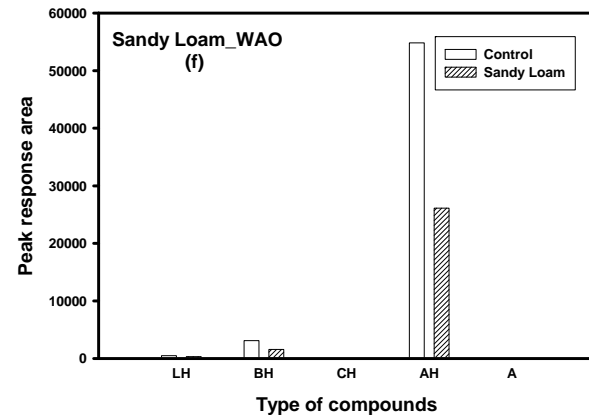
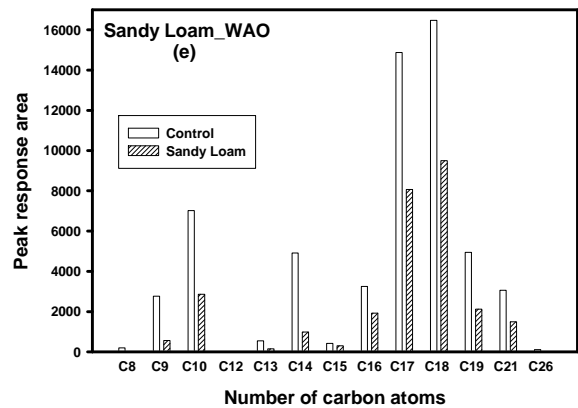
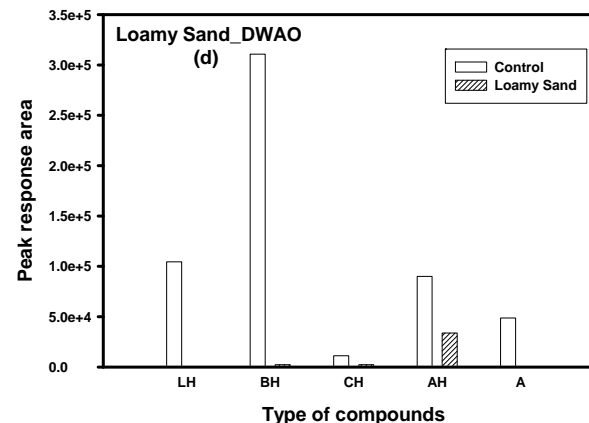
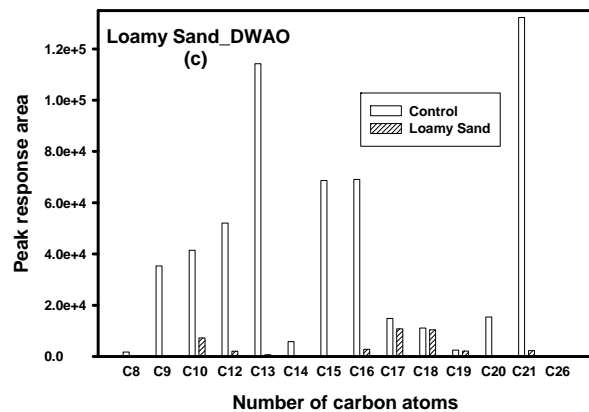
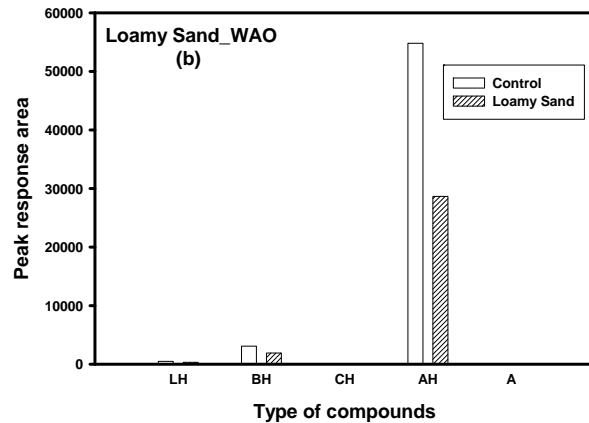
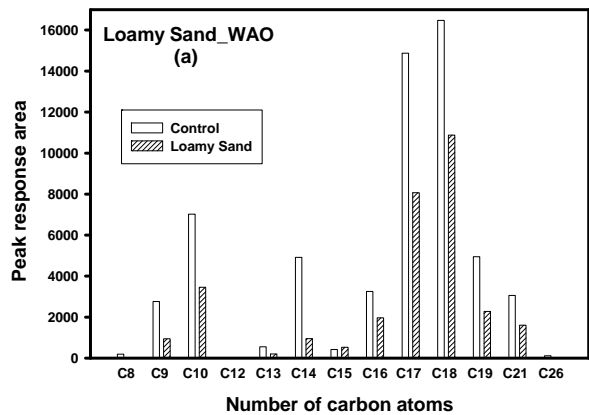


Figure 4-10. GC-MS analysis of WAO and DWAO as a function of the number of carbon atoms (a), and the type of chemical compounds (b). LH: linear aliphatic hydrocarbons; BH: branched aliphatic hydrocarbons; CH: cyclic aliphatic hydrocarbons; AH: aromatic hydrocarbons; and A: alkenes.

The presence of the dispersant enhanced sorption of all types of hydrocarbons. **Figures 4-11d** and **4-11h** reveal that both sediments removed nearly all of LH, BH, and alkenes, loamy sand removed 79% of CH and 63% of AH, and sandy loam removed 68% of CH and 59% of AH. Therefore, the further enhanced phenanthrene uptake is attributed to elevated uptake of LH, BH, AH, CH, and alkenes along with the dispersant in the presence of DWAO.



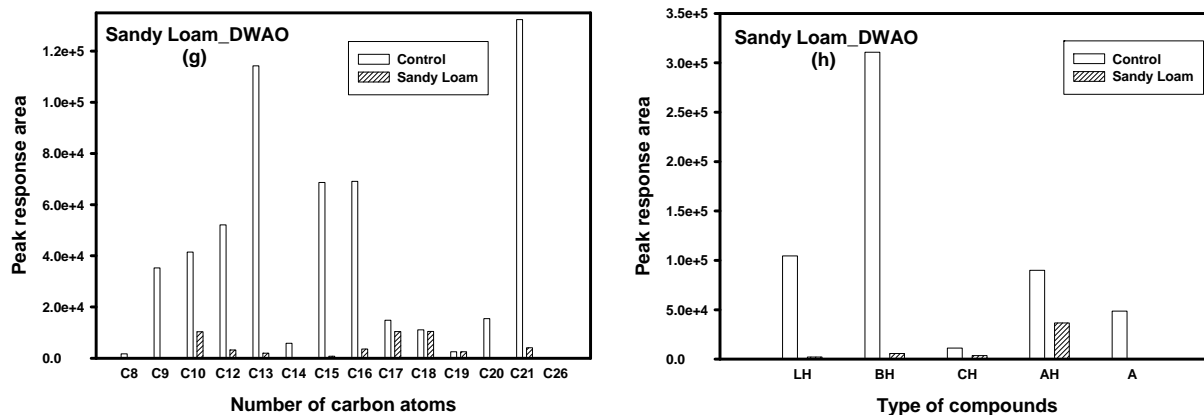


Figure 4-11. Hydrocarbon compositions of WAO and DWAO before and after sorption by loamy sand and sandy loam as a function of the number of carbon atoms or the type of chemical compounds. WAO and DWAO were prepared in the same manner as in Figure 4-10.

The WAO-facilitated phenanthrene sorption is attributed to the “plasticizing” effect of oil hydrocarbons on the structure and properties of SOM, i.e., the sorption of WAO may swell SOM and convert part of glassy SOM to a more rubbery polymer, making the hydrophobic interior sorption sites more accessible for phenanthrene (Jonker et al., 2003). In addition, the uptake of WAO renders the sediment surface more hydrophobic and affords additional sorption pools for phenanthrene. The presence of the dispersant further enhances the effect of WAO. On the one hand, the dispersant causes dispersion/dissolution of more oil hydrocarbons in the solution, which in turn results in transferring more hydrocarbons to the sediment/SOM phase. On the other hand, the sorption of dispersant onto sediments provides more sorption sites for oil hydrocarbons and PAHs, bestowing additional sorption capacity for phenanthrene.

4.4 Conclusions

This study investigated effects of oil and Corexit EC9500A on sorption and desorption of a model PAH with two representative Gulf Coast marine sediments. The primary findings are summarized as follows:

- (1) The dispersant poses two contrasting effects on the distribution of phenanthrene. On the one hand, it increases the aqueous solubility, which tends to reduce sediment sorption of the PAH; On the other hand, sediment sorption of the dispersant provides additional partitioning capacity for the PAH. Overall, increasing the concentration of the dispersant increases sediment uptake of the PAH.
- (2) The dispersant itself is subject to sorption to sediments with an S-shaped isotherm, likely indicative of transition from monomeric uptake in the low concentration region to formation of hemimicelles/admicelles at elevated concentrations. Yet, the sorption is fully reversible throughout the concentration range.
- (3) Batch sorption kinetic tests showed that the presence of the dispersant at 18 mg/L enhanced the sediment uptake of phenanthrene by up to 7%. The sorbed dispersant serves as a more effective sorbent for phenanthrene than native SOM with a 2.7-times greater distribution coefficient than K_{oc} .
- (4) Equilibrium sorption data reveal that the presence of the dispersant during sorption progressively increases phenanthrene sorption capacity for both sediments. The presence of the dispersant during desorption resulted in remarkable sorption hysteresis.
- (5) The dual-mode isotherm and kinetic models were able to adequately simulate phenanthrene sorption isotherms and kinetic data for both sediments in the presence of various concentrations of the dispersant.

(6) The presence of WAO and DWAO increases phenanthrene uptake of loamy sand by 8% and 22%, respectively, and that of sandy loam by 5% and 22%. The enhanced phenanthrene uptake by the sediments is attributed to elevated uptake of various classes of oil hydrocarbons such as LH, BH, AH, CH and alkenes along with the dispersant.

The results are important for understanding the roles of oil dispersants on environmental distribution, fate, and transport of spilled oil and persistent oil components in marine water-sediment systems.

Chapter 5. Effects of Oil Dispersant on Photodegradation of Pyrene in Gulf Coast Marine Water

This chapter studied effects and mechanisms of a model oil dispersant (Corexit EC9500A) on photodegradation of pyrene in the Gulf Coast seawater. The first-order kinetic model was used to simulate the degradation kinetic data. Effects of various environmental parameters, ionic strength (IS), humic acid (HA), pH, and temperature on the photodegradation of pyrene in the dispersant solution were also explored.

5.1 Introduction

The 2010 Deepwater Horizon (DWH) oil spill released an estimated 4.6 million barrels of South Louisiana sweet crude oil into the Gulf of Mexico (Griffiths, 2012). In response to the incident, approximately 2.1 million gallons of chemical dispersants Corexit EC9500A (1.8 million gallons) and Corexit 9527A (0.3 million gallons) were widely applied on the sea surface and at the wellhead (Kujawinski et al., 2011).

Polycyclic aromatic hydrocarbons (PAHs) are a class of important oil-associated contaminants that are of great environmental concern due to their potent toxicity, mutagenicity, carcinogenicity, and environmental persistency properties (Nam et al., 2008). The Macondo well oil contained approximated 3.9% of PAHs by weight, and as a result of the DWH oil spill, approximately 2.1×10^{10} g of PAHs was released into the Gulf of Mexico (Reddy et al., 2012). In the marine environment, PAHs undergo a number of physical and chemical processes, such as dissolution and volatilization (Liu et al., 2012), adsorption (Yang et al., 2005), bioaccumulation

(Baumard et al., 1998), biodegradation (Baumard et al., 1998), and photodegradation (Shemer and Linden, 2007). Volatilization and photodegradation are both important processes affecting the environmental fate and transport of PAHs. Since PAHs can strongly absorb light in the ultraviolet region, the associated photochemical reactions are considered the major abiotic mechanisms in degrading PAHs in the aquatic environment (Shemer and Linden, 2007).

Many studies have demonstrated that PAHs undergo fairly rapid transformations when exposed to ultraviolet light. Zhang et al. (2008) compared the photocatalytic degradation of benzo[a]pyrene on soil surfaces in the presence of TiO₂ using different wavelengths of UV irradiation (254, 310 and 365 nm). The results showed that the photodegradation followed the first-order kinetics, and the photodegradation rates followed the order of 254 nm ($7.8 \times 10^{-3} \text{ h}^{-1}$) > 310 nm (6.1×10^{-3}) > 365 nm ($5.0 \times 10^{-3} \text{ h}^{-1}$). Beltran et al. (1995) studied the direct photolysis under UV irradiation (254 nm) of three PAHs, fluorene, phenanthrene, and acenaphthene. They found that at pH 7 and 20 °C, the PAHs were completely degraded in 12, 7, and 20 mins, respectively. An and Carraway (2002) reported that the direct photolysis of phenanthrene and pyrene in water under 254 nm UV irradiation followed a first order rate law, with a half-life of 18 and 63 min, respectively.

Three primary mechanisms have been proposed for photodegradation of PAHs: (1) direct photoionization or photolysis; (2) energy transfer from an excited PAH triplet state to molecular oxygen; and (3) charge or electron transfer from an excited singlet or triplet PAH state to molecular oxygen (Fasnacht and Blough, 2002, 2003). Fasnacht and Blough (2003) examined the role of oxygen, photoionization, and PAH cation radicals in the photodegradation of nine PAHs, and concluded that photoionization was unimportant, and the photodegradation proceeded primarily through reaction of O₂ with both excited singlet and triplet states of the PAHs.

Dissolved organic matter (DOM)/humic acid (HA), ionic strength (IS), and pH have been reported to impact photodegradation of PAHs (Clark et al., 2007; Xia et al., 2009). DOM can influence photodegradation of PAHs in two contrasting ways: accelerating the degradation by stimulating the production of the highly reactive hydroxyl radicals or inhibiting the degradation due to the competition of the matrix components for absorption of the irradiation (Fasnacht and Blough, 2002; Xia et al., 2009). De Bruyn et al. (2012) demonstrated that the photodegradation rate of phenanthrene decreased by a factor of 5 in the presence of 10 mg/L of HA as TOC (Total Organic Carbon). In contrast, Fasnacht and Blough's (2002) observed that the photodegradation rate of anthracene increased by 70% in the presence of 5 mg/L as TOC of Suwannee River fulvic acid. Clark et al. (2007) reported that the photodegradation rate of pyrene decreased by 84% as dissolved oxygen concentration decreased from 8.6 to 0 mg/L, and increased by a factor of 2 as IS increased from 0.001 to 0.1 M.

Corexit EC9500A consists of three nonionic surfactants, namely, sorbitan monooleate (Span 80), sorbitan monooleate polyethoxylae (Tween 80), and sorbitan trioleate polyethoxylate (Tween 85), and an anionic surfactant (sodium dioctyl sulfosuccinate (SDSS)) (Scelfo and Tjeerdema, 1991). Researchers have investigated the effects of individual surfactants on the photochemical degradation of PAHs. An and Carraway (2002) observed enhanced pyrene photolysis and retarded phenanthrene photolysis in a micellar ammonium perfluorooctanoate (APFO) (50 mM) solution relative to water. Sigman et al. (1998) reported inhibited photodegradation of pyrene in Brij 35 micellar media, and observed that pyrene photolysis quantum yields was decreased by a factor of approximately 2 in the micellar media relative to that in water. However, to our knowledge, little is known on the effects of oil dispersants on the photodegradation kinetics, mechanisms, and pathways of PAHs. Moreover, the influences of

other factors such as IS, HA, pH, and temperature on PAHs degradation in the presence of oil dispersant have not yet been explored.

The overall goal of this study was to determine effects of a model oil dispersant Corexit EC9500A on the volatilization and photochemical degradation rates of pyrene in Gulf Coast seawater. The specific objectives were to: 1) investigate and predict effects of the dispersant on the volatilization rate of pyrene in seawater; 2) compare dispersant effects on photodegradation of pyrene under UV and sunlight irradiations; 3) elucidate mechanisms and pathways of pyrene photodegradation in the presence of the dispersant; and 4) examine effects of IS (or salinity), HA, pH, and temperature on photodegradation of pyrene in dispersant solution.

5.2 Materials and Methods

5.2.1 Materials

Seawater was collected from the top 30 cm of the water column from Grand Bay, AL, USA in December, 2010. The latitudes/longitudes of the sampling site were 30.37926/88.30684. The sampling site sits in the neighborhood with some sites affected by the DWH oil spill, such as Bayou La Batre and Dauphin Island. The seawater sample was stored in sealed containers at 4 °C in the refrigerator. Before use, the seawater was first passed through 0.45 µm membrane filters to remove suspended solids, and then sterilized at 121 °C for 35 min via autoclaving. Salient properties of the seawater sample have been described elsewhere (Gong et al., 2014).

All chemicals used in this study were of analytical or higher grade. Pyrene, 1,4-benzoquinone, tert-butanol, and methanol were purchased from Alfa Aesar (Ward Hill, MA, USA). Sodium azide (NaN₃), NaOH, and NaCl were obtained from Fisher Scientific (Fair Lawn, NJ, USA). Acetonitrile (HPLC grade) was purchased from EMD Millipore Corporation (Billerica, MA, USA). HCl was acquired from BDH Aristar (West Chester, PA, USA). Humic

acid (sodium salt, 50~60% as HA) was procured from Acros Organics (Morris Plains, NJ, USA). Corexit EC9500A was acquired through the courtesy of Nalco Company (Naperville, IL, USA).

5.2.2 Experimental apparatus

Batch photochemical degradation kinetic tests were carried out in a well controlled glass reactor with a surface area of 78 cm² and a volume of 650 mL. Two kinds of light sources were employed: (a) UV irradiation using a 4 W UV lamp operated at a wavelength of 253.7 nm; and (b) simulated sunlight using an Oriel Sol1A solar simulator (Newport Corporation, Irvine, CA, USA) with an additional air mass 1.5 global filter installed in the radiation beam to match the spectrum of the 450 W Xenon lamp to the typical solar spectrum. The light intensity was determined to be 7.7 and 257.7 W/m² for UV light and sunlight, respectively, by an optical power meter Model 1916-R (Newport Corporation, Irvine, CA, USA). To facilitate a sound comparison of the two light sources, the UV irradiation intensity was designed to be identical for both light sources although the solar simulator covers a broader spectrum of wavelengths whereas the UV light has a single wavelength of 253.7 nm. The light dose is also in accord with the actual solar irradiation (208 W/m²) in the Grand Bay area (NREL, 2013). **Figure 5-1** shows the schematic of the experimental set-up. Before each experiment, the lamps were warmed up for 15 min to ensure stable output. A quartz plate was used as the cover without blocking the light.

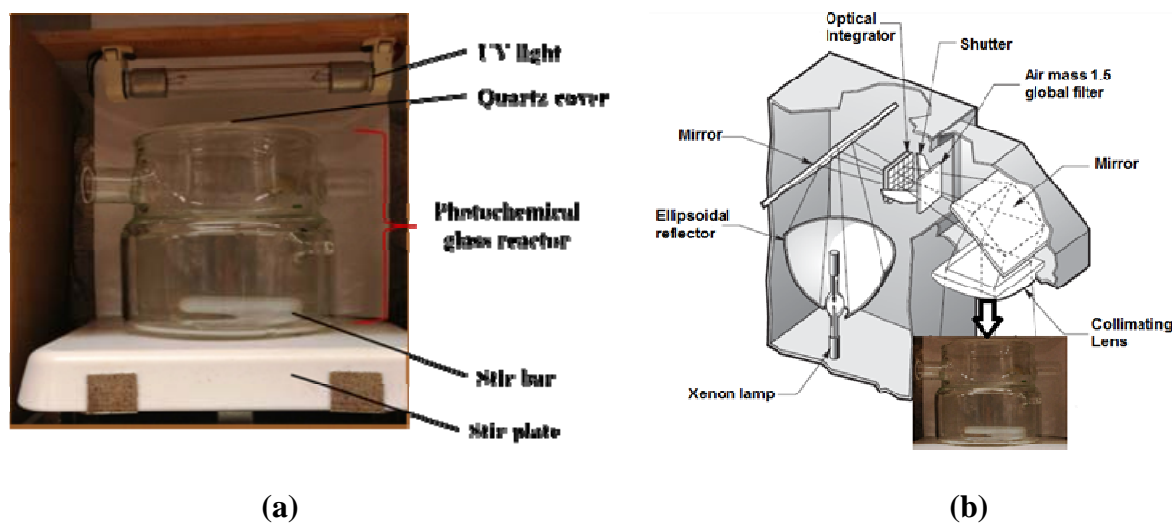


Figure 5-1. A schematic of the experimental set-up under (a) UV light, and (b) simulated sunlight.

5.2.3 Effects of dispersant on volatilization and photodegradation of pyrene

Batch kinetic tests were carried out with the reactor open to the atmosphere under UV irradiation. A stock solution of pyrene was prepared at 0.3 g/L in methanol. A working solution with a concentration of 60 $\mu\text{g/L}$ was then prepared by injecting 0.06 mL of the stock solution into 300 mL of seawater. In each batch, the reactor was filled with 300 mL of the solution and stirred gently with a magnetic stirrer bar to maintain homogeneity during the tests. Control tests were carried out in a closed system in the dark to assess the loss of pyrene due to sorption to the glass wall, which turned out to be negligible. To determine the volatilization rate of pyrene from the reactor system, parallel kinetic tests were carried out with the reactor in dark under otherwise identical conditions. To explore the net photodegradation rates, kinetic tests were conducted under UV or sunlight irradiation with the reactor sealed. During the batch tests, 1 mL each of the solution in the reactor was sampled at predetermined times and then analyzed for pyrene. To investigate the effects of the dispersant, the tests were conducted in the presence of 0, 18 and 180

mg/L of Corexit EC9500A under otherwise identical conditions. All the experiments were conducted in duplicate and at 22 ± 1 °C.

5.2.4 Effects of radical scavengers on UV-mediated photochemical degradation of pyrene

The formation of oxidative species, such as singlet oxygen ($^1\text{O}_2$), superoxide ($\text{O}_2^{\cdot-}$), and hydroxyl radicals ($\cdot\text{OH}$), and their roles in the pyrene degradation processes were investigated in the absence and presence of 18 mg/L of Corexit EC9500A. The following scavengers were used to quench these radicals, tert-butanol (221 mg/L) for hydroxyl radicals, sodium azide (NaN_3) (200 mg/L) for singlet oxygen and hydroxyl radicals, and 1,4-benzoquinone (161 mg/L) for superoxide radicals.

5.2.5 Photodegradation pathways of pyrene with or without dispersant

During the pyrene photodegradation process, samples (10 mL each) were collected from the reactor at various time intervals (0, 0.5, 2, and 6 h), and transferred into glass separating funnels. The intermediate products with or without the dispersant were then extracted using dichloromethane consecutively for three times (3 mL dichloromethane in each step). The extracts were then passed through a funnel with sodium sulfate anhydride (1 g), and concentrated to a volume of 0.1 mL under a stream of nitrogen gas for gas chromatography-mass spectrometry (GC-MS) analysis.

5.2.6 Effects of solution chemistry and temperature

The effects of IS, HA, pH, and temperature on photodegradation of pyrene were investigated through similar kinetic experiments in the presence of 18 mg/L of the dispersant. A 300 mL solution containing 60 $\mu\text{g/L}$ pyrene and the dispersant was prepared at the beginning of each batch experiment. To test the IS effect, the IS of the reaction solution was varied from 0.01, 0.7 to 1.2 M. The original seawater had an IS of 0.7 M, and NaCl was added in the seawater to

achieve an IS of 1.2 M, whereas DI water was added to dilute it down to 0.01 M. To examine the pH effect, the initial solution pH was adjusted to 5 and 8 using 0.1 M HCl, and the final pH dropped to 4.8 and 7.8, respectively. To probe the HA effect, the photochemical degradation tests were conducted in the presence of various HA concentrations (0, 5.5, and 22 mg/L as TOC). To investigate the temperature effect, the degradation experiments were carried out at 10 and 22 °C, which represent the lowest and highest water temperatures in the Grand Bay area.

5.2.7 Analytical methods

Pyrene concentration was determined using an HPLC system (HP series 1100, Hewlett Packard, CA, USA) equipped with a UV detector and a Zorbax SB-C18 column (150×468 mm). The mobile phase consists of 70% acetonitrile, 30% water, and 0.1% phosphoric acid. The injection volume was set at 80 µL, and the mobile phase flow rate was 1.0 mL/min. The optimal UV detection wavelength was found to be 240 nm for pyrene, and the method afforded a detection limit of 2.5 µg/L for pyrene. UV spectra of the aqueous solution were obtained using a UV spectrophotometer with a 1×1 cm quartz cell. Solution pH was measured with an Orion pH-meter equipped with a glass electrode (pH 510 Benchtip Meter, Oakton, CA, USA). HA concentrations were determined as TOC by a Tekmar Dohrmann Pheonix 8000 UV-Persulfate TOC analyzer (Mason, OH, USA) with a detection limit of 0.1 mg/L.

GC-MS analysis was carried out using an Agilent 7890A GC coupled with the 5975C series mass spectrometry (Agilent Technologies Inc., Santa Clara, CA, USA). A DB-EUPAH column (length = 20 m, inner diameter = 0.18 mm, film thickness = 0.14 µm) was used with helium as the carrier gas at a flow rate of 0.9 mL/min. A 2.0 µL sample was injected with 3 min solvent delay by an auto-injector. The front inlet temperature was set at 250 °C. The GC oven temperature was programmed as follows: 50 °C hold for 1 min, and ramped at 5 °C /min to

300 °C (held for 5 min). The scan range was from 50 to 550 m/z (mass to charge ratio). The chemical compounds were identified through high probability matching using the NIST11 MS library.

5.3 Results and Discussion

5.3.1 UV spectroscopic studies of pyrene in dispersant solutions

UV spectroscopy provides useful information on the solubilization characteristics of compounds in solutions (Riegelman et al., 1958). **Figure 5-2** shows the UV-Vis absorption spectra of pyrene in seawater and in the presence of various concentrations of Corexit EC9500A. The spectra in **Figure 5-2a** were corrected by subtracting the seawater background absorbance. It indicates that the presence of the dispersant enhances the total UV absorption of the solution, and increasing the dispersant concentration further enhances the absorption. **Figure 5-2b** compares the effects of the dispersant on the UV absorption of pyrene. To enunciate the absorbance of pyrene, the pyrene-in-seawater spectra were corrected by subtracting the seawater background absorbance, and when the dispersant was present, the spectra were corrected by subtracting the corresponding background dispersant-seawater absorbance. Two main phenomena were observed: First, the absorption spectra of pyrene in the dispersant solutions were very similar to that in seawater. Second, peaks in the dispersant solutions were generally lowered and red shifted compared to seawater. The former indicates that solubilized pyrene in the dispersant solutions is surrounded by a more water-like microenvironment. The critical micelle concentration (CMC) value of Corexit EC9500A is 22.5 mg/L (Gong et al., 2014). It is expected that at 180 mg/L of the dispersant, water penetrates into dispersant micelles and pyrene is solubilized in those regions of the dispersant micelles (An and Carraway, 2002). The latter indicates that pyrene in the dispersant solution is more polar than seawater (An and Carraway, 2002). **Figure 5-2b** shows

that the presence of the dispersant decreases the UV absorbance of pyrene at 254 nm, which suggests that the dispersant competes with pyrene for UV irradiation.

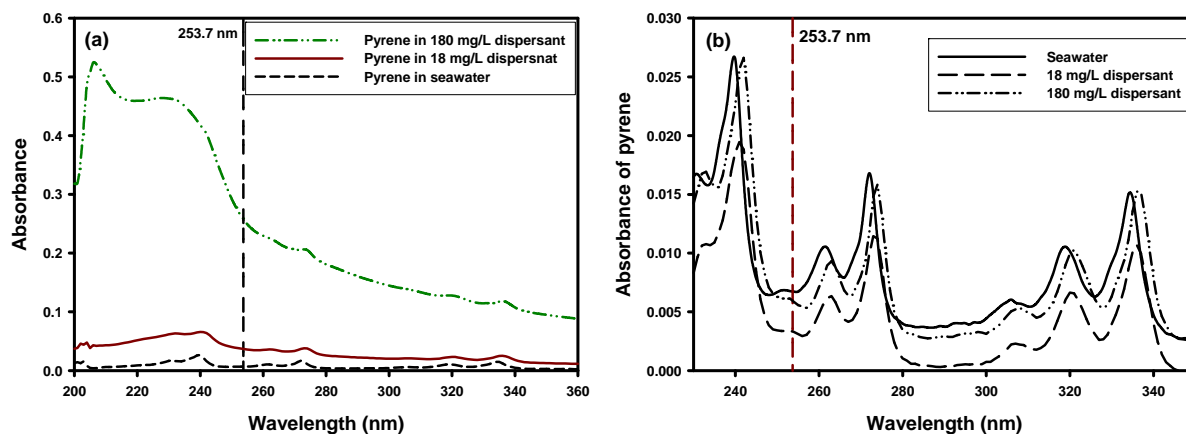


Figure 5-2. UV-Vis absorption spectra of pyrene in seawater and in a monomeric dispersant solution (18 mg/L) and micellar dispersant solution (180 mg/L). **(a)** The spectra were corrected by subtracting the seawater background absorbance. **(b)** The spectra in seawater were corrected by subtracting the seawater background absorbance, and the spectra in dispersant solutions were corrected by subtracting the background dispersant-seawater absorbance. Pyrene concentration = 60 $\mu\text{g/L}$.

5.3.2 Effects of dispersant on photodegradation of pyrene in seawater under UV and sunlight irradiations

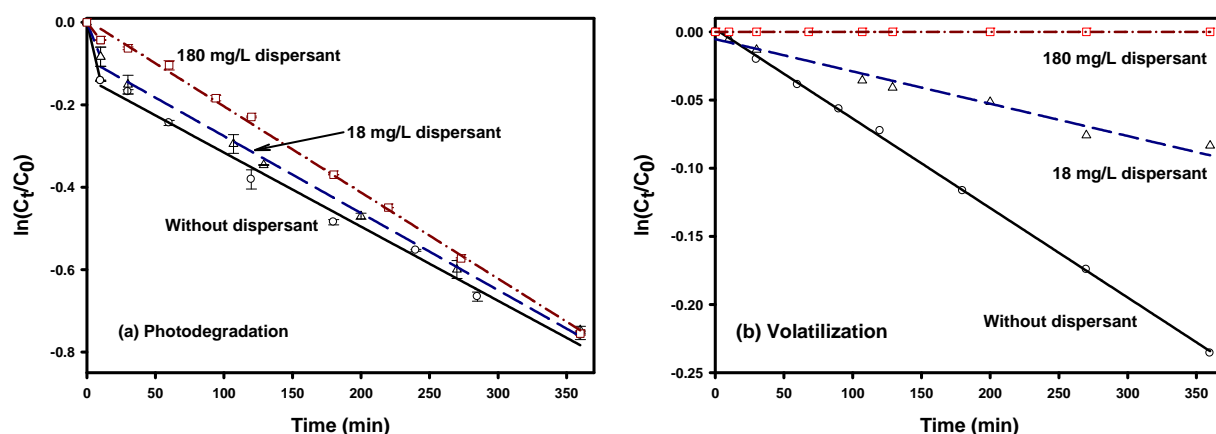
Direct photodegradation and photosensitized degradation of a trace chemical in well-mixed aqueous systems can be described by the first-order rate law (Kawaguchi, 1993; Zepp et al. 1981):

$$\ln(C_t / C_0) = -kt \quad (\text{Eq. 5.1})$$

where C_0 is the initial reactant concentration at irradiation time $t = 0$; C_t is the reactant

concentration at time t ; and k is the first-order rate constant. The k values under UV and sunlight were obtained by fitting Eqn. (1) to the corresponding experimental kinetic data.

Figure 5-3a displays an unusual two-stage kinetic profile under UV irradiation, i.e., a much faster degradation rate in the first 10 min (the induction period) followed by a slower but steady degradation rate thereafter. Accordingly, the first-order kinetic model was applied to the two stages separately to interpret the pyrene photodegradation rate data. **Table 5-1** gives the resultant kinetic parameters. The UV-degradation rate constant in stage 1 (k_1) was 0.0142 min^{-1} , which decreased to 0.0018 min^{-1} (by a factor of 7.9) in stage 2. Likewise, the rate constant for sunlight degradation in stage 1 was 10.7 times greater than in stage 2. The two-stage degradation kinetics suggests that different degradation mechanisms were operative in the two stages. During the induction period (0-10 min), direct photolysis played a more prevalent role in the pyrene degradation, resulting in a higher reaction rate. However, in the following stage (10-360 min), the electron transfer from excited pyrene species to oxygen became the rate-limiting mechanism, resulting in a slower reaction rate (see Section 5.3.5).



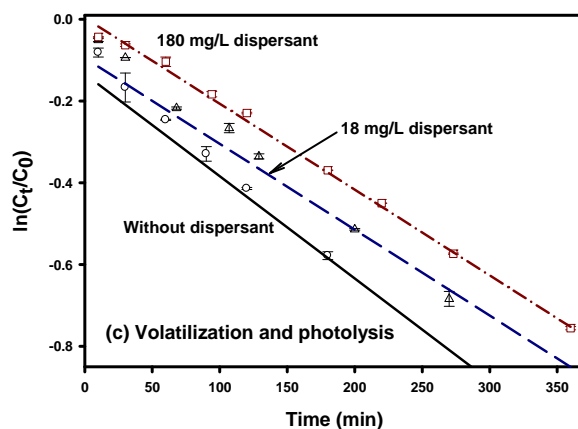


Figure 5-3. First-order kinetic plots of (a) photochemical degradation, (b) volatilization, and (c) combined volatilization and photodegradation of pyrene in seawater and in a monomeric dispersant Corexit EC9500A solution (18 mg/L) and micellar dispersant solution (180 mg/L). Initial pyrene = 60 $\mu\text{g/L}$, solution pH = 7.6-8.3, temperature = 22 $^{\circ}\text{C}$. Data plotted as mean of duplicates and the error bars (calculated as standard error) indicate data reproducibility.

Under UV irradiation, the presence of 18 mg/L of the dispersant inhibited k_1 from 0.0142 to 0.0083 min^{-1} (by 41.5%). The inhibition can be explained by the fact that the dispersant competed with pyrene for UV irradiation at 253.7 nm (**Figure 5-2**). The dispersant increased k_2 from 0.0018 to 0.0019 min^{-1} (by 5.6%) for UV and from 0.0006 to 0.0007 min^{-1} (by 17%) for sunlight. Based on the t-tests, the differences are statistically significant with a p value of <0.05 at the 0.05 level of significance. Section 5.3.6 presents more detailed discussion on the mechanisms for the dispersant enhanced degradation.

An effective photodegradation process requires that the emission spectra of the light source overlap with the absorption spectra of the target compounds (Mill et al., 1981). The higher pyrene degradation rate achieved under UV irradiation than that under simulated sunlight can be attributed to the more compatible emission spectra of the light source. In the subsequent tests,

UV light was used as the irradiation source.

Table 5-1. First-order photodegradation rate constants for pyrene photodegradation in the absence and presence of Corexit EC9500A under UV light and sunlight irradiations. Errors are given as standard error.

Corexit EC9500A (mg/L)	UV irradiation				Sunlight irradiation			
	0-10 min		10-360 min		0-10 min		10-360 min	
	k_1 (min ⁻¹)	R ²	k_2 (min ⁻¹)	R ²	k_1 (min ⁻¹)	R ²	k_2 (min ⁻¹)	R ²
0	$(1.42 \pm 0.01) \times 10^{-2}$	1	$(1.80 \pm 0.01) \times 10^{-3}$	0.991	$(7.50 \pm 0.44) \times 10^{-3}$	1	$(7.0 \pm 0.2) \times 10^{-4}$	0.930
18	$(8.30 \pm 0.02) \times 10^{-3}$	1	$(1.90 \pm 0.02) \times 10^{-3}$	0.996	$(9.50 \pm 1.10) \times 10^{-3}$	1	$(8.0 \pm 0.1) \times 10^{-4}$	0.973

Note: k_1 (min⁻¹): UV-degradation rate constant in stage 1; k_2 (min⁻¹): UV-degradation rate constant in stage 2; R^2 : the coefficient of determination, which is calculated via $R^2 = 1 - \frac{\sum_i (y_i - y_{i(predict)})^2}{\sum_i (y_i - \bar{y})^2}$, where y_i and $y_{i(predict)}$ are the original data values and model values, respectively, and \bar{y} is the mean of the observed data.

5.3.3 Effects of dispersant on volatilization and photodegradation of pyrene in seawater

Volatilization and photodegradation are both important processes affecting the fate and transport of oil components. Influences of various concentrations of Corexit EC9500A on pyrene volatilization and photochemical degradation were studied. **Figure 5-3b** shows that the volatilization rate of pyrene decreased with the increase of the dispersant concentration. Within 360 min, 21% of pyrene volatilized in the absence of the dispersant. The presence of the dispersant at 18 and 180 mg/L reduced the volatilization to 8% and 0, respectively. **Figure 5-3c** indicates that the combined volatilization and photodegradation rate of pyrene diminished with increasing dispersant concentration. The overall pyrene remaining in water increased from 33% without dispersant to 41% and 47% after 360 min with 18 and 180 mg/L of the dispersant, respectively.

Figures 5-3a and **5-3b** show that both photodegradation rate and volatilization rate from 10 to 360 min can be well interpreted by the first-order kinetic law, and **Table 5-2** gives the respective rate constants. The extent and rate of the photodegradation rate increased with increasing dispersant concentration. The first-order rate constant was 0.0018 min⁻¹ without the dispersant, and was escalated by 5.5% (to 0.0019 min⁻¹) and by 17% (to 0.0021 min⁻¹) in the presence of 18 and 180 mg/L of the dispersant, respectively (The differences between the *k* values with and without dispersant are statistically significant with a *p* value of 0.047 and 0.02, respectively, at the 0.05 level of significance). The presence of 18 and 180 mg/L of the dispersant reduced the volatilization rate constant from 0.0007 to 0.0002 and 0 min⁻¹, respectively, i.e., by 71% and 100%. Evidently, the presence of the dispersant lowered the Henry's law constant in favor of the dissolution of pyrene in the water column. Increasing the dispersant concentration from 0 to 18 and 180 mg/L enhanced the soluble pyrene by 9% and 22%, respectively.

Table 5-2. First-order rate constants for pyrene volatilization or/and UV-mediated photodegradation in the absence and presence of Corexit EC9500A. Errors are given as standard error.

Corexit EC9500A (mg/L)	Volatilization		UV-mediated Photodegradation (10-360 min)		Volatilization and photodegradation (<i>k_v</i> + <i>k</i>) (min ⁻¹)
	<i>k_v</i> (min ⁻¹)	R ²	<i>k</i> (min ⁻¹)	R ²	
0	(7.0±0.1)×10 ⁻⁴	0.999	(1.80±0.01)×10 ⁻³	0.991	0.0025
18	(2.0±0.2)×10 ⁻⁴	0.973	(1.90±0.02)×10 ⁻³	0.996	0.0021
180	0	0.999	(2.10±0.04)×10 ⁻³	0.997	0.0021

Note: *k_v* (min⁻¹): volatilization rate constant; R² is calculated in the same manner as noted in Table 5-1.

Based on the combined first-order rate constants for volatilization and photodegradation, the first-order kinetic model was able to adequately predict the experimental kinetic data that include both volatilization and photodegradation of pyrene in the presence of various concentrations of the dispersant (**Figure 5-3c**). It is noteworthy that the dispersant reduces pyrene volatilization but increases photodegradation. As a result, the overall pyrene degradation rate decreased from 0.0025 min^{-1} without the dispersant to 0.0021 min^{-1} for both 18 and 180 mg/L of the dispersant.

5.3.4 Role of radicals on photodegradation of pyrene

The UV irradiation is known to produce various reactive oxygen species, including singlet oxygen ($^1\text{O}_2$), superoxide ($\text{O}_2^{\cdot-}$), and hydroxyl radicals ($\cdot\text{OH}$) (Xu et al., 2008). Yet, the effects of oil dispersants on the production of the radicals are unknown. The role of each radical on the photodegradation of pyrene in the absence and presence of 18 mg/L of Corexit EC9500A was investigated using three selective radical scavengers (tert-butanol, sodium azide, and 1,4-benzoquinone). Tert-butanol selectively quenches $\cdot\text{OH}$, azide reacts with both $^1\text{O}_2$ and $\cdot\text{OH}$ (Xu et al., 2008), and 1,4-benzoquinone scavenges $\text{O}_2^{\cdot-}$ (Stylidi et al., 2004).

The addition of tert-butanol or NaN_3 in the solutions did not seem to affect the photodegradation rate of pyrene in the absence and presence of the dispersant (**Table 5-3**). This observation suggests that $\cdot\text{OH}$ and $^1\text{O}_2$ are not the main active species for the photodegradation of pyrene.

As shown in **Table 5-3**, when $\text{O}_2^{\cdot-}$ was quenched with 161 mg/L of 1,4-benzoquinone, the pyrene photodegradation rate decreased from 0.0018 to 0.0001 min^{-1} without dispersant and from 0.0019 to 0 min^{-1} with dispersant. This observation indicates that $\text{O}_2^{\cdot-}$ plays a predominant role in the pyrene photodegradation process. The first-order rate constant due to $\text{O}_2^{\cdot-}$ was 0.0017 min^{-1} without dispersant and 0.0019 min^{-1} with dispersant, and the contribution ratios of $\text{O}_2^{\cdot-}$ to the

overall photodegradation rate was 94% and 100%, respectively (**Table 5-3**). It is noteworthy that the presence of the dispersant boosted the $O_2^{\bullet-}$ generation, leading to the increase of the $O_2^{\bullet-}$ - facilitated photodegradation rate.

Table 5-3. Contributions of radicals ($\cdot\text{OH}$, $^1\text{O}_2$ and $\text{O}_2^{\cdot-}$) to pyrene photodegradation with or without 18 mg/L of Corexit EC9500A.

Errors are given as standard error.

Dispersant concentration (mg/L)	First-order rate constants (min^{-1})				$\cdot\text{OH}$ and $^1\text{O}_2$ contribution to pyrene photodegradation rate (min^{-1})	$\text{O}_2^{\cdot-}$ contribution to pyrene photodegradation rate (min^{-1})	$\text{O}_2^{\cdot-}$ contribution ratio to pyrene photodegradation rate
	k	k_{TB}	k_A	k_B			
0	$(1.80\pm 0.01)\times 10^{-3}$	$(1.80\pm 0.01)\times 10^{-3}$	$(1.80\pm 0.01)\times 10^{-3}$	$(1.0\pm 0.1)\times 10^{-4}$	0	0.0017	94%
18	$(1.90\pm 0.02)\times 10^{-3}$	$(1.90\pm 0.02)\times 10^{-3}$	$(1.90\pm 0.02)\times 10^{-3}$	$0\pm 1.1\times 10^{-5}$	0	0.0019	100%

Note: k_{TB} (min^{-1}): UV-degradation rate constant in the presence of tert-butanol (a $\cdot\text{OH}$ radical scavenger); k_A (min^{-1}): UV-degradation rate constant in the presence of azide ($\cdot\text{OH}$ and $^1\text{O}_2$ radicals scavenger); k_B (min^{-1}): UV-degradation rate constant in the presence of 1,4-benzoquinone ($\text{O}_2^{\cdot-}$ radical scavenger).

5.3.5 Photodegradation pathway of pyrene and effects of dispersant

Two possible mechanisms have been proposed for the oxidative photodegradation of pyrene in water: (1) electron transfer, and (2) singlet molecular oxygen addition (Sigman et al., 1998). As stated above, $O_2^{\cdot-}$ played a predominant role in the pyrene photodegradation process. Consequently, the oxidation of pyrene proceeds via electron transfer from an excited singlet and/or triplet state of pyrene to a molecular oxygen (Fasnacht and Blough, 2002).

The intermediate products with or without the dispersant were obtained by GC-MS spectroscopic methods. In both cases, one major by-product 1-hydroxypyrene was observed, as reported by others (Clark et al., 2007; Sigman et al., 1998; Wen et al., 2003). **Figure 5-4** provides the proposed primary reaction pathways leading to the photochemical oxidation of pyrene in seawater with or without the dispersant. Upon UV irradiation of the ground-state pyrene, excited-state pyrene (pyrene*) is formed, which may be quenched by O_2 to produce [Pyrene*-- O_2] complexes. The complexes are then excited, resulting in the formation of pyrene cation and $O_2^{\cdot-}$ radicals (Step 1). The water trapping step of the pyrene cations (Step 2) and the subsequent deprotonation (Step 3) give rise to hydroxypyrenyl radicals along with protons. Step 3 also depicts the acid-base equilibrium involving the hydroperoxyl radical. The pK_a of the hydroperoxyl radical was reported to be 4.4-4.8 (Sigman et al., 1998), and the radical is dissociated in our reaction systems (pH 7.6-8.3). The hydroxypyrenyl radical can be readily oxidized to give 1-hydroxypyrene (in Step 5), which is subject to further photochemical oxidation, resulting in the production of 1,6- and 1,8-pyrenquinones.

In the presence of the dispersant, more 1-hydroxypyrene was produced during the degradation process (**Figure 5-5**), indicating the dispersant enhanced photodegradation of pyrene.

The enhancement may result from an increased ability of the medium to support charge separation (Step 1 in **Figure 5-4**) (Sigman et al., 1998) and enhanced generation of $O_2^{\cdot-}$ radicals.

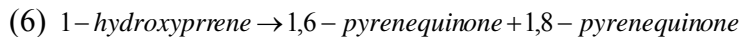
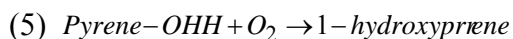
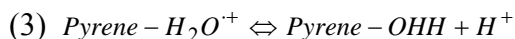
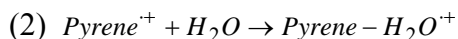
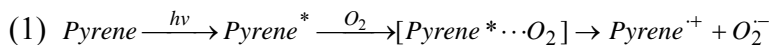


Figure 5-4. Photochemical degradation mechanism of pyrene in the aqueous solution (After Sigman et al., 1998).

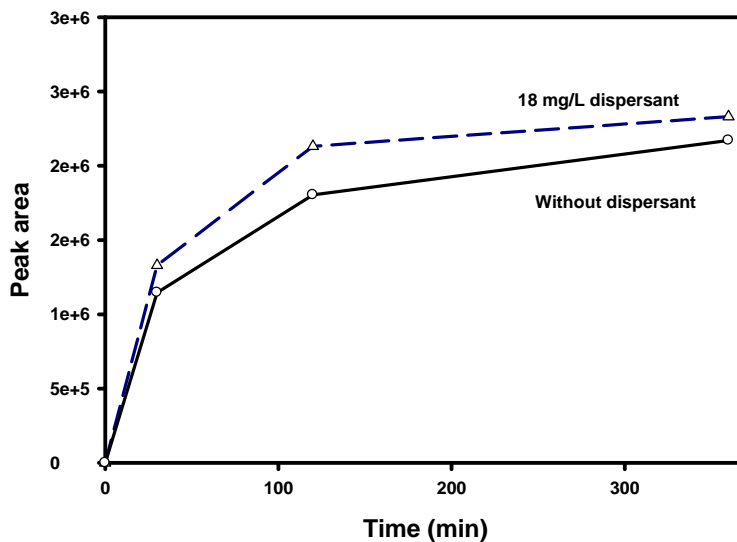


Figure 5-5. Peak areas of intermediate 1-hydroxypyrene during the photodegradation of pyrene in the presence and absence of Corexit EC9500A. Initial pyrene = 60 $\mu\text{g/L}$, initial dispersant = 18 mg/L, pH = 7.6-8.3, temperature = 22 $^{\circ}\text{C}$.

5.3.6 Dispersant effects on UV-facilitated pyrene photodegradation

The change of the photodegradation rate of pyrene associated with the oil dispersant can be calculated with the following formula (Xia et al., 2009):

$$dr = dA + dC + dO \quad (\text{Eq. 5.2})$$

where dr (min^{-1}) is the net change of photodegradation rate; dA , dC and dO (min^{-1}) are the changes of photodegradation rate caused by the active oxygen ($\text{O}_2^{\cdot-}$) mechanism, the photon and energy competition mechanism and other mechanisms, respectively.

The contribution of $\text{O}_2^{\cdot-}$ to pyrene photodegradation with and without dispersant was found to be 100% and 94%, respectively. The findings indicate that the presence of the dispersant generated more $\text{O}_2^{\cdot-}$ radicals. Based on the reaction rate constants in **Table 5-3**, the presence of 18 mg/L of the dispersant increases the rate constant due to the $\text{O}_2^{\cdot-}$ route ($k-k_B$) by 0.0002 min^{-1} . However, the actual net increase of the overall rate constant (k) was only by 0.0001 min^{-1} . The lower than expected rate enhancement can be attributed to the photon and energy competition effects of the dispersant, i.e., the presence of the dispersant in the solution also competes for the effective radiation energy with pyrene. As shown in **Figure 5-2b**, when dispersant was present in the solution, effective radiation for pyrene was weakened. In the presence of 18 mg/L of the dispersant, the fraction of absorbed light that was absorbed by pyrene was calculated to be only 0.11 (**Figure 5-2a**). Corexit EC9500A was found decomposed at least in part during the photodegradation process and many by-products derived from the dispersant components were observed, such as oleic acid, methyl oleate, and ethyl 2-ethylhexyl ester fumaric acid. Evidently, in the presence of 18 mg/L of the dispersant, the promoting effects of the $\text{O}_2^{\cdot-}$ radicals exceeded the inhibitive effects of the photon and energy competition, resulting in a net increase in the overall photodegradation rate.

When the dispersant concentration exceeds the CMC value (22.5 mg/L), the photodegradation is further enhanced due to the so-called “cage effect”, i.e., the accumulation of pyrene in the micelles results in a higher local concentration, leading to a faster degradation rate (Chu and Jia, 2009; Zhang et al., 2011). The resultant degradation intermediates tend to reside in the nonaqueous “cage” due to the similar hydrophobic properties. The incident photons can be effectively absorbed by the concentrated pyrene/intermediate molecules in the nonaqueous “cage”.

5.3.7 Effects of solution chemistry on photochemical degradation of pyrene in dispersant solution

To examine the effects of key environmental parameters in seawater, the photodegradation kinetics of pyrene in 18 mg/L of Corexit EC9500A were measured as a function of IS, HA, pH, and temperature. The first-order rate constants after 10 min were obtained through the linear regression $\ln(C_t/C_0)$ vs. t and are listed in **Table 5-4**.

Table 5-4. First-order rate constants for pyrene photodegradation in the presence of 18 mg/L of dispersant as a function of ionic strength (IS), humic acid (HA) concentration, pH, and temperature. Errors are given as standard error.

Initial pyrene concentration ($\mu\text{g/L}$)	Solution medium in 18 mg/L dispersant solution	k (min^{-1}) (10-360 min)	R^2	
60	IS (M)	0.01	$(1.70 \pm 0.04) \times 10^{-3}$	0.996
60		0.7	$(1.90 \pm 0.02) \times 10^{-3}$	0.996
60		1.2	$(2.20 \pm 0.10) \times 10^{-3}$	0.986
60	Humic acid (mg/L)	0	$(1.90 \pm 0.02) \times 10^{-3}$	0.996
60		5.5	$(0.70 \pm 0.04) \times 10^{-3}$	0.976
60		22.0	$(0.40 \pm 0.03) \times 10^{-3}$	0.964
60	pH	4.8	$(1.70 \pm 0.08) \times 10^{-3}$	0.990
60		7.8	$(1.90 \pm 0.02) \times 10^{-3}$	0.996
60	Temperature ($^{\circ}\text{C}$)	10	$(1.70 \pm 0.03) \times 10^{-3}$	0.998
60		22	$(1.90 \pm 0.02) \times 10^{-3}$	0.996

5.3.7.1 Effects of IS

Figure 5-6a shows effects of IS on photodegradation of pyrene in the dispersant solution. The first-order degradation rate increased from 0.0017 to 0.0019 min^{-1} as the IS increased from 0.01 to 0.7 M. Further increasing IS to 1.2 M boosted the reaction rate to 0.0022 min^{-1} . The differences between the k values are statistically significant with a p value of 0.046 (IS = 0.7 M) and 0.043 (IS = 1.2 M), respectively, at the 0.05 level of significance.

The solution property can affect electron transfer reaction rates by controlling the rate of diffusion and by establishing the microscopic environment of the solvent cage, within which the electron transfer between two species takes place (Clark and Hoffman, 1997). If a reaction is diffusion controlled, then increasing the IS should cause an increase in the rate constant for two ions of the same charge diffusing together; for oppositely charged ions, increasing IS would decrease the rate constant (Clark and Hoffman, 1997). Since the Step 3 is most likely the rate determining step (Clark et al., 2007), which involves a neutral species separating from a H^+ ion, the IS effect observed here is likely due to the solvent cage environment. When the IS is increased, some of the water molecules are attracted by the salt ions, resulting in a decrease in the number of molecules available to interact with pyrene and the dispersant. As a result, more ground-state pyrene can be irradiated by UV irradiation, forming excited-state pyrene.

5.3.7.2 Effects of HA

To test the effects of HA, experiments were repeated in 18 mg/L dispersant solution in the presence of various concentrations of HA (0, 5.5 and 22.0 mg/L measured as TOC) (**Figure 5-6b**). Note that the TOC concentration does not include those from the seawater and the dispersant. As the HA concentration increased from 0 to 5.5, and further to 22 mg/L, the first-

order rate constant decreased from 0.0019 to 0.0007, and further to 0.0004 min^{-1} , i.e., a 63% and 79% reduction, respectively.

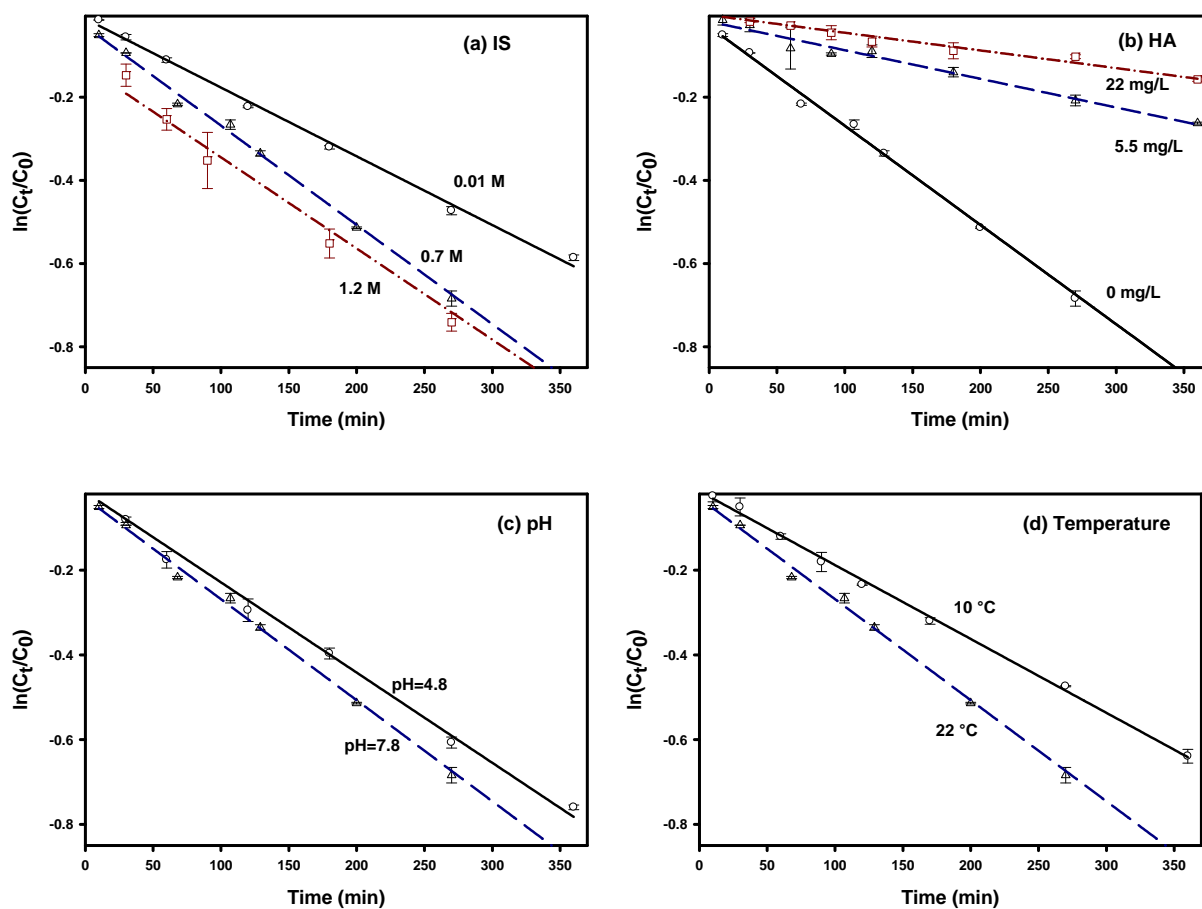


Figure 5-6. Effects of (a) IS, (b) HA, (c) pH, and (d) temperature on photodegradation of pyrene in 18 mg/L dispersant solution. Initial pyrene = 60 $\mu\text{g/L}$. Data plotted as mean of duplicates and the error bars (calculated as standard error) indicate data reproducibility.

HA can inhibit the photodegradation in a number of ways. First, HA competitively absorb the UV light. DOM is known to be the primary light absorbing species in natural water systems, with a well established absorption spectrum in the range of 200-450 nm (Boyle et al., 2009). Based on

the absorbance of pyrene and HA in the dispersant solution (**Figure 5-7**), HA optically filters the amount of light reaching pyrene, resulting in a reduced light intensity for pyrene. Second, HA may quench photo-chemically produced reactive species (Frimmel, 1994), i.e., the excited states of pyrene and the radical $O_2^{\cdot-}$. Lastly, sorption of pyrene within the complex HA matrix may shield it from oxygen and photodegradation. Previous sorption studies showed that pyrene could be rapidly and strongly adsorbed to HA (Simpson et al., 2004). HA have also been reported to act as a photosensitizer to induce the generation of radical species and advance PAHs degradation rates (Wangl et al., 1995). When HA absorbed UV irradiation, the reactive oxygen species were generated, therefore, pyrene bound to HA could potentially react with them due to their proximity to the sources (Fasnacht and Blough, 2002). The overall effect depends on the extent of these two contrasting factors. In our study, the restraining effects exceed the advancing effects, resulting in the overall decrease of pyrene photodegradation rates.

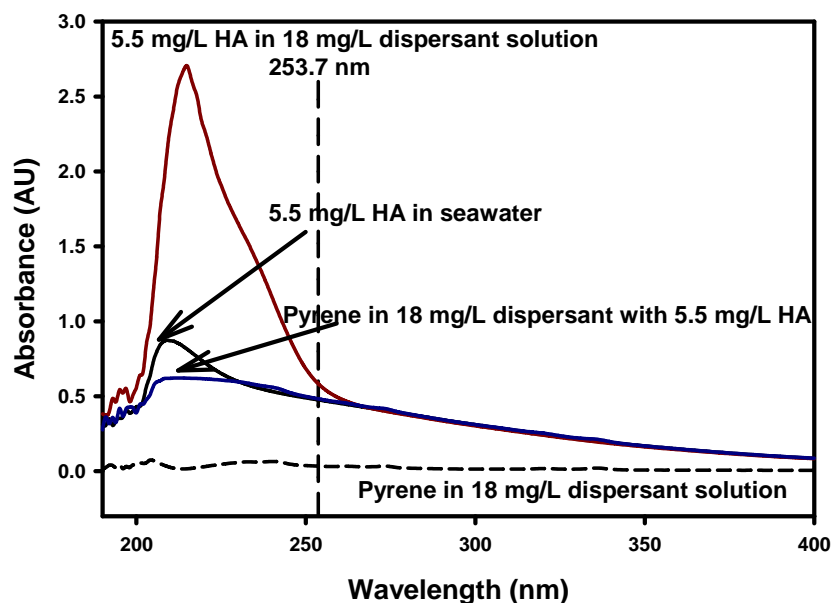


Figure 5-7. Absorption spectra of 5.5 mg/L HA and 60 μ g/L pyrene in 18 mg/L dispersant solution. The spectra were corrected by subtracting the seawater background absorbance.

5.3.7.3 Effects of pH and temperature

Figure 5-6c shows that decreasing pH from 7.8 to 4.8 did not significantly affect the photodegradation rate of pyrene in the dispersant solution (The difference between the k values was not statistically significant with a p value of 0.123). As discussed in Section 5.3.5, the pK_a of the hydroperoxyl radical is reported to be 4.4-4.8. The radical was highly dissociated at pH 4.8 and 7.8.

The influence of reaction temperature on the photodegradation rate of pyrene was also investigated in 18 mg/L dispersant solution at 10 and 22 °C (**Figure 5-6d**). The experimental results showed that decreasing the temperature decreased the first-order rate constant from 0.0019 to 0.0017 min^{-1} (with a p value of 0.037). An increase in temperature accelerates the movement rate of pyrene molecules, and the change in interatomic interaction weakens the chemical bonds. As a result, the degradation rate increased at higher temperature. However, the activation energy for the photolysis reaction is provided by light energy, not by systematic thermal energy. Therefore, the influence of temperature on the photolysis rate was limited (Li et al., 2013).

5.4 Conclusions

This study investigated effects of a popular oil dispersant Corexit EC9500A on evaporation and photochemical degradation of pyrene in the Gulf Coast seawater. The primary findings are summarized as follows:

- (1) Both UV and simulated sunlight irradiations can effectively degrade pyrene in dispersant solutions. Within 360 min, 53% of pyrene was degraded under UV irradiation, compared to 29% under solar irradiation in the presence of 18 mg/L of the dispersant. The degradation process followed a two-stage first-order kinetic model, i.e., a much faster initial degradation

rate in the first 10 min (an induction period) followed by a slower degradation rate thereafter (10-360 min). UV irradiation is more efficient than simulated sunlight in degrading pyrene in the aqueous phase.

- (2) The presence of the dispersant increases the aqueous solubility of pyrene, resulting in a reduction in pyrene volatilization loss. The presence of 18 and 180 mg/L of the dispersant reduced or eliminated pyrene volatilization.
- (3) The presence of the dispersant enhances UV-mediated photoreactivity of pyrene. With 0, 18 and 180 mg/L of the dispersant, the first-order rate constant was escalated from 0.0018 to 0.0019 min^{-1} and to 0.0021 min^{-1} , respectively.
- (4) Based on the individual volatilization and UV-mediated photodegradation rate constants, the first-order kinetic model is able to predict the combined volatilization and photodegradation of pyrene in the presence of various concentrations of the dispersant.
- (5) Mechanistic studies show that superoxide radicals play a predominant role and 1-hydroxypyrene is the main intermediate during the degradation process, indicating that pyrene oxidation proceeds through the electron transfer from excited pyrene to oxygen. The presence of the dispersant boosted the $\text{O}_2^{\cdot-}$ generation, and led to the increase in the pyrene photodegradation rate.
- (6) The first-order photodegradation rate of pyrene in 18 mg/L dispersant solution was enhanced by 29% when the IS was increased from 0.01 to 1.2 M, and decreased with increasing HA concentration (0.0019 min^{-1} without HA vs. 0.0007 min^{-1} with 5.5 mg/L HA vs. 0.0004 min^{-1} with 22 mg/L HA). When the temperature increased from 10 to 22 °C, the photodegradation rate was enhanced by 12%. The pH range of 4.8-7.8 had no significant effect on the degradation rate.

The results are important for understanding the roles of oil dispersants on environmental weathering and fate of spilled oil and persistent oil components.

Chapter 6. Conclusions and Suggestions for Future Research

6.1 Summary and Conclusions

Mercury (Hg) is one of the most pervasive and bio-accumulative metals in the environment. Fully stabilized iron sulfide (FeS) nanoparticles were prepared with sodium carboxymethyl cellulose (CMC) as a stabilizer and tested for removal of aqueous mercury (Hg^{2+}) as a function of CMC concentration, reaction time, pH, chloride, dissolved organic matter (DOM), and ionic strength. The presence of CMC at ≥ 0.03 wt% can fully stabilize 0.5 g/L of FeS (i.e. CMC-to-FeS molar ratio ≥ 0.0006) through concurrent electrostatic and steric stabilization mechanisms. Fourier transform infrared (FTIR) spectra suggested that CMC molecules were attached to the nanoparticles through bidentate bridging and hydrogen bonding. The particle stabilization technique increased mercury sorption capacity by 20% as CMC-to-FeS molar ratio increased from 0 to 0.0010. However, further increasing CMC-to-FeS ratio from 0.0010 to 0.0025 diminished mercury sorption by 14%. An examination of FTIR spectra of Hg-free and Hg-laden FeS indicates that surface complexation between CMC-FeS and Hg^{2+} is an important mechanism for Hg immobilization. On the other hand, XRD analysis showed that cinnabar, metacinnabar, and $\text{Hg}_{0.89}\text{Fe}_{0.11}\text{S}$ were formed during the sorption process, indicating that precipitation and ion exchange were concurrently operative. However, the relative contributions of adsorption (ion exchange and surface complexation) and precipitation were found to vary according to the Hg-to-FeS molar ratio. Batch kinetic data revealed that the stabilized nanoparticles facilitated rapid uptake of Hg^{2+} , with an equilibrium time within 6.7 h. The kinetic data can be interpreted with a

pseudo-second-order kinetic model. We proposed a dual-mode isotherm model, which considers precipitation and adsorption mechanisms, to interpret the sorption isotherm data. High mercury uptake was observed over the pH range of 6.5-10.5, whereas at pH<6 significant loss in mercury capacity was observed due to partial dissolution of the nanoparticles. Effect of chloride at <106 mg/L on Hg²⁺ sorption was negligible, while Hg²⁺ uptake decreased by 14% when chloride increased from 106 to 1775 mg/L. However, no further inhibitive effect was observed at higher Cl⁻ mg/L, suggesting the nanoparticles hold the potential for brine treatment. High concentrations of DOM (5 mg/L as TOC) may inhibit mercury uptake, while effect of ionic strength (0-0.2 M) was negligible. When aged for 2.5 years, 14% of sorbed Hg²⁺ was leached out of the nanoparticles due to pH drop. The leaching, however, can be prevented by maintaining pH above neutral. The findings in this work demonstrate the promise of CMC-stabilized FeS nanoparticles employed as an effective sorbent for *in situ* immobilization of mercury in contaminated soil/sediment and groundwater.

To prove this, *in situ* immobilization of mercury in some high profile field contaminated sediment/soils using CMC-stabilized FeS nanoparticles was investigated through a series of batch and column experiments. Batch tests showed that the nanoparticles are highly effective for immobilizing water-leachable or TCLP-leachable Hg in sediment/soils. For the Hg-loaded sediment (AL1), the nanoparticles reduced the water-leachable Hg by 96% and the TCLP leachability by 96% at an FeS-to-Hg molar ratio of 92:1. For the field contaminated soil (NJ38), the water-leachable Hg concentration was reduced by 90% and the TCLP leachability by 76% at an FeS-to-Hg molar ratio of 118:1. For the other field soil (NJ4), the water-leachable Hg concentration was reduced by 79% and the TCLP leachability by 26% at an FeS-to-Hg molar ratio of 28:1. In all cases, the nanoparticle treatment lowered the TCLP-leachable Hg to far

below the Land disposal restriction threshold of 25 µg/L. Column breakthrough tests indicated that the nanoparticles were deliverable in the sediment/soil columns under moderate injection pressure. The travel effective distance can be manipulated by regulating the injection pressure. However, once the external pressure was removed, the delivered nanoparticles remained virtually immobile under typical groundwater flow conditions. When the Hg-loaded sediment (AL1) was treated with 95 PVs of a 500 mg/L FeS nanoparticle suspension, the water-leachable Hg was reduced by 90%, and the TCLP leachability by 91%. The CMC-FeS nanoparticles showed a very high affinity for Hg. When the Hg-contaminated soil (NJ4) was treated with 52 PVs of a 500 mg/L FeS nanoparticle suspension, the water-leachable Hg was reduced by 93%, and the TCLP leachability by 65%. The results warrant further field demonstration of this promising *in situ* remediation technology.

Results obtained from the abovementioned study suggest that CMC-stabilized FeS nanoparticles are able to effectively immobilize Hg in water, soil, and sediments. The research provides promising evidence for this low-cost, effective, and innovative *in situ* remediation technologies. The nanoparticles may also be used for water treatment. However, the CMC-to-FeS ratio will need to be adjusted such that the resulting CMC-FeS nanoparticles, referred to as flocculated nanoparticles, can advantage of the high specific surface area and easy separation by gravity- settling (An et al., 2011).

During the 2010 DWH oil spill, ~2.1 million gallons of oil dispersants (mainly Corexit EC9500A and 9527A) were applied to the surface and wellhead to break up oil slicks. It remains unknown how the dispersants affect the environmental fate of PAHs in the Gulf Coast ecosystems. Effects of oil and an oil dispersant (Corexit EC9500A) on sorption and desorption of a model PAH (phenanthrene) were investigated with two representative Gulf Coast marine

sediments. Kinetic data revealed that the presence of the dispersant at 18 mg/L enhanced phenanthrene uptake by up to 7%, whereas the same dispersant during desorption reduced phenanthrene desorption by up to 5%. Sorption isotherms confirmed that at dispersant concentrations of 18 and 180 mg/L phenanthrene uptake progressively increased for both sediments. Furthermore, the presence of the dispersant during desorption induced remarkable sorption hysteresis. The effects were attributed to added phenanthrene affinity and capacity due to sorption of the dispersant on the sediments. The dual-mode isotherm and kinetic models adequately simulated sorption isotherms and kinetic data in the presence of various concentrations of the dispersant. Water accommodated oil (WAO) and dispersant-enhanced WAO increased phenanthrene sorption by up to 22%, which is attributed to elevated uptake of various classes of dissolved oil hydrocarbons along with the dispersant. This information is important for understanding the roles of oil dispersants on the distribution and transport of petroleum PAHs in marine water-sediment systems.

Effects of a model oil dispersant Corexit EC9500A on photodegradation of pyrene in the Gulf Coast seawater were investigated. Both UV and simulated sunlight irradiations can effectively degrade pyrene in dispersant solutions. Within 360 min, 53% of pyrene was degraded under UV irradiation, compared to 29% under solar irradiation in the presence of 18 mg/L of the dispersant. UV irradiation is more efficient than simulated sunlight in degrading pyrene in the aqueous phase. The presence of 18 and 180 mg/L of the dispersant increased the first-order photodegradation rate by 5.5% and 17%, respectively, within 360 min, and the dispersant also reduced or eliminated pyrene volatilization. By combining the individual first-order rate laws for volatilization and photodegradation, we proposed an integrated kinetic model that was able to adequately predict the overall degradation data. Mechanistic studies indicated that superoxide

radicals play a predominant role, and 1-hydroxypyrene was the main intermediate in the degradation process with and without the dispersant, suggesting that electrons are transferred from excited pyrene to oxygen. The dispersant enhanced the formation of the superoxide radicals, leading to the increase in the pyrene photodegradation rate. The first-order photodegradation rate of pyrene in 18 mg/L dispersant solution was enhanced by 29% when the IS was increased from 0.01 to 1.2 M, and decreased with increasing HA concentration (0.0019 min⁻¹ without HA vs. 0.0007 min⁻¹ with 5.5 mg/L HA vs. 0.0004 min⁻¹ with 22 mg/L HA). When the temperature increased from 10 to 22 °C, the photodegradation rate was enhanced by 12%. The pH range of 4.8-7.8 had no significant effect on the degradation rate. The results are important for understanding the roles of oil dispersants on environmental fate of spilled oil and persistent oil components.

The knowledge acquired in this part can help us better estimate long term fate and transport of persistent oil components spilled in the Gulf of Mexico, and provide various stakeholders, such as Gulf of Mexico Alliance, state and federal environmental agencies, industries and businesses affected by the spill, with a science based tool for risk assessment and decision making.

6.2 Suggestions for Future Work

The specific recommendations for future work were made as follows:

- (1) Field implementation and demonstration of CMC-stabilized FeS nanoparticles in mercury contaminated sites would be desired to validate the effectiveness of this *in situ* remediation technology. Field study can be carried out through *in situ* injection of the nanoparticles into a secondary source zone aquifer. Subsequently, the nanoparticles and mercury concentrations in groundwater can be monitored to evaluate the long term effectiveness of the stabilized

nanoparticles for immobilizing mercury *in situ*. The onsite practice would also help us spot any potential limitation in the procedures and methods.

- (2) Mercury methylation is of major environmental concern because methylmercury is the most toxic and bioaccumulation form of mercury. Our research has demonstrated in the laboratory that CMC-FeS can effectively immobilized Hg^{2+} in the water, soils, and sediments. Dissolved, neutral mercury complexes (primarily HgS^0 and $\text{Hg}(\text{HS})_2^0$ are considered the main mercury species controlling the extent of mercury methylation (Zhong et al., 2009). Therefore, it is of interest to estimate the effectiveness of the nanoparticles for stabilizing various forms of mercury, such as elemental mercury, mercuric ion, present in contaminated sites, and to evaluate the impacts of the FeS nanoparticles on mercury speciation.
- (3) In order to gain regulatory and public acceptance for using nanomaterials in environmental remediation, information on toxicology and fate of nanoparticles is needed. Transport, environmental fate, and environmental impacts of the nanoparticles are some interesting research areas. More experiments need to be conducted to investigate the transport behaviors of the nanoparticles under different conditions, i.e., various concentrations of the stabilizer, different concentrations of the nanoparticles, different injection pressure (or pore velocities), dissolved organic matter, and ionic strength.
- (4) The ultimate fate of the CMC-FeS nanoparticles as well as the stabilizer, the impact of the nanoparticles to the soil/sediment chemistry, such as pH and hydraulic conductivity, and to the subsurface microbial community after injection are interesting research topics that require future work.
- (5) Sorption and desorption behaviors of total petroleum hydrocarbons and various types of PAHs (such as pyrogenic PAHs or parent PAHs and alkylated PAHs), in the absence and

presence of different kinds of dispersants or surfactants can be carried out to acquire further insights into the roles of dispersant on the distribution and transport of spilled oil in the marine environment. To better simulate the real environmental conditions, lower concentrations of oil dispersants (less than 100 ppb) and/or PAHs might be used in the future study.

- (6) A series of photochemical degradation kinetic tests of oil/PAHs dissolved in the aqueous phase and sorbed in suspended sediments with and without the presence of low concentrations of dispersants can be studied under simulated Gulf Coast sunlight irradiation.

References

- Abbriano, R.M., Carranza, M.M., Hogle, S.L., Levin, R.A., Netburn, A.N., Seto, K.L., Snyder, S.M., Franks, P.J.S., 2011. Deepwater Horizon oil spill: A review of the planktonic response. *Oceanography* 24, 294-301.
- Ahn, C.K., Woo, S.H., Park, J.M., 2010. Selective adsorption of phenanthrene in nonionic-anionic surfactant mixtures using activated carbon. *Chemical Engineering Journal* 158, 115-119.
- An, B.; Liang, Q.; Zhao, D., 2011. Removal of arsenic (V) from spent ion exchange brine using a new class of starch-bridged magnetite nanoparticles. *Water Research* 45, 1961-1972.
- An, Y.J., Carraway, E.R., 2002. PAH degradation by UV/H₂O₂ in perfluorinated surfactant solutions. *Water Research* 36, 309-314.
- Andreozzi, R., Raffaele, M., Nicklas, P., 2003. Pharmaceuticals in STP effluents and their solar photodegradation in aquatic environment. *Chemosphere* 50, 1319-1330.
- Atwood, D.A., Zaman, M.K., 2006. Mercury removal from water, in: Atwood, D.A. (Ed.), *Recent developments in mercury science*. Springer-Verlag Berlin Heidelberg, pp. 163-182.
- Austin, A., 2012. Chemical characterization of a gold and mercury based siddha sastric preparation-*Poorna chandrodayam*. *American Journal of Drug Discovery and Development* 2 (3), 110-123.
- Axe, L., Anderson, P.R., 1995. Sr diffusion and reaction within Fe oxides: Evaluation of the rate-limiting mechanism for sorption. *Journal of Colloid and Interface Science* 175 (1), 157-165.

- Barnett, M.O., Turner, R.R., Singer, P.C., 2001. Oxidative dissolution of metacinnabar (beta-HgS) by dissolved oxygen. *Applied Geochemistry* 16(13), 1499-1512.
- Baumard, P., Budzinski, H., Garrigues, P., Sorbe, J.C., Burgeot, T., Bellocq, J., 1998. Concentrations of PAHs (polycyclic aromatic hydrocarbons) in various marine organisms in relation to those in sediments and to trophic level. *Marine Pollution Bulletin* 36, 951-960.
- Bayramoglu, G., Arica, M.Y., 2007. Kinetics of mercury ions removal from synthetic aqueous solutions using by novel magnetic p(GMA-MMA-EGDMA) beads. *Journal of Hazardous Materials* 144 (1-2), 449-457.
- Behra, P., Bonnissel-Gissing, P., Alnot, M., Revel, R., Ehrhardt, J.J., 2001. XPS and XAS study of the sorption of Hg(II) onto pyrite. *Langmuir* 17 (13), 3970-3979.
- Behrends, T., 1999. A three-site model for the adsorption of aromatic compounds in hemimicelles and admicelles. *Abstracts of Papers of the American Chemical Society* 217, U750-U750.
- Beltran, F.J., Ovejero, G., Garcia-Araya, J.F., Rivas, J., 1995. Oxidation of polynuclear aromatic hydrocarbons in water. 2. UV radiation and ozonation in the presence of UV radiation. *Industrial & Engineering Chemistry Research* 34, 1607-1615.
- Benoit, J.M., Gilmour, C.C., Mason, R.P., Heyes, A., 1999. Sulfide controls on mercury speciation and bioavailability to methylating bacteria in sediment pore waters. *Environmental Science & Technology* 33 (6), 951-957.
- Berner, R.A., 1964. Iron sulfides formed from aqueous solution at low temperatures and atmospheric pressure. *Journal of Geology* 72, 293-306.
- Blue, L.Y., Jana, P., Atwood, D.A., 2010. Aqueous mercury precipitation with the synthetic dithiolate, BDTH₂. *Fuel* 89 (6), 1326-1330.

- Borderieux, S., Wu, C., Bonzongo, J.C., Powers, K., 2004. Control of elemental mercury vapor in combustion systems using Fe₂O₃ nanoparticles. *Aerosol and Air Quality Research* 4(1), 74-90.
- Bouyoucos, G.J., 1962. Hydrometer method improved for making particle size analyses of soils. *Agronomy Journal* 54(5), 464-465.
- Bower, J., Savage, K. S., Weinman, B., Barnett, M.O., Hamilton, W.P., Harper, W.F., 2008. Immobilization of mercury by pyrite (FeS₂). *Environmental Pollution* 156 (2), 504–514.
- Boyle, E.S., Guerriero, N., Thiallet, A., Vecchio, R.D., Blough, N.V., 2009. Optical properties of humic substances and CDOM: Relation to structure. *Environmental Science & Technology* 43, 2262-2268.
- Braida, W.J., White, J.C., Ferrandino, F.J., Pignatello, J.J., 2001. Effect of solute concentration on sorption of polyaromatic hydrocarbons in soil: uptake rates. *Environmental Science & Technology* 35, 2765-2772.
- Brown, D.W., Floyd, A.J., Sainsbury, M., 1988. *Organic spectroscopy*. John Wiley & Sons., New York, USA.
- Brown, J.R., Bancroft, G.M., Fyee, W.S., McLean, R.A., 1979. Mercury removal from water by iron sulfide minerals-electron spectroscopy for chemical analysis (ESCA) study. *Environmental Science & Technology* 13, 1142-1144.
- Cheng, K.Y., Wong, J.W.C., 2006. Combined effect of nonionic surfactant Tween 80 and DOM on the behaviors of PAHs in soil-water system. *Chemosphere* 62, 1907-1916.
- Chiron, S., Minero, C., Vione, D., 2006. Photodegradation processes of the antiepileptic drug carbamazepine, relevant to estuarine waters. *Environmental Science & Technology* 40, 5977-5983.

- Chu, W., Jia, J., 2009. The photodegradation and modeling of a typical NAPL, trichloroethene, by monochromatic UV irradiations. *Environmental Science & Technology* 43, 1455-1459.
- Chu, W., Ma, C.W., 1998. Reaction kinetics of UV-decolourization for dye materials. *Chemosphere* 37, 961-974.
- Clark, C.D., De Bruyn, W.J., Ting, J., Scholle, W., 2007. Solution medium effects on the photochemical degradation of pyrene in water. *Journal of Photochemistry and Photobiology A: Chemistry* 186, 342-348.
- Clark, C.D., Hoffman, M.Z., 1997. Effect of solution medium on the rate constants of excited-state electron-transfer quenching reactions of ruthenium(II)-diimine photosensitizers. *Coordination Chemistry Reviews* 159, 359-373.
- D'Auria, M., Racioppi, R., Velluzzi, V., 2008. Photodegradation of crude oil: Liquid injection and headspace solid-phase microextraction for crude oil analysis by gas chromatography with mass spectrometer detector. *Journal of Chromatographic Science* 46, 339-344.
- Danwanichakul, P., Danwanichakul, D., 2009. Mass transfer analysis of mercury(II) removal from contaminated water by non-porous waste tire granules. *European Journal of Scientific Research* 36 (3), 363–375.
- Davies, B.E., 1974. Loss-on-ignition as an estimate of soil organic matter. *Soil Science Society of America Journal* 38(1), 150-151.
- De Bruyn, W.J., Clark, C.D., Ottelle, K., Aiona, P., 2012. Photochemical degradation of phenanthrene as a function of natural water variables modeling freshwater to marine environments. *Marine Pollution Bulletin* 64, 532-538.
- Fábrega, F.M., Mansur, M.B., 2007. Liquid-liquid extraction of mercury(II) from hydrochloric acid solutions by Aliquat 336. *Hydrometallurgy* 87 (3-4), 83–90.

- Fasnacht, M.P., Blough, N.V., 2002. Aqueous photodegradation of polycyclic aromatic hydrocarbons. *Environmental Science & Technology* 36, 4364-4369.
- Fasnacht, M.P., Blough, N.V., 2003. Mechanisms of the aqueous photodegradation of polycyclic aromatic hydrocarbons. *Environmental Science & Technology* 37, 5767-5772.
- Fitzgerald, W.F., Engstrom, D.R., Mason, R.P., Nater, E.A., 1998. The case for atmospheric mercury contamination in remote areas. *Environmental Science & Technology* 32, 1-7.
- Frimmel, F.H., 1994. Photochemical aspects related to humic substances. *Environment International* 20, 373-385.
- Gearing, P.J., Gearing, J.N., Pruell, R.J., Wade, T.L., Quinn, J.G., 1980. Partitioning of no. 2 fuel oil in controlled estuarine ecosystems. Sediments and suspended particulate matter. *Environmental Science & Technology* 14, 1129-1136.
- George-Ares, A., Clark, J.R., 2000. Aquatic toxicity of two Corexit dispersants. *Chemosphere* 40, 897-906.
- Ghodbane, I., Hamdaoui, O., 2008. Removal of mercury(II) from aqueous media using eucalyptus bark: Kinetic and equilibrium studies. *Journal of Hazardous materials* 160 (2-3), 301-309.
- Ghosh, A., Mukiibi, M., Ela, W., 2004. TCLP underestimates leaching of arsenic from solid residuals under landfill conditions. *Environmental Science & Technology* 38, 4677-4682.
- Gilmour, C.C., Henry, E.A., Mitchell, R., 1992. Sulfate stimulation of mercury methylation in freshwater sediments. *Environmental Science & Technology* 26, 2281-2287.
- Gong, Y., Liu, Y., Xiong, Z., Kaback, D., Zhao, D., 2012. Immobilization of mercury in field soil and sediment using carboxymethyl cellulose stabilized iron sulfide nanoparticles. *Nanotechnology* 23, 294007.

- Gong, Y., Liu, Y., Xiong, Z., Zhao, D., 2014. Immobilization of mercury by carboxymethyl cellulose stabilized iron sulfide nanoparticles: Reaction mechanisms and effects of stabilizer and water chemistry. *Environmental Science & Technology* (In Press).
- Gong, Y., Zhao, X., O'Reilly, S.E., Qian, T., Zhao, D., 2014. Effects of oil dispersant and oil on sorption and desorption of phenanthrene with Gulf Coast marine sediments. *Environmental Pollution* 185, 240-249.
- Graham, W.M., Condon, R.H., Carmichael, R.H., D'Ambra, I., Patterson, H.K., Linn, L.J., Jr, F.J.H., 2010. Oil carbon entered the coastal planktonic food web during the Deepwater Horizon oil spill. *Environmental Research Letters* 5, 045301.
- Griffiths, S.K., 2012. Oil release from Macondo Well MC252 following the Deepwater Horizon accident. *Environmental Science & Technology* 46, 5616-5622.
- He, F., Zhang, M., Qian, T., Zhao, D., 2009. Transport of carboxymethyl cellulose stabilizer iron nanoparticles in porous media: Column experiments and modeling. *Journal of Colloid and Interface Science* 334, 96-102.
- He, F., Zhao, D., 2005. Preparation and characterization of a new class of starch-stabilized bimetallic nanoparticles for degradation of chlorinated hydrocarbons in water. *Environmental Science & Technology* 39 (9), 3314–3320.
- He, F., Zhao, D., 2008. Hydrodechlorination of trichloroethene using stabilized Fe-Pd nanoparticles: Reaction mechanism and effects of stabilizers, catalysts and reaction conditions. *Applied Catalysis B: Environmental* 84 (3-4), 533–540.
- He, F., Zhao, D., Liu, J., Roberts, C.B., 2007. Stabilization of Fe-Pd nanoparticles with sodium carboxymethyl cellulose for enhanced transport and dechlorination of trichloroethylene in soil and groundwater. *Industry and Engineering Chemistry Research* 46 (1), 29–34.

- Hemmer, M.J., Barron, M.G., Greene, R.M., 2011. Comparative toxicity of eight oil dispersants, Louisiana sweet crude oil (LSC), and chemically dispersed LSC to two aquatic test species. *Environmental Toxicology and Chemistry* 30, 2244-2252.
- Ho, Y.S., McKay, G., 1999. Pseudo-second order model for sorption processes. *Process Biochemistry* 34, 451-465.
- Hogue, C., 2007. Quicksilver quandary: Mercury in aging chemical plants could end up in and on the hands of gold miners. *Chemical & Engineering News* 85, 26-29.
- Holmes, P., James, K.A.F., Levy, L.S., 2009. Is low-level environmental mercury exposure of concern to human health? *Science of the Total Environment* 408 (2), 171-182.
- Hyland, M. M., Jean, G. E., Bancroft, G. M., 1990. XPS and AES studies of Hg(II) sorption and desorption reactions on sulphide minerals. *Geochimica et Cosmochimica Acta* 54 (7), 1957-1967.
- Ishiwatari, R., 1971. Molecular weight distribution of humic acids from lake and marine sediments. *Geochemical Journal* 5, 121-132.
- Jean, G.E., Bancroft, G.M., 1986. Heavy metal adsorption by sulphide mineral surfaces. *Geochimica et Cosmochimica Acta* 50 (7), 1455–1463.
- Jeong, H.Y., Klaue, B., Blum, J.D., Hayes, K.F., 2007. Sorption of mercuric ion by synthetic nanocrystalline mackinawite (FeS). *Environmental Science & Technology* 41, 7699-7705.
- Johnson, A.C., Ternes, T., Williams, R.J., Sumpter, J.P., 2008. Assessing the concentrations of polar organic microcontaminants from point sources in the aquatic environment: Measure or model? *Environmental Science & Technology* 42, 5390-5399.

- Jonker, M.T.O., Sinke, A.J.C., Brils, J.M., Koelmans, A.A., 2003. Sorption of polycyclic aromatic hydrocarbons to oil contaminated sediment: Unresolved complex? *Environmental Science & Technology* 37, 5197-5203.
- Kawaguchi, H., 1993. Rates of sensitized photo-oxidation of 2,4,6-trimethylphenol by humic acid. *Chemosphere* 27, 2177-2182.
- Kecskes, L.J., Woodman, R.H., Trevino, S.F., Klotz, B.R., Hirsch, S.G., Gersten, B.L., 2003. Characterization of a nanosized iron powder by comparative methods. *KONA* 21, 143–150.
- Kerin, E.J., Gilmour, C.C., Roden, E., Suzuki, M.T., Coates, J.D., Mason, R.P., 2006. Mercury methylation by dissimilatory iron-reducing bacteria. *Applied and Environment Microbiology* 72, 7919-7921.
- Kirsten, W.J., 1979. Automated methods for the simultaneous determination of carbon, hydrogen, nitrogen, and sulfur, and sulfur alone in organic and inorganic materials. *Analytical Chemistry* 51, 1173-1179.
- Kirsten, W.J., 1979. Automated methods for the simultaneous determination of carbon, hydrogen, nitrogen, and sulfur, and sulfur alone in organic and inorganic materials. *Analytical Chemistry* 51, 1173-1179.
- Ko, S.O., Schlautman, M.A., Carraway, E.R., 1998a. Effects of solution chemistry on the partitioning of phenanthrene to sorbed surfactants. *Environmental Science & Technology* 32, 3542-3548.
- Ko, S.O., Schlautman, M.A., Carraway, E.R., 1998b. Partitioning of hydrophobic organic compounds to sorbed surfactants. 1. Experimental studies. *Environmental Science & Technology* 32, 2769-2775.

- Kot, F.S., Papoport, V. L., Kharitonova, G.V., 2007. Immobilization of soil mercury by colloidal sulphur in the laboratory experiment. *Central European Journal of Chemistry* 5, 846-857.
- Ku, Y., Wu, M., Shen, Y., 2002. Mercury removal from aqueous solutions by zinc cementation. *Waste Management* 22 (7), 721–726.
- Kujawinski, E.B., Kido Soule, M.C., Valentine, D.L., Boysen, A.K., Longnecker, K., Redmond, M.C., 2011. Fate of dispersants associated with the Deepwater Horizon oil spill. *Environmental Science & Technology* 45, 1298-1306.
- Li, Y., Duan, X., Li, X., Zhang, D., 2013. Photodegradation of nonylphenol by simulated sunlight. *Marine Pollution Bulletin* 66, 47-52.
- Lindqvist, Q., Rodhe, H., 1985. Atmospheric mercury: a review. *Tellus* 37B (3), 136–159.
- Liu, J., Huang, C., 1992. Electrokinetic characteristics of some metal sulfide-water interfaces. *Langmuir* 8, 1851-1856.
- Liu, J., Valsaraj, K.T., Devai, I., DeLaune, R.D., 2008. Immobilization of aqueous Hg(II) by mackinawite (FeS). *Journal of Hazardous Materials* 157 (2-3), 432-440.
- Liu, R., Zhao, D., 2007. Reducing leachability and bioaccessibility of lead in soils using a new class of stabilized iron phosphate nanoparticles. *Water Research* 41, 2491-2502.
- Liu, Z., Liu, J., Zhu, Q., Wu, W., 2012. The weathering of oil after the Deepwater Horizon oil spill: Insights from the chemical composition of the oil from the sea surface, salt marshes and sediments. *Environmental Research Letters* 7, 035302.
- Logan, B.E., 1999. *Environmental Transport Process*. John Wiley & Sons, Inc., Canada.
- Lu, L., Zhu, L.Z., 2012. Effect of soil components on the surfactant-enhanced soil sorption of PAHs. *Journal of Soils and Sediments* 12, 161-168.

- Lyons, W.B., Wayne, D.M., Warwick, J.J., Doyle, G.A., 1998. The Hg geochemistry of a geothermal stream, steamboat creek, Nevada: natural vs. anthropogenic influences. *Environmental Geology* 34 (2-3), 143–150.
- Maity, D., Agrawal, D.C., 2007. Synthesis of iron oxide nanoparticles under oxidizing environment and their stabilization in aqueous and non-aqueous media. *Journal of Magnetism and Magnetic Materials* 308 (1), 46–55.
- Mercone, D., Thomson, J., Croudace, I.W., Troelstra, S.R., 1999. A coupled natural immobilisation mechanism for mercury and selenium in deep-sea sediments. *Geochimica et Cosmochimica Acta* 63 (10), 1481-1488.
- Meyer, D.E., Sikdar, S.K., Hutson, N.D., Bhattacharyya, D., 2007. Examination of sulfur-functionalized, copper-doped iron nanoparticles for vapor-phase mercury capture in entrained-flow and fixed-bed systems. *Energy & Fuels* 21, 2688-2697.
- Mill, T., Mabey, W.R., Lan, B.Y., Baraze, A., 1981. Photolysis of polycyclic aromatic hydrocarbons in water. *Chemosphere* 10, 1281-1290.
- Mohan, D., Gupta, V.K., Srivastava, S.K., Chander, S., 2000. Kinetics of mercury adsorption from wastewater using activated carbon derived from fertilizer waste. *Colloids and Surfaces A: Physicochemical and Engineering Aspects* 177 (2-3), 169–181.
- Morse J. W., Arakaki T., 1993. Adsorption and coprecipitation of divalent metals with mackinawite (FeS). *Geochimica et Cosmochimica Acta* 57 (15), 3635–3640.
- Morse, J.W., Luther, G.W., 1999. Chemical influences on trace metalsulfide interactions in anoxic sediments. *Geochimica et Cosmochimica Acta* 63 (19-20), 3373–3378.
- Nakamoto, K., 1997. Infrared and Raman spectra of inorganic and coordination compounds, theory and applications in inorganic chemistry. John Wiley & Sons., New York, USA.

- Nam, J.J., Thomas, G.O., Jaward, F.M., Steinnes, E., Gustafsson, O., Jones, K.C., 2008. PAHs in background soils from Western Europe: Influence of atmospheric deposition and soil organic matter. *Chemosphere* 70, 1596-1602.
- Nam, K.H., Gomez-Salazar, S., Tavlarides, L.L., 2003. Mercury(II) adsorption from wastewaters using a thiol functional adsorbent. *Industrial & Engineering Chemistry Research* 42 (9), 1955–1964.
- National Research Council, 2003. Oil in the sea III: Inputs, fates, and effects. The National Academies Press, Washington, D.C. <<http://www.nap.edu/openbook.php?isbn=0309084385>> (accessed 07.11).
- National Research Council, 2005. Oil spill dispersants: efficacy and effects. The National Academies Press, Washington, D.C. <http://www.nap.edu/openbook.php?record_id=11283> (accessed 07.11).
- Neagu, V., Luca, C., Ștefan, S., Ștefan, M., Untea, I., 2007. Unconventional ion exchange resins and their retention properties for Hg²⁺ ions. *Reactive and Functional Polymers* 67 (12), 1433–1439.
- Pacheco, S., Medina, M., Valencia, F., Tapia, J., 2006. Removal of inorganic mercury from polluted water using structured nanoparticles. *Journal of Environmental Engineering* 132, 342-349.
- Pajares, A., Gianotti, J., Haggi, E., Stettler, G., Amat-Guerri, F., Bertolotti, S., Criado, S., García, N.A., 1999. Visible light-promoted interactions between riboflavin and 3-hydroxypyridine in aqueous solution. *Dyes and Pigments* 41, 233-239.

- Pan, G., Jia, C., Zhao, D., You, C., Chen, H., Jiang, G., 2009. Effect of cationic and anionic surfactants on the sorption and desorption of perfluorooctane sulfonate (PFOS) on natural sediments. *Environmental Pollution* 157, 325-330.
- Pan, G., Li, L., Zhao, D., 2010. Immobilization of non-point phosphorus using stabilized magnetite nanoparticles with enhanced transportability and reactivity in soils. *Environmental Pollution* 158, 35-40.
- Paquette, K., Helz, G., 1995. Solubility of cinnabar (red HgS) and implications for mercury speciation in sulfidic waters. *Water, air, and soil pollution* 80 (1-4), 1053–1056.
- Park, J.W., Jaffe, P.R., 1993. Partitioning of three nonionic organic compounds between adsorbed surfactants, micelles, and water. *Environmental Science & Technology* 27, 2559-2565.
- Parkpoin, P., Thongra-ar, W., DeLaune, R.D., Jugsujinda, A., 2001. Adsorption and desorption of mercury by Bangpakong River sediments as influenced by salinities. *Journal of Environmental Science and Health, Part A: Toxic/Hazardous Substance and Environmental Engineering* 36(5), 623-640.
- Pavlostathis, S.G., Mathavan, G.N., 1992. Desorption kinetics of selected volatile organic compounds from field contaminated soils. *Environmental Science & Technology* 26, 532-538.
- Payne, J.R., Clayton Jr, J.R., Kirstein, B.E., 2003. Oil/suspended particulate material interactions and sedimentation. *Spill Science & Technology Bulletin* 8, 201-221.
- Piao, H., Bishop, P.L., 2006. Stabilization of mercury-containing wastes using sulfide. *Environmental Pollution* 139, 498-506.

- Pignatello, J.J., 1998. Soil organic matter as a nanoporous sorbent of organic pollutants. *Advances in Colloid and Interface Science* 76-77, 445-467.
- Pignatello, J.J., Xing, B., 1995. Mechanisms of slow sorption of organic chemicals to natural particles. *Environmental Science & Technology* 30, 1-11.
- Pitoniak, E., Wu, C., Mazyck, D.W., Powers, K.W., Sigmund, W., 2005. Adsorption enhancement mechanisms of silica-titania nanocomposites for elemental mercury vapor removal. *Environmental Science & Technology* 39, 1269-1274.
- Ramachandran, S.D., Hodson, P.V., Khan, C.W., Lee, K., 2004. Oil dispersant increases PAH uptake by fish exposed to crude oil. *Ecotoxicology and Environmental Safety* 59, 300-308.
- Ravichandran, M., Aiken, G.R., Ryan, J.N., Reddy, M.M., 1999. Inhibition of precipitation and aggregation of metacinnabar (mercuric sulfide) by dissolved organic matter isolated from the Florida Everglades. *Environmental Science & Technology* 33 (9), 1418-1423.
- Reddy, C.M., Arey, J.S., Seewald, J.S., Sylva, S.P., Lemkau, K.L., Nelson, R.K., Carmichael, C.A., McIntyre, C.P., Fenwick, J., Ventura, G.T., Van Mooy, B.A.S., Camilli, R., 2012. Science applications in the Deepwater Horizon oil spill special feature: Composition and fate of gas and oil released to the water column during the Deepwater Horizon oil spill. *Proceedings of the National Academy of Sciences of the United States of America*, 1101242108.
- Reference Soil Test Methods for the Southern Region of the United States, Southern Cooperative Series Bulletin 289, 1983. University of Georgia College of Agriculture Experiment Stations, Athens, GA, 30602.
- Reimers, R.S., Krenkel, P.A., 1974. Kinetics of mercury adsorption and desorption in sediments. *Water Pollution Control Federation* 46, 352-365.

- Rickard, D., Morse, J.W. 2005. Acid volatile sulfide (AVS). *Marine Chemistry* 97(3-4), 141-197.
- Rickard, D., Schoonen M.A.A., Luther, G.W., 1995. Chemistry of iron sulfides in sedimentary environments, in Vairavamurthy, M.A. et al. (Ed.), *Geochemical transformations of sedimentary sulfur*, pp. 168-193. American Chemical Society.
- Rickard, D.T., 1974. Kinetics and mechanism of the sulfidation of goethite. *American Journal of Science* 274, 941-952.
- Riegelman, S., Allawala, N.A., Hrenoff, M.K., Strait, L.A., 1958. The ultraviolet absorption spectrum as a criterion of the type of solubilization. *Journal of Colloid Science* 13, 208-217.
- Rodríguez-Cruz, M.S., Sanchez-Martin, M.J., Sanchez-Camazano, M., 2005. A comparative study of adsorption of an anionic and a non-ionic surfactant by soils based on physicochemical and mineralogical properties of soils. *Chemosphere* 61, 56-64.
- Ross, S.D., 1972. *Inorganic infrared and Raman spectra*. McGraw Hill Ltd., UK.
- Saeed, T., Ali, L.N., Al-Bloushi, A., Al-Hashash, H., Al-Bahloul, M., Al-Khabbaz, A., Al-Khayat, A., 2011. Effect of environmental factors on photodegradation of polycyclic aromatic hydrocarbons (PAHs) in the water-soluble fraction of Kuwait crude oil in seawater. *Marine Environmental Research* 72, 143-150.
- Sahoo, D., Smith, J.A., 1997. Enhanced trichloroethene desorption from long-term contaminated soil using Triton X-100 and pH increases. *Environmental Science & Technology* 31, 1910-1915.
- Sarkar, D., Essington, M. E., Misra, K. C., 2000. Adsorption of mercury(II) by kaolinite. *Soil Science Society of America Journal* 64 (6), 1968–1975.
- Scelfo, G.M., Tjeerdema, R.S., 1991. A simple method for determination of Corexit 9527 in natural waters. *Marine Environmental Research* 31, 69-78.

- Shemer, H., Linden, K.G., 2007. Aqueous photodegradation and toxicity of the polycyclic aromatic hydrocarbons fluorene, dibenzofuran, and dibenzothiophene. *Water Research* 41, 853-861.
- Shen, Y., 1999. Sorption of natural dissolved organic matter on soil. *Chemosphere* 38, 1505-1515.
- Sigman, M.E., Schuler, P.F., Ghosh, M.M., Dabestani, R.T., 1998. Mechanism of pyrene photochemical oxidation in aqueous and surfactant solutions. *Environmental Science & Technology* 32, 3980-3985.
- Simpson, M.J., Simpson, A.J., Hatcher, P.G., 2004. Noncovalent interactions between aromatic compounds and dissolved humic acid examined by nuclear magnetic resonance spectroscopy. *Environmental Toxicology and Chemistry* 23, 355-362.
- Singer, M.M., Aurand, D., Bragin, G.E., Clark, J.R., Coelho, G.M., Sowby, M.L., Tjeerdema, R.S., 2000. Standardization of the preparation and quantitation of water-accommodated fractions of petroleum for toxicity testing. *Marine Pollution Bulletin* 40, 1007-1016.
- Skyllberg, U., Bloom, P.R., Qian, J., Lin, C., Bleam, W.F., 2006. Complexation of mercury(II) in soil organic matter: EXAFS evidence for linear two-coordination with reduced sulfur groups. *Environmental Science & Technology* 40, 4174-4180.
- Skyllberg, U., Drott, A., 2010. Competition between Disordered Iron Sulfide and Natural Organic Matter Associated Thiols for mercury(II)-An EXAFS Study. *Environmental Science & Technology* 44 (4), 1254-1259.
- Snoeyink, V. L., Jenkins, D., 1980. *Water Chemistry*. John Wiley & Sons, Inc., New York, USA.
- Stein, E.D., Cohen, Y., Winer, A.M., 1996. Environmental distribution and transformation of mercury compounds. *Critical Reviews in Environmental Science & Technology* 26, 1-43.

- Stylidi, M., Kondarides, D.I., Verykios, X.E., 2004. Visible light-induced photocatalytic degradation of Acid Orange 7 in aqueous TiO₂ suspensions. *Applied Catalysis B: Environmental* 47, 189-201.
- Sumesh, E., Bootharaju, M.S., Pradeep, T., 2011. A practical silver nanoparticle-based adsorbent for the removal of Hg²⁺ from water. *Journal of Hazardous Materials* 189, 450-457.
- Svensson, M., Allard, B., Duker, A., 2006. Formation of HgS: mixing HgO or elemental Hg with S, FeS or FeS₂. *Science of the Total Environment* 368, 418-423.
- Sweet, L.I., Zelikoff, J.T., 2001. Toxicology and immunotoxicology of mercury: A comparative review in fish and humans. *Journal of Toxicology and Environmental Health-Part B-Critical Reviews* 4, 161-205.
- Sylvestre, J.P., Kabashin, A.V., Sacher, E., Meunier, M., Luong, J.H.T., 2004. Stabilization and size control of gold nanoparticles during laser ablation in aqueous cyclodextrins. *Journal of the American Chemical Society* 126 (23), 7176–7177.
- UGA, 1983. Reference Soil Test Methods for the Southern Region of the United States, Southern Cooperative Series Bulletin 289, 1983. University of Georgia College of Agriculture Experiment Stations, Athens, GA, 30602.
- United Nations Environment Programme (UNEP), 2007. Global mercury assessment Report no.54790.01.
- USEPA., 2009. National primary drinking water regulations. <http://www.epa.gov/safewater/contaminants/index.html#inorganic> (accessed 06.10).
- Voice, T.C., Weber Jr, W.J., 1983. Sorption of hydrophobic compounds by sediments, soils and suspended solids-I. Theory and background. *Water Research* 17, 1433-1441.

- Wang, J., Deng, B., Chen, H., Wang, X., Zheng, J., 2009. Removal of aqueous Hg(II) by polyaniline: Sorption characteristics and mechanisms, *Environmental Science & Technology* 43 (14), 5223-5228.
- Wang, P., Keller, A.A., 2008. Particle-size dependent sorption and desorption of pesticides within a water-soil-nonionic surfactant system. *Environmental Science & Technology* 42, 3381-3387.
- Wang, Q., Kim, D., Dionysiou, D.D., Sorial, G.A., Timberlake, D., 2004. Sources and remediation for mercury contamination in aquatic systems-a literature review. *Environmental Pollution* 131 (2), 323–336.
- Wangl, C.X., Yediler, A., Peng, A., Kettrup, A., 1995. Photodegradation of phenanthrene in the presence of humic substances and hydrogen peroxide. *Chemosphere* 30, 501-510.
- Wen, S., Zhao, J.C., Sheng, G.Y., Fu, J.M., Peng, P.A., 2003. Photocatalytic reactions of pyrene at TiO₂/water interfaces. *Chemosphere* 50, 111-119.
- Wharton, M.J., Atkins, B., Charnockab, J.M., Livens, F.R., Patrick, R.A.D., Collison, D., 2000. An X-ray absorption spectroscopy study of the coprecipitation of Tc and Re with mackinawite (FeS). *Applied Geochemistry* 15 (3), 347–354.
- White, J.C., Pignatello, J.J., 1999. Influence of bisolute competition on the desorption kinetics of polycyclic aromatic hydrocarbons in soil. *Environmental Science & Technology* 33, 4292-4298.
- Widler, A.M., Seward, T.M., 2002. The adsorption of gold(I) hydrosulphide complexes by iron sulphide surfaces. *Geochimica et Cosmochimica Acta* 66, 383–402.

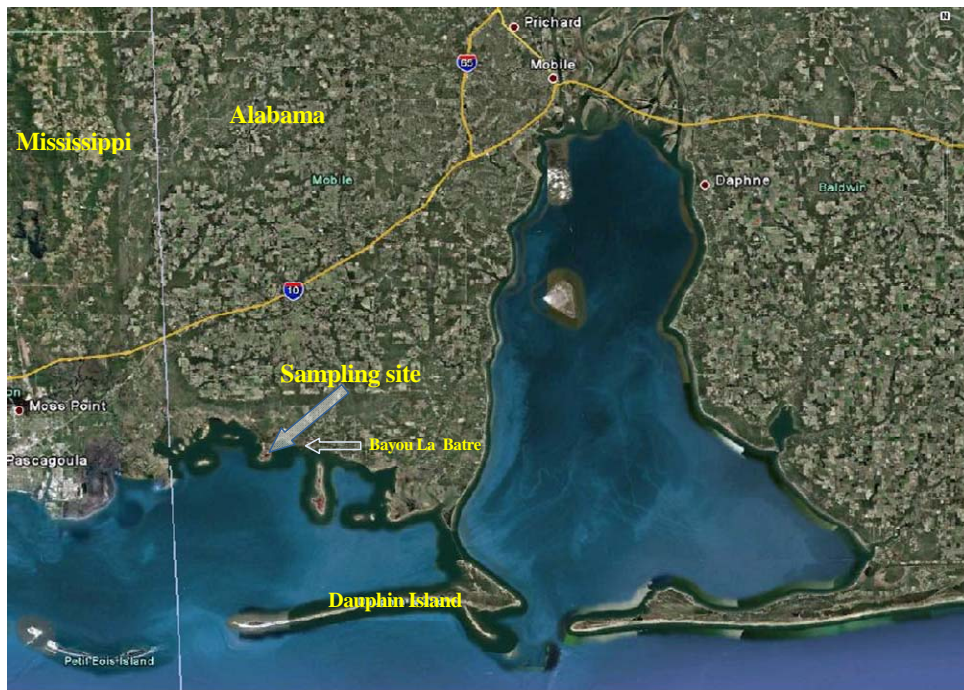
- Wolfenden, S., Charnock, J.M., Hilton, J., Livens, F.R., Vaughan, D.J., 2005. Sulfide species as a sink for mercury in lake sediments. *Environmental Science & Technology* 39 (17), 6644–6648.
- Wolthers, M., Charlet, L., Van Der Linde, P.R., Rickard, D., Van Der Weijden, C.H., 2005. Surface chemistry of disordered mackinawite (FeS). *Geochimica et Cosmochimica Acta* 69, 3469-3681.
- Wolthers, M., Van der Gaast, S. J., Rickard, D., 2003. The structure of disordered mackinawite. *American Mineralogist* 88 (11-12), 2007-2015.
- Wu, S.C., Gschwend, P.M., 1986. Sorption kinetics of hydrophobic organic compounds to natural sediments and soils. *Environmental Science & Technology* 20, 717-725.
- Xia, X., Li, G., Yang, Z., Chen, Y., Huang, G.H., 2009. Effects of fulvic acid concentration and origin on photodegradation of polycyclic aromatic hydrocarbons in aqueous solution: Importance of active oxygen. *Environmental Pollution* 157, 1352-1359.
- Xing, B., Pignatello, J.J., 1997. Dual-mode sorption of low-polarity compounds in glassy poly(vinyl chloride) and soil organic matter. *Environmental Science & Technology* 31 (3), 792–799.
- Xing, B., Pignatello, J.J., Gigliotti, B., 1996. Competitive sorption between atrazine and other organic compounds in soils and model sorbents. *Environmental Science & Technology* 30, 2432-2440.
- Xiong, Z., He, F., Zhao, D., Barnett, M.O., 2009. Immobilization of mercury in sediment using stabilized iron sulfide nanoparticles. *Water Research* 43(20), 5171-5179.

- Xu, Z., Jing, C., Li, F., Meng, X., 2008. Mechanisms of photocatalytical degradation of monomethylarsonic and dimethylarsinic acids using nanocrystalline titanium dioxide. *Environmental Science & Technology* 42, 2349-2354.
- Yang, G., Zhao, Y., Lu, X., Gao, X., 2005. Adsorption of methomyl on marine sediments. *Colloids and Surfaces A: Physicochemical and Engineering Aspects* 264, 179-186.
- Yang, K., Zhu, L., Xing, B., 2006. Enhanced soil washing of phenanthrene by mixed solutions of TX100 and SDBS. *Environmental Science & Technology* 40, 4274-4280.
- Yantasee, W., Warner, C.L., Snagvanich, T., Addleman, R.S., Carter, T.G., Wiacek, R.J., Fryxell, G.E., Timchalk, C., Warner, M.G., 2007. Removal of heavy metals from aqueous systems with thiol functionalized superparamagnetic nanoparticles. *Environmental Science & Technology* 41, 5114-5119.
- Yin, Y., Allen, H.E., Huang, C.P., 1997. Kinetics of mercury adsorption and desorption on soil. *Environmental Science & Technology* 31, 496-503.
- Yuan, S., Shu, Z., Wan, J., Lu, X., 2007. Enhanced desorption of hexachlorobenzene from kaolin by single and mixed surfactants. *Journal of Colloid and Interface Science* 314, 167-175.
- Zepp, R.G., Baughman, G.L., Schlotzhauer, P.F., 1981. Comparison of photochemical behavior of various humic substances in water: II. Photosensitized oxygenations. *Chemosphere* 10, 119-126.
- Zhang, F., Nriagu, J.O., Itoh, H., 2005. Mercury removal from water using activated carbons derived from organic sewage sludge. *Water Research* 39 (2-3), 389-395.
- Zhang, J., He, M., 2011. Effect of surfactants on sorption and desorption of phenanthrene onto black carbon. *Water Environment Research* 83, 15-22.

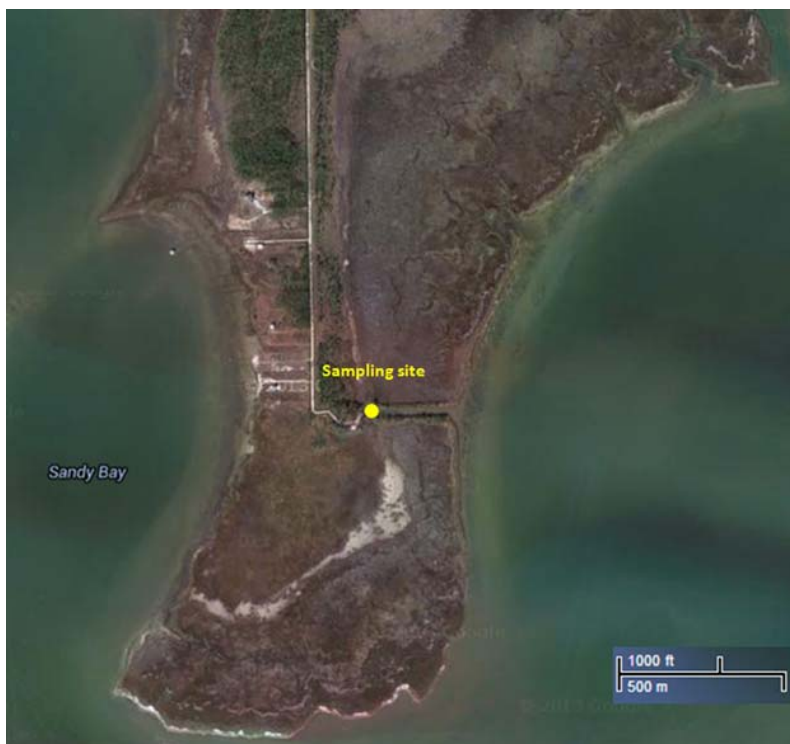
- Zhang, L., Li, P., Gong, Z., Li, X., 2008. Photocatalytic degradation of polycyclic aromatic hydrocarbons on soil surfaces using TiO₂ under UV light. *Journal of Hazardous Materials* 158, 478-484.
- Zhang, L., Planas, D., 1994. Biotic and abiotic mercury methylation and demethylation in sediments. *Bulletin of Environmental Contamination and Toxicology* 52, 691-698.
- Zhang, M., He, F., Zhao, D., Hao, X., 2011. Degradation of soil-sorbed trichloroethylene by stabilized zero valent iron nanoparticles: Effects of sorption, surfactants, and natural organic matter. *Water Research* 45 (7), 2401-2414.
- Zhang, M., Zhu, L., 2010. Effect of SDBS-Tween 80 mixed surfactants on the distribution of polycyclic aromatic hydrocarbons in soil-water system. *Journal of Soils and Sediments* 10, 1123-1130.
- Zhang, Y., Wong, J.W.C., Liu, P., Yuan, M., 2011. Heterogeneous photocatalytic degradation of phenanthrene in surfactant solution containing TiO₂ particles. *Journal of Hazardous Materials* 191, 136-143.
- Zhao, B., Zhu, L., Li, W., Chen, B., 2005. Solubilization and biodegradation of phenanthrene in mixed anionic-nonionic surfactant solutions. *Chemosphere* 58, 33-40.
- Zhao, D., Hunter, M., Pignatello, J.J., White, J.C., 2002. Application of the dual-mode model for predicting competitive sorption equilibria and rates of polycyclic aromatic hydrocarbons in estuarine sediment suspensions. *Environmental Toxicology and Chemistry* 21, 2276-2282.
- Zhao, D., Pignatello, J.J., White, J.C., Braida, W., Ferrandino, F., 2001. Dual-mode modeling of competitive and concentration dependent sorption and desorption kinetics of polycyclic aromatic hydrocarbons in soils. *Water Resources Research* 37 (8), 2205-2212.

Appendix

Appendix 1. Location of the sampling site for the sediments and seawater samples.



(a)



(b)

Figure A-1. (a) An overview of the sampling location of two marine sediments and seawater samples; and (b) A close-up of the sampling sites.

Appendix 2. PAHs analysis in seawater and marine sediments.

The loamy sand and sandy loam sediments were extracted and analyzed for PAHs following a revised method by Zhao et al. (2002) and White and Pignatello (1999). The 16 PAHs specified in EPA Method 610 PAH mixtures were targeted. The samples were wet-sieved with seawater to obtain a size fraction of 75-840 μm , and extracted with methanol at 70 $^{\circ}\text{C}$ for 12 h (sediment (dry wt.): methanol = 1 g: 50 mL). The PAHs were then phase transferred to methylene chloride (methanol: DI water: methylene chloride = 40 mL: 400 mL: 20 mL). The extracts were blown to dryness under a stream of nitrogen gas. The dried extracts were re-dissolved in 1 mL of methylene chloride for GC-MS analysis.

The seawater samples filtered through 0.45 µm membrane filters were directly extracted with methylene chloride (seawater: methylene chloride = 400 mL: 20 mL). The extracts were concentrated by 40 times under nitrogen gas and then analyzed by GC-MS.

Table A-1. PAHs targeted and detected in the Gulf Coast seawater (seawater was filtered through 0.45 µm membrane without autoclaving), loamy sand, and sandy loam sediments (sediments were only wet-sieved).

PAHs	Detection limit (µg/L)	Seawater		Loamy sand sediment		Sandy loam sediment	
		Average concentration	Standard error	Average content	Standard error	Average content	Standard error
		(µg/L)		(µg/g)		(µg/g)	
Naphthalene	1	0.0019	0.0000	0.0075	0.0008	0.0114	0.0049
Acenaphthylene	1	ND*		0.0018	0.0001	0.0011	0.0002
Acenaphthene	0.5	ND		0.0009	0.0002	0.0023	0.0009
Fluorene	0.5	ND		ND		ND	
Phenanthrene	1	0.0029	0.0000	0.0103	0.0007	0.0107	0.0044
Anthracene	0.5	ND		ND		ND	
Fluoranthene	1	ND		0.0109	0.0008	0.0195	0.0100
Pyrene	1	0.0028	0.0000	ND		ND	
Benz(a)anthracene	1	ND		ND		ND	
Chrysene	1	ND		ND		ND	
Benzo(b)fluoranthene	1	0.0028	0.0001	ND		0.0043	0.0025
Benzo(k)fluoranthene	1	ND		0.0014	0.0005	0.0076	0.0041
Benzo(a)pyrene	1	0.0014	0.0000	ND		ND	
Dibenz(a,h)anthracene	1	ND		0.0022	0.0001	0.0039	0.0026
Indeno(1,2,3-cd)pyrene	1	ND		0.0022	0.0001	0.0039	0.0016
Benzo(ghi)perylene	1	0.0012	0.0001	ND		0.0020	0.0034

*ND: Not detectable

PAHs in the concentrated solvent were analyzed using an Agilent Gas Chromatography (7890A) coupled with the 5975C Series Mass Spectrometry. A DB-EUPAH column (length 20 m; inner diameter 0.18 mm; film thickness 0.14 μm) was used to separate the analytes. The front inlet temperature was set at 250 $^{\circ}\text{C}$. The GC oven temperature was programmed as follows: 50 $^{\circ}\text{C}$ (hold for 0.8 min), ramp to 180 $^{\circ}\text{C}$ at 40 $^{\circ}\text{C}/\text{min}$, ramp to 230 $^{\circ}\text{C}$ at 7 $^{\circ}\text{C}/\text{min}$ (hold for 0.5 min), and ramp to 335 $^{\circ}\text{C}$ at 15 $^{\circ}\text{C}/\text{min}$ (hold for 5 min). The sample injection volume was 2 μL . GC-MS analysis was performed utilizing a selected ion monitoring (SIM) mode to improve detection limits. Standard curves were developed for each PAH using the EPA standards. **Table A-1** presents the concentrations of the PAHs in the seawater and sediments and the respective detection limits of the GC-MS method.

Appendix 3. Dispersant-enhanced solubilization of phenanthrene.

Batch experiments were conducted with 43-mL glass vials with Teflon-lined caps to determine solubility enhancement of phenanthrene by Corexit EC9500A at concentration ranging from 0 to 360 mg/L. Each (42 mL) of the solutions was mixed with 0.01 g of phenanthrene in duplicate. The mixtures were equilibrated on an end-to-end rotator at 30 rpm kept at 21 ± 1 $^{\circ}\text{C}$ in an incubator for 7 days. Then, the vials were centrifuged at 3000 rpm for 10 minutes to separate any undissolved particulates. After 12 h of standstill, 1 mL each of the supernatants was sampled and analyzed for soluble phenanthrene.

Phenanthrene was analyzed by HPLC (HP series 1100, Hewlett Packard, CA, USA) equipped with a UV detector and a Zorbax SB-C18 column (150 \times 468 mm). The mobile phase consisted of 70% acetonitrile, 30% water, and 0.1% phosphoric acid, and the flow rate was set at 1.2 mL/min. The system was operated at 40 $^{\circ}\text{C}$. The optimal UV detection wavelength for phenanthrene was found to be 250 nm. The method afforded a detection limit of 4 $\mu\text{g}/\text{L}$ at a

sample volume of 80 μL . Preliminary studies indicated that the dispersant did not interfere with the phenanthrene analysis.

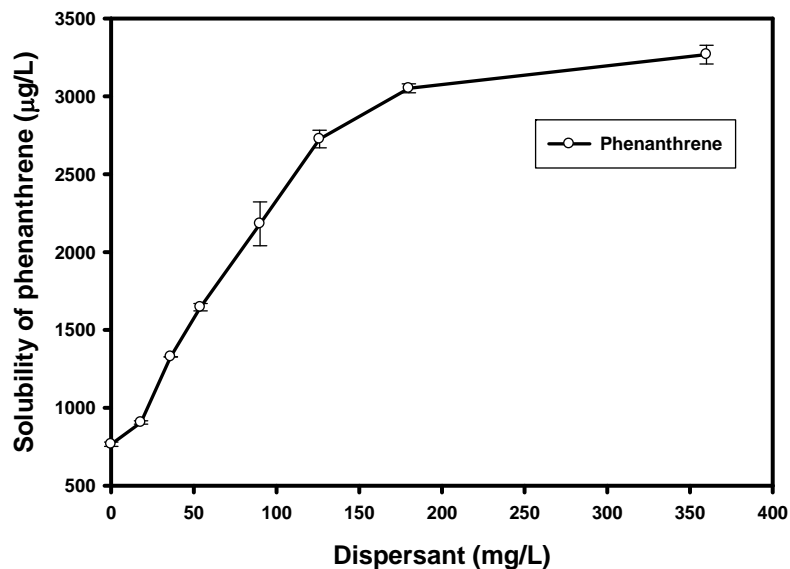


Figure A-2. Solubility of phenanthrene as a function of Corexit EC9500A dosage. Experimental conditions: phenanthrene = 0.01 g, dispersant solution (0-360 mg/L) = 42 mL, equilibrium time = 7 days. Data are plotted as mean of duplicates, and error bars indicate standard error from the mean.

References

White, J.C., Pignatello, J.J., 1999. Influence of bisolute competition on the desorption kinetics of polycyclic aromatic hydrocarbons in soil. *Environmental Science & Technology* 33, 4292-4298.

Zhao, D., Hunter, M., Pignatello, J.J., White, J.C., 2002. Application of the dual-mode model for predicting competitive sorption equilibria and rates of polycyclic aromatic hydrocarbons in estuarine sediment suspensions. *Environmental Toxicology and Chemistry* 21, 2276-2282.